

AD-A043 499

GENERAL RESEARCH CORP SANTA BARBARA CALIF  
THE ROSCOE MANUAL. VOLUME 14B. MIDLATITUDE DENSITY PROFILES OF --ETC(U)  
JUN 75 B F MYERS

F/G 17/9

DNA001-74-C-0182

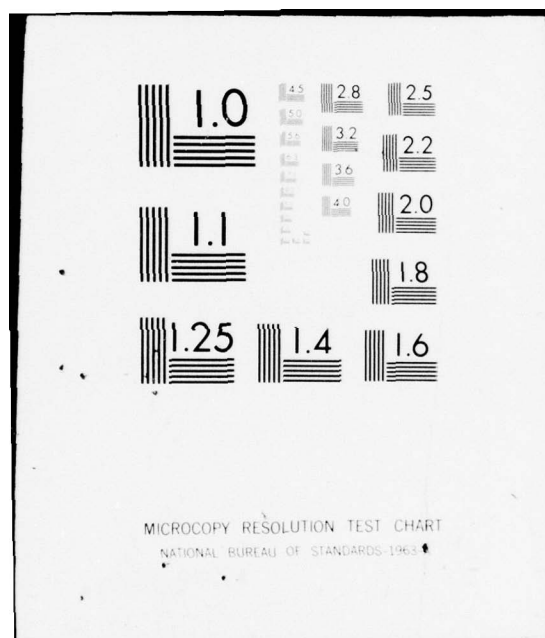
DNA-3964F-14B

NL

UNCLASSIFIED

1 of 2  
AD  
A043499







ADA 043499

2  
DNA 3964F - 14b

# THE ROSCOE MANUAL

## Volume 14b - Midlatitude Density Profiles of Selected Atmospheric Species

Science Applications, Inc.

P. O. Box 2351

La Jolla, California 92038

13 June 1975

Final Report for Period 2 March 1974—28 February 1975

CONTRACT No. DNA 001-74-C-0182

APPROVED FOR PUBLIC RELEASE;  
DISTRIBUTION UNLIMITED.

THIS WORK SPONSORED BY THE DEFENSE NUCLEAR AGENCY  
UNDER RDT&E RMSS CODES B322074464 S99QAXHC06428 AND  
B322075464 S99QAXHC06432 H2590D.

DDC FILE COPY

Prepared for

Director

DEFENSE NUCLEAR AGENCY

Washington, D. C. 20305

DDC  
RECEIVED  
AUG 30 1977  
C

Destroy this report when it is no longer  
needed. Do not return to sender.



## UNCLASSIFIED

SECURITY CLASSIFICATION OF THIS PAGE (When Data Entered)

REPORT DOCUMENTATION PAGE		READ INSTRUCTIONS BEFORE COMPLETING FORM
1. REPORT NUMBER DNA 3964F-14b	2. GOVT ACCESSION NO.	3. RECIPIENT'S CATALOG NUMBER
4. TITLE (and Subtitle) THE ROSCOE MANUAL - Volume 14b. Midlatitude Density Profiles of Selected Atmospheric Species	5. TYPE OF REPORT & PERIOD COVERED Final Report for Period 2 Mar 74 - 28 Feb 75	
7. AUTHOR(s) B. F. Myers	6. PERFORMING ORG. REPORT NUMBER SAI-75-609-LJ-2B	
9. PERFORMING ORGANIZATION NAME AND ADDRESS Science Applications, Inc. P.O. Box 2351 La Jolla, California 92038	8. CONTRACT OR GRANT NUMBER(s) DNA 001-74-C-0182	
11. CONTROLLING OFFICE NAME AND ADDRESS Director Defense Nuclear Agency Washington, D.C. 20305	10. PROGRAM ELEMENT PROJECT, TASK AREA & WORK UNIT NUMBERS Subtasks S99QAXHC064-28/32	
14. MONITORING AGENCY NAME & ADDRESS (if different from Controlling Office)	12. REPORT DATE 13 June 1975	
16. DISTRIBUTION STATEMENT (of this Report)  Approved for public release; distribution unlimited.	13. NUMBER OF PAGES 140 (12) 137p.	
17. DISTRIBUTION STATEMENT (of the abstract entered in Block 20, if different from Report)	15. SECURITY CLASS (of this report)  UNCLASSIFIED	
18. SUPPLEMENTARY NOTES  This work sponsored by the Defense Nuclear Agency under RDT&E RMSS Codes B322074464 S99QAXHC06428 and B322075464 S99QAXHC06432 H2590D.	15a. DECLASSIFICATION/DOWNGRADING SCHEDULE	
19. KEY WORDS (Continue on reverse side if necessary and identify by block number)  Atmospheric Species Density Profiles	C	
20. ABSTRACT (Continue on reverse side if necessary and identify by block number)  Atmospheric density profiles are presented for the following species: atomic oxygen, molecular oxygen in the <sup>1g</sup> state, ozone, nitric oxide, atomic nitrogen, nitrogen dioxide, carbon dioxide, and water vapor. The profiles are intended to represent mean densities at midlatitudes for noon and midnight conditions. A review and limited discussion of recent obser- vations and calculations are given.		

DD FORM 1 JAN 73 1473 EDITION OF 1 NOV 65 IS OBSOLETE

UNCLASSIFIED

SECURITY CLASSIFICATION OF THIS PAGE (When Data Entered)

402754

UNCLASSIFIED

SECURITY CLASSIFICATION OF THIS PAGE(When Data Entered)

## 18. SUPPLEMENTARY NOTES (Continued)

### EDITORS' NOTE

Volumes 13 to 17 were originally published by SAI to describe the atmospheric, geomagnetic, and high-altitude energy deposition and neutral heave models for ROSCOE. This whole section of code, when associated with an appropriate DRIVER subroutine, operated as a package that ran independently of the rest of the ROSCOE structure. Provision was also made, within this high-altitude package, for two completely independent descriptions of atmospheric heave, each with its own description of atmospheric chemistry.

When GRC incorporated this section of code within the ROSCOE framework, some modifications were necessary, which means that some of the descriptions in Volumes 13 to 17 are inappropriate to ROSCOE as it now exists. In particular, the NRL heave routines (deck NRLHYD) and associated chemistry (deck NRLCHM) are not presently used in ROSCOE. Three other subroutines are different: subroutines ATMOSU, EIF, and XTCOEF correspond to the ROSCOE subroutines ATMOS, EXPINT, and WDXP respectively. With these exceptions, the subroutines described in Volumes 13 to 17 correspond exactly to those currently in ROSCOE.

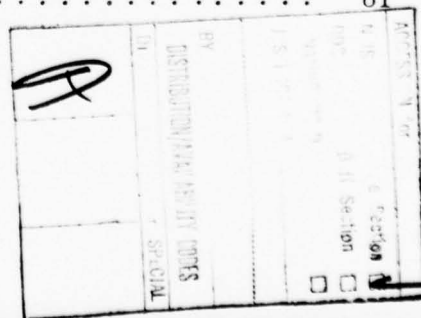
The bulk of this work ( 85 percent) was supported by the author; the remaining portion was sponsored by the Defense Nuclear Agency (see Item 8).

UNCLASSIFIED

SECURITY CLASSIFICATION OF THIS PAGE(When Data Entered)

# CONTENTS

	<u>Page</u>
SUMMARY . . . . .	7
1. INTRODUCTION . . . . .	9
2. DENSITY PROFILE OF ATOMIC OXYGEN . . . . .	11
2.1 Introduction . . . . .	11
2.2 Atomic Oxygen Densities Above 90 km . . . . .	11
2.3 Atomic Oxygen Densities Between 40 and 90 km . . . . .	21
2.4 Atomic Oxygen Densities Below 40 km . . . . .	26
2.5 Atomic Oxygen Profile Between 0 and 120 km . . . . .	29
3. DENSITY PROFILE OF MOLECULAR OXYGEN, $O_2(a^1\Delta_g)$ . . . . .	32
3.1 Introduction . . . . .	32
3.2 Measurements . . . . .	32
3.3 Model Calculations . . . . .	36
3.4 Selection of $O_2(^1\Delta_g)$ Profile . . . . .	39
4. DENSITY PROFILE OF OZONE . . . . .	44
4.1 Introduction . . . . .	44
4.2 Daytime Densities . . . . .	44
4.3 Nighttime Densities . . . . .	50
5. DENSITY PROFILE OF NITRIC OXIDE . . . . .	59
5.1 Introduction . . . . .	59
5.2 Daytime Nitric Oxide Densities Above 120 km . . . . .	59
5.3 Daytime Nitric Oxide Densities Below 120 km . . . . .	67
5.4 Additional Daytime Nitric Oxide Data . . . . .	74
5.5 Nighttime Nitric Oxide Densities . . . . .	81





	<u>Page</u>
6. DENSITY PROFILE OF ATOMIC NITROGEN .....	83
6.1 Introduction .....	83
6.2 Measurements .....	83
6.3 Model Calculations .....	86
6.4 Selection of Atomic Nitrogen Profile .....	86
7. DENSITY PROFILE OF NITROGEN DIOXIDE .....	91
7.1 Introduction .....	91
7.2 Daytime Nitrogen Dioxide Densities .....	91
7.3 Nighttime Nitrogen Dioxide Densities .....	99
8. CARBON DIOXIDE PROFILES .....	101
8.1 Introduction .....	101
8.2 Measurements .....	101
8.3 Model Calculations .....	102
8.4 Selection of CO <sub>2</sub> Profile .....	104
8.5 Comparison of Profiles .....	106
9. DENSITY PROFILES FOR WATER VAPOR .....	108
9.1 Introduction .....	108
9.2 Measurements .....	108
9.3 Model Calculations .....	114
9.4 Selection of Water Profile .....	116
REFERENCES .....	122

## ILLUSTRATIONS

		<u>Page</u>
2-1	Atomic Oxygen Densities Above 90 km . . . . .	12
2-2	Comparison of Atomic Oxygen Profile of Table 2-1 with Model Profile of Moe [Mo-73] . . . . .	22
2-3	Atomic Oxygen Densities Between 40 and 90 km . . . . .	24
2-4	Atomic Oxygen Profile Between 0 and 120 km for Noon and Midnight Conditions . . . . .	31
3-1	Measured $O_2(^1\Delta_g)$ Densities Between 30 and 120 km . . . . .	33
3-2	Calculated $O_2(^1\Delta_g)$ Densities Between 0 and 100 km . . . . .	37
3-3	Profile of $O_2(^1\Delta_g)$ Between 0 and 140 km for Noon and Midnight Conditions . . . . .	42
4-1	Daytime Ozone Densities Between 0 and 110 km . . . . .	46
4-2	Profile of Ozone Between 0 and 110 km for Noon and Midnight Conditions . . . . .	51
4-3	Nighttime Ozone Densities Between 0 and 110 km . . . . .	54
4-4	Dependence of Atmospheric Ozone on Latitude and Season . . . . .	56
5-1	Nitric Oxide Densities Above 120 km . . . . .	60
5-2	Nitric Oxide Densities vs Decimetric Solar Flux . . . . .	64
5-3	Profiles of Nitric Oxide Above 120 km as a Function of Solar Activity . . . . .	68
5-4	Nitric Oxide Densities Below 120 km . . . . .	69
5-5	Nitric Oxide Profile Below 120 km for Noon and Midnight Conditions . . . . .	76
5-6	Dependence of Nitric Oxide Density on Sunspot Number at 105, 110 and 130 km . . . . .	79
6-1	Measured Atomic Nitrogen Densities . . . . .	84

	<u>Page</u>
6-2    Calculated Atomic Nitrogen Densities . . . . .	87
6-3    Atomic Nitrogen Profile for Noon and Midnight Conditions . . . . .	90
7-1    Nitrogen Dioxide Densities Below 50 km . . . . .	92
7-2    Calculated Nitrogen Dioxide Densities Above 20 km . . . . .	95
7-3    Nitrogen Dioxide Profile Between 0 and 140 km for Noon and Midnight Conditions . . . . .	98
8-1    Carbon Dioxide Density and Mixing Ratio Profiles . . . . .	103
8-2    Selection of Carbon Dioxide Densities Between 100 and 120 km by Interpolation . . . . .	105
9-1    Volume Mixing Ratios for H <sub>2</sub> O Up To 16 km . . . . .	109
9-2    Volume Mixing Ratios for H <sub>2</sub> O Between 10 and 100 km . . . . .	111
9-3    Calculated Water Densities Between 40 and 160 km . . . . .	115
9-4    Midlatitude, Tropospheric Water Vapor Densities [Ca-74] . . . . .	117
9-5    Water Vapor Profile . . . . .	121



## TABLES

		<u>Page</u>
2-1	Average Values of Oxygen Atom Densities for Altitudes of 90 km and Greater . . . . .	20
2-2	Comparison of Atomic Oxygen Profile of Table 2-1 with Model Profile of Moe [Mo-73] . . . . .	21
2-3	Average Values of Oxygen Atom Densities for Altitudes from 40 to 85 km . . . . .	27
2-4	Calculated Values of Atomic Oxygen Densities Below 40 km . . . . .	28
2-5	Atomic Oxygen Profile to 120 km for Noon and Midnight Conditions . . . . .	30
3-1	Profile of $O_2(^1\Delta_g)$ for Noon and Midnight Conditions . . . . .	41
4-1	Calculation of Average Ozone Densities Between 75 and 125 km . . . . .	49
4-2	Profile of Ozone for Noon and Midnight Conditions . . . . .	52
4-3	Average Ozone Densities Above 60 km for Nighttime Conditions . . . . .	58
5-1	Nitric Oxide Densities at 215 km and the Decimetric Solar Flux . . . . .	63
5-2	Selection of Values of Nitric Oxide Densities Below 120 km . . . . .	73
5-3	Nitric Oxide Profile for Noon and Midnight Conditions . . . . .	75
6-1	Nitrogen Atom Densities for Noon and Midnight Conditions . . . . .	89
7-1	Nitrogen Dioxide Densities for Noon and Midnight Conditions . . . . .	97
8-1	Carbon Dioxide Mixing Ratio and Densities . . . . .	106

	<u>Page</u>
9-1a Midlatitude Water Vapor Concentrations in the Troposphere . . . . .	118
9-1b Average of Measured Values of Water Mixing Ratios Between 15 and 50 km . . . . .	118
9-2 Water Vapor Densities . . . . .	120

## SUMMARY

Atmospheric density profiles are presented for the following species: atomic oxygen, molecular oxygen in the  $a^1\Delta_g$  state, ozone, nitric oxide, atomic nitrogen, nitrogen dioxide, carbon dioxide and water vapor. These profiles are intended to represent mean densities at midlatitudes for noon and midnight conditions. A review and limited discussion of recent observations and calculations are given.

## 1. INTRODUCTION

Profiles of selected atmospheric species have been constructed based on a collation of observed and calculated densities from ground level to several hundred kilometers altitude. The profiles are intended to represent mean densities at midlatitudes primarily in the northern hemisphere. The profiles are presented for only two diurnal conditions: noon and midnight. In the data from which the profiles were drawn, there are to be found significant variations as a result of geographical, seasonal, solar and other environmental factors but the intended applications of the profiles were envisaged to be not so precise as to require the incorporation of such variations, were this possible with the present state of knowledge about each species. Furthermore, there is considerable scatter in observational data (as well as in calculated densities) in certain ranges of altitude which may result not only from experimental difficulties but also from a lack of understanding or analysis of the effect of the factors mentioned above.

Only mean profiles have been presented; the uncertainty associated with these profiles has not been explicitly given. However, a general appreciation of the uncertainties in the mean profiles can be obtained from the collations of the data reviewed in this report.

Profiles are presented for the following species: atomic oxygen, molecular oxygen in the  $a^1\Delta_g$  state, ozone, nitric oxide, atomic nitrogen, nitrogen dioxide, carbon dioxide, and water vapor. This list is restricted, of course, and in certain altitude ranges, excepting molecular oxygen and nitrogen, important species are not included as is the case for nitric acid in the troposphere and stratosphere.

Following the completion of the profile selection, additional, important data have appeared in the literature. These data are presented separately as late reports in the sections for the corresponding species. Also, note that the survey of the literature was not intended to be exhaustive but to include primarily the most recent observations and calculations.

## 2. DENSITY PROFILE OF ATOMIC OXYGEN

### 2.1 INTRODUCTION

An atomic oxygen profile is selected for altitudes from ground level to 120 km and for midlatitudes. The selection is based on observations and model calculations. At present, the reported observations of atomic oxygen are restricted to altitudes above 90 km; below 90 km, reliance has to be placed on model calculations.

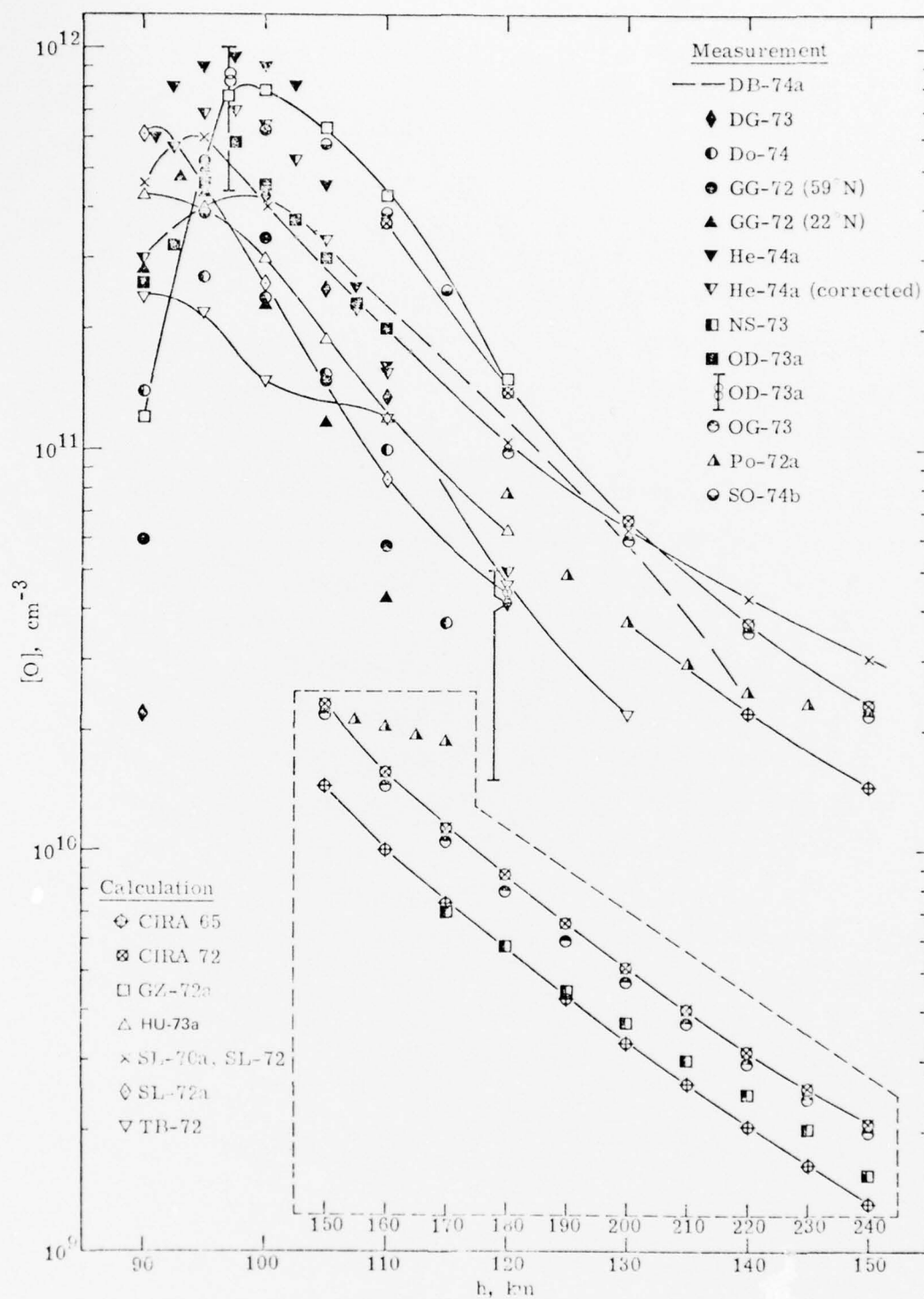
Several difficulties are encountered when attempting to select an atomic oxygen profile. For altitudes above 90 km, the observations demonstrate diurnal [Da-72d, OD-73a, Of-74, Po-72a], seasonal [DG-73, OD-73a, Of-74, Sc-74a, SL-72a], and latitudinal and longitudinal [Da-72d, DG-73, DG-74] variations in the atomic oxygen density; these variations cannot yet be taken into account in a consistent manner as there are important problems concerning transport of atomic oxygen which have yet to be understood. In addition, the observations are sporadic, thus far, and this contributes to uncertainties in the selected profiles. Below 90 km, where model calculations are the source of atomic oxygen densities, problems involving transport coefficients (i. e., eddy diffusion coefficients), boundary conditions, restricted modelling of mass motions and simplified sets of reactions remain. Adequate comparisons between different model calculations have not been made.

### 2.2 ATOMIC OXYGEN DENSITIES ABOVE 90 KM

#### 2.2.1 Measurements

The atomic oxygen densities above about 90 km are plotted in Fig. 2-1. Measurements [NS-73, OG-73, Po-72a] for altitudes above





120 km are given on Fig. 2-1 but will not be discussed in general. Consider first, the observational data for rocket-based experiments. Henderson [He-74a] has measured atomic oxygen densities by use of a thin, silver film whose resistance changes in the event that oxygen atoms are adsorbed; his measurements apply to a latitude of  $39^{\circ}\text{N}$ . Both the original and corrected [He-74a] data of Henderson are plotted in Fig. 2-1; data between 90 and 105 km were reduced in value by Henderson so as to obtain a reasonable, composite profile over the altitude range 90 to 125 km. The data of Henderson peak near 97 km and decline rapidly at other altitudes. The error associated with Henderson's measurements is about  $\pm 50\%$ . Measurements were also made [He-74a] at a latitude of  $71^{\circ}\text{N}$  but these measurements are not included in Fig. 2-1 as our present interests are restricted to midlatitudes. However, note that at a latitude of  $71^{\circ}\text{N}$ , the measured oxygen atom densities are an order of magnitude smaller than at  $39^{\circ}\text{N}$ , using the same experimental technique for the range of altitudes between 90 and 115 km, and become similar only above 120 km.

An extensive atomic oxygen profile has been obtained by Offermann et al. [OD-73a, OG-73] between 90 and 240 km by combining photometer measurements at  $5577 \text{ \AA}$  for altitudes below 118 km with mass spectrometer measurements at altitudes above 118 km. The mass spectrometer walls were cryogenically cooled to  $8^{\circ}\text{K}$  to minimize losses of atomic oxygen in the ion source. The measurements were consistent in that the photometer and mass spectrometer yielded atomic oxygen densities which were in good agreement in the overlap altitude range near 118 km. The density of atomic oxygen peaks at about 97 km and is in agreement with the corrected data of Henderson [He-74a] between 90 and 115 km. Note also, the good agreement above 120 km between the atomic oxygen densities of Offermann and Grossmann [OG-73] and



those of the CIRA 72 model atmosphere. Offermann and Drescher [OD-73a] summarize previous atomic oxygen measurements (based mainly on photometer results), and find variations with day of the year, local time and a weak variation with magnetic index.

Scholz and Offermann [SO-74b] have extended the mass spectrometer measurements to the altitude range 85 to 115 km at latitude  $39.6^{\circ}\text{N}$ ; these results are shown in Fig. 2-1; their oxygen atom densities are relatively high, particularly at altitudes above 105 km. The results of Offermann and colleagues have been compared with previous mass spectrometer measurements [SO-74b, Of-74] and the conclusion is reached that, with a certain degree of confidence, the previous results obtained with uncooled mass spectrometer walls should be increased by a factor of 2.5. A review of the older mass spectrometer measurements has not been included in the present review.

Also shown in Fig. 2-1, is the range of atomic oxygen densities at 95 km deduced from photometer measurements of the 5577 Å air-glow [OD-73a].

Measurements of the atomic oxygen density have been made by Golomb and Good [GG-72] based on the O-NO chemiluminescence. These measurements, which are shown on Fig. 2-1, were made at  $22^{\circ}\text{N}$  and  $59^{\circ}\text{N}$ ; the error of these measurements is a factor of  $\pm 2.5$  below 120 km. For the measurements at  $59^{\circ}\text{N}$ , data were obtained at 2245 hrs (and 0300 hrs but these measurements are not represented on Fig. 2-1). Golomb and Good note that the peak of the oxygen atom density seems to ascend from about 93 to 99 km as the night progresses and this can be understood from their measurements and also by comparison with Henderson's (at 0230 hr) if considerations of latitude are neglected. The results of Golomb and Good between 110 and 150 km are not shown;

in this altitude region, they found a minimum at 120 km in the atomic oxygen profiles with values of the density ranging from about  $10^{10}$  to  $4 \times 10^{10} \text{ cm}^{-3}$ . Other measurements do not indicate a minimum although densities in the range  $1.5$  to  $5 \times 10^{10} \text{ cm}^{-3}$  have been deduced as discussed below. Golomb and Good suggest the minima might be due to a very complicated wind shear and turbulence structure in the 90-130 km range which was revealed by TMA (tetramethylaluminum) trails released 30 minutes prior to their experiment. The TMA radiance is believed to be associated with the atomic oxygen densities. Thus in addition to seasonal and latitudinal variations, local motion of the atmosphere can apparently contribute significantly to variation in atomic oxygen density.

Atomic oxygen densities have been deduced from satellite measurements of the  $5577 \text{ \AA}$  airglow [DG-73, DG-74] and from the O-NO chemiluminescence [Do-74]. The photometer data clearly demonstrate latitudinal and semiannual variations. But, discounting these variations, the deduced oxygen atom densities appear to be significantly smaller than those obtained from the measurements thus far considered. The upper limits to the photometer data [DG-73, Fig. 19] are plotted on Fig. 2-1 and the range of all measurements is shown at 120 km; these data were obtained for  $49^\circ\text{N}$ . There is some uncertainty in the value of the rate constant for the process yielding the radiator,  $\text{O}(^1\text{S})$ , but to match densities observed and calculated at 120 km by others (i.e.,  $[\text{O}] \cong 10^{11} \text{ cm}^{-3}$ ), would require the rate constant to be reduced by a factor of 25. (See also DG-74, particularly the last paragraph of the paper.)

The O-NO chemiluminescence measurements [Do-74] are interpreted as leading to an upper limit to  $[\text{NO}][\text{O}]$ . Using measured

values of [NO], the O-atom densities have been computed; a representative profile is shown on Fig. 2-1 [Do-74, Fig. 1, 44°S, lower curve]. The profile is again consistently lower than other profiles of Fig. 2-1.

A very recently reported measurement [DB-74a] in the altitude range up to 140 km is shown on Fig. 2-1. These were nighttime measurements at 57°N and employed a new technique: in situ measurement of atomic oxygen by absorption and resonance fluorescence. Absolute values of the atomic oxygen density were determined from the absorption experiments; using these data, the resonance fluorescence measurements were calibrated and were extrapolated to oxygen density ranges where the absorption technique was insensitive. The results of these measurements [DB-74a] are in reasonable agreement with those of Offermann et al. [OD-73a, OG-73].

The data plotted on Fig. 2-1 are for a variety of times in the year. Seasonal variations have been derived from data analysis by several investigators, at least [Sc-74a, DG-73, Of-74]. All these investigations show a minimum in the atomic oxygen density in the summer, between June and September and also demonstrate yearly variations of about a factor of three in atomic oxygen densities. Of the measurements on Fig. 2-1, only two were made during the minimum: Henderson's [He-74a] in August and Golomb and Good's [GG-72] at 59°N also in August. The remainder were made in March, May, September, October, and November. There is no clear seasonal correlation among the measurements shown on Fig. 2-1. In addition to the summer minimum, some investigations [Sc-74a, DG-73] show a minimum in January; these investigations also show, inconsistently, maximum oxygen atom densities of 2 or  $3 \times 10^{11} \text{ cm}^{-3}$  at 97 and 120 km, respectively.

### 2.2.2 Model Calculations

Four recent model calculations are considered here to examine the calculated atomic oxygen profiles for altitudes above 90 km. No attempt has been made at a thorough comparison. The two model calculations of Shimazaki and Laird [SL-70a, SL-72] and Hunt [Hu-73a] give similar results as indicated on Fig. 2-1. Both models include numerous chemical reactions (Hu-73a has the greater number, 150) and account for eddy and molecular diffusion; the eddy diffusion coefficient profiles (for the results shown on Fig. 2-1) are also similar. Diffusive equilibrium was assumed at the upper boundary ( $\sim 150$ - $160$  km). In spite of the fact that these calculations were carried out for conditions at the equator at noon, the values of atomic oxygen density are in reasonable agreement with the measurements of Fig. 2-1 for altitudes  $\geq 90$  km at midlatitudes. Shimazaki and Laird [SL-72a] have also computed O-atom profiles for  $60^\circ\text{N}$ , summer-noon conditions; in this calculation, their model was updated for cross-section data, temperature profiles and the eddy-diffusion profile; the latter profile was brought into closer agreement with observations, particularly by eliminating the constant value of the eddy-diffusion coefficient above 100 km and replacing it with a coefficient which rapidly declines with altitude for altitudes above about 100-110 km. The oxygen atom profile shown in Fig. 2-1 now reaches a peak just above 90 km and at higher altitudes declines more rapidly than other observational or calculational data with the exception of the data of Golomb and Good [GG-72]. Although calculations [SL-72a] were made for summer and winter conditions, only the summer data are plotted; the large seasonal difference found in the calculations [SL-72a] may not be true due to the neglect of meridional circulations. Note that differences between summer and winter results were to some extent due to the different number of daylight hours.

The model calculations by George et al. [GZ-72a] are shown on Fig. 2-1 for 30°N, noontime with a turbopause at 94 km. Their major contribution is to use more realistic eddy diffusion coefficient profiles and to examine the effect of changing the altitude of the turbopause. Above 95 km, agreement is not good with the observational data shown on Fig. 2-1 but they would probably obtain better agreement if the turbopause altitude were raised as can be deduced from their results for turbopauses at 94 and 102 km (with the exception that the peak O-density discrepancy between calculations and experiments would become larger).

In the model calculations of Thomas and Bowman [TB-72], the assumption of diffusive equilibrium at the upper boundary was avoided for the species O, O<sub>2</sub> and H<sub>2</sub> by allowing fluxes of these species across the upper boundary. Their eddy-diffusion coefficient profile was similar, qualitatively, to that of Shimazaki and Laird [SI-72a] for summer conditions but had a smaller peak value. As seen on Fig. 2-1, their calculated oxygen atom densities are clearly lower than most other plotted data; the conditions of the calculations were 45°N at noon. They concluded that a lower eddy diffusion coefficient would yield better agreement with the preliminary data of Henderson [He-71] but their eddy-diffusion coefficient was already smaller than that of George et al. [GZ-72a] whose calculations are in better agreement with the final data of Henderson [He-74a]. Clearly a thorough comparison of model calculations is required to aid understanding the differences in model calculations.

A consistent modelling of effects of diffusion (molecular and eddy) on neutral composition (O included) and temperature is that by Chandra and Sinha [CS-74a]. They carried out a parameter study and from their results [CS-74a, Figs. 2 and 4] one sees that the maximum value of  $K_M$  (eddy diffusion coefficient) and the altitude of the turbopause,  $Z_m$ , have little effect on the densities below 100 km (their study



extends to 85 km). These results are different from those of George et al. [GZ-72a] where a distinct difference in the atomic oxygen profile [GZ-72a, Fig. 6] occurs for various  $Z_m$  at altitudes up to and above 100 km. Furthermore the peak O-densities occur at about 90 km in the calculations of Chandra and Sinha [CS-74a] for  $Z_m = 105$  to 120 km, but at 105 or 87 km in the calculations of George et al. [GZ-72a] for  $Z_m = 102$  or 112 km, respectively.

Of the profiles presented by Chandra and Sinha [CS-74a], all have peak densities at about 90 km of  $1.7 \times 10^{12} \text{ cm}^{-3}$ , considerably greater than any measurements or other model calculations of Fig. 2-1.

### 2.2.3 Selection of Atomic Oxygen Profile

In selecting an atomic oxygen profile, reliance was placed on experimental results for altitudes of 90 to 120 km. At each selected altitude, an average oxygen density was computed from the experimental values; these values and the computed averages are listed in Table 2-1. The rocket experiments were given a greater weight than the satellite experiments by a factor of two on the basis of the more direct nature of the rocket measurement techniques. Also, in accounting for the satellite data, not only were the upper limit oxygen densities derived from photometer data [DG-73] included (see above discussion) but also the lower limit oxygen densities of these photometer data [DG-73, Fig. 19].

The atomic oxygen profile was selected before the publication of the extensive measurements of Dickinson et al. [DB-74a] and these measurements were therefore not included in the selection process. Note that in the altitude range from 95 to 115 km, the data of Dickinson et al. [DB-74a] deviate by no more than 15 percent from the atomic oxygen densities of the selected profile.

Table 2-1. Average Values of Oxygen Atom Densities for Altitudes of 90 km and Greater (derived from rocket and satellite data).

A. Rocket Data (R)

h, km	He-74a	OD-73a	OG-73	SO-74b	GG-72 <sup>a</sup>	GG-72 <sup>b</sup>	$\langle R \rangle$	$\frac{2\langle R \rangle + \langle S \rangle}{3}$
90	3.0(11)	2.6(11)	-	-	6.6(10)	2.8(11)	2.3(11)	1.7(11)
95	6.9(11)	5.0(11)	-	3.9(11)	5.2(11)	4.8(11)	5.2(11)	4.6(11)
100	6.4(11)	4.6(11)	-	6.2(11)	3.4(11)	2.3(11)	4.6(11)	4.3(11)
105	3.3(11)	3.0(11)	-	5.7(11)	c	c	4.0(11)	3.3(11)
110	1.6(11)	2.0(11)	-	4.0(11)	c	c	2.5(11)	2.0(11)
115	8.3(10)	-	-	2.4(11)	c	c	1.7(11)	1.3(11)
120	5.0(10)	-	1.0(11)	-	c	c	7.5(10)	6.3(10)

B. Satellite Data (S)

h, km	(DG-73) <sub>max</sub>	(DG-73) <sub>min</sub>	Do-74	$\langle S \rangle$
90	2.2(10)	1.9(9)	1.4(11)	5.5(10)
95	5.0(11)	2.1(11)	2.7(11)	3.3(11)
100	4.3(11)	2.2(11)	2.4(11)	3.0(11)
105	2.5(11)	1.6(11)	1.6(11)	1.9(11)
110	1.4(11)	1.0(11)	1.0(11)	1.1(11)
115	7.4(10)	6.0(10)	6.4(10)	6.6(10)
120	4.1(10)	3.5(10)	3.7(10)	3.8(10)

<sup>a</sup>For 59°N flight.

<sup>b</sup>For 22°N flight.

<sup>c</sup>For altitudes > 100 km, data not considered as a result of possible local atmospheric motions.

The atomic oxygen profile based on data in Table 2-1, is compared with a model of Moe [Mo-73] in Table 2-2 and Fig. 2-2 for the altitude range 90-120 km. Moe had fewer experimental results to consider and used both model calculations and experimental results to arrive at his model. Both model profiles have peaks at about 97 km but the peak-density of the distribution of Moe is about twice that obtained in the present review.

## 2.3 ATOMIC OXYGEN DENSITIES BETWEEN 40 AND 90 KM

### 2.3.1 Model Calculations

Below 90 km, only model calculations are generally available for oxygen atom densities. Those calculations which take into account transport phenomena, extend down to 40 km at the lowest altitude considered. Below 40 km, transport processes are not included in the available calculations which yield oxygen atom densities.

Below about 85 km, a significant diurnal variation in atomic oxygen densities is calculated. For the present models, the diurnal variation will be simplified by selecting one model for noon and one for midnight conditions.

Table 2-2. Comparison of Atomic Oxygen Profile of Table 2-1 with Model Profile of Moe [Mo-73].

Altitude, km	Atomic Oxygen Densities, $\text{cm}^{-3}$	
	Table 2-1	Moe
90	1.7(11)	1.4(11)
95	4.6(11)	9.0(11)
100	4.3(11)	7.0(11)
110	2.0(11)	2.1(11)
120	6.3(10)	9.6(10)



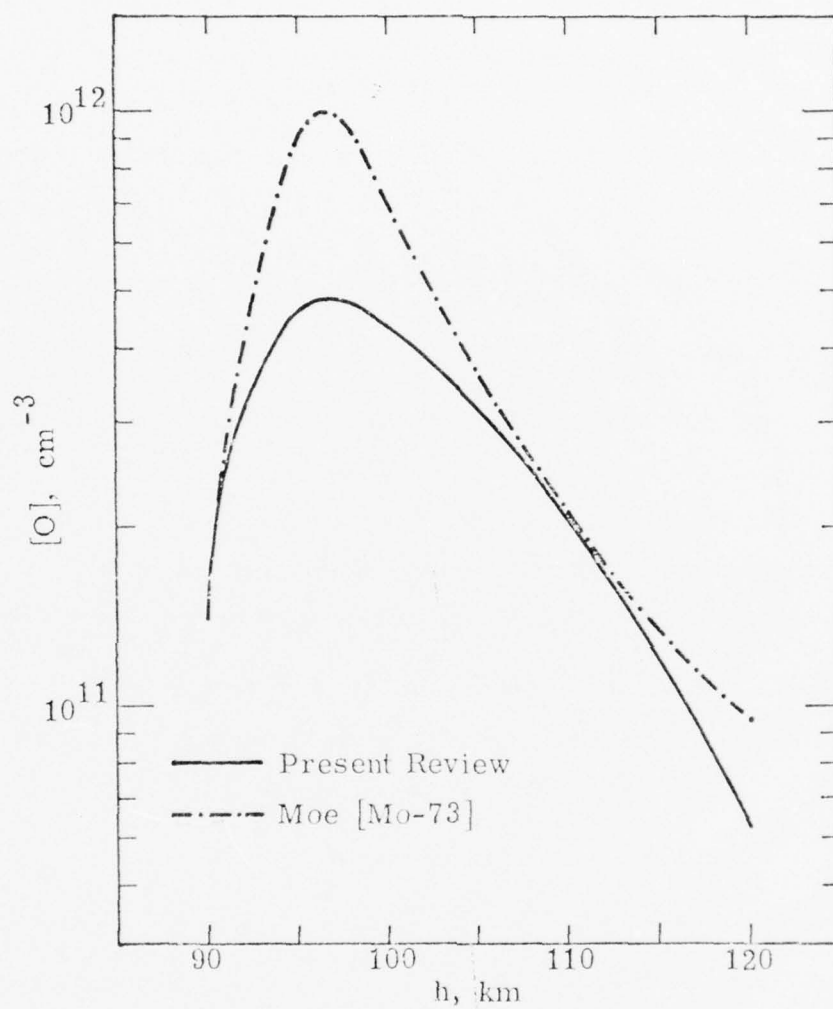


Fig. 2-2. Comparison of Atomic Oxygen Profile of Table 2-1 with Model Profile of Moe [Mo-73].

2.3.1.1 Daytime Densities. Between 40 and 90 km, we consider the five recent model calculations of Hunt [Hu-73a], Thomas and Bowman [TB-72], Shimazaki and Laird [SL-70a, SL-72, SL-72a] and George, Zimmerman and Keneshea [GZ-72a]. The calculations of George et al. [GZ-72a] show that profile densities are relatively insensitive between 80 and 90 km to the turbopause altitude; thus in this range the model calculations are more likely to agree. This is shown to be the case in Fig. 2-3 only approximately. At 80 and 85 km all calculations apply to noon and there is no correlation with altitude of the spread in calculated densities. Also, no simple correlation with gross chemical composition seems to distinguish the calculations; hydrogen-oxygen systems were used by Thomas and Bowman [TB-72] and George et al. [GZ-72a], a hydrogen-oxygen-nitrogen system by Shimazaki and Laird [SL-70a, SL-72, SL-72a] and a hydrogen-oxygen-nitrogen-carbon system by Hunt [Hu-73a]. The maximum eddy diffusion coefficient was of order  $10^7 \text{ cm}^2 \text{ sec}^{-1}$  in the calculations of George et al. [GZ-72a] and Shimazaki and Laird [SL-72a (and SL-70a)] whereas in the calculations of Thomas and Bowman [TB-72] and Hunt [Hu-73a], the maximum was of order  $10^6 \text{ cm}^2 \text{ sec}^{-1}$ . In the calculations of Shimazaki and Laird [SL-70a] and Hunt [Hu-73a], the eddy diffusion coefficients were given constant values above 100 km and this is not reasonable [SL-72a]. If we choose for consideration only those calculations which have an eddy diffusion coefficient profile and maximum value consistent with observations [SL-72a], then the calculations of Shimazaki and Laird [SL-72a] and George et al. [GZ-72a] are selected. That this is a justifiable procedure cannot be demonstrated with the simple comparisons that have been presented; a much more detailed comparison of the calculations is required and perhaps considerations beyond the scope of any of these calculations.

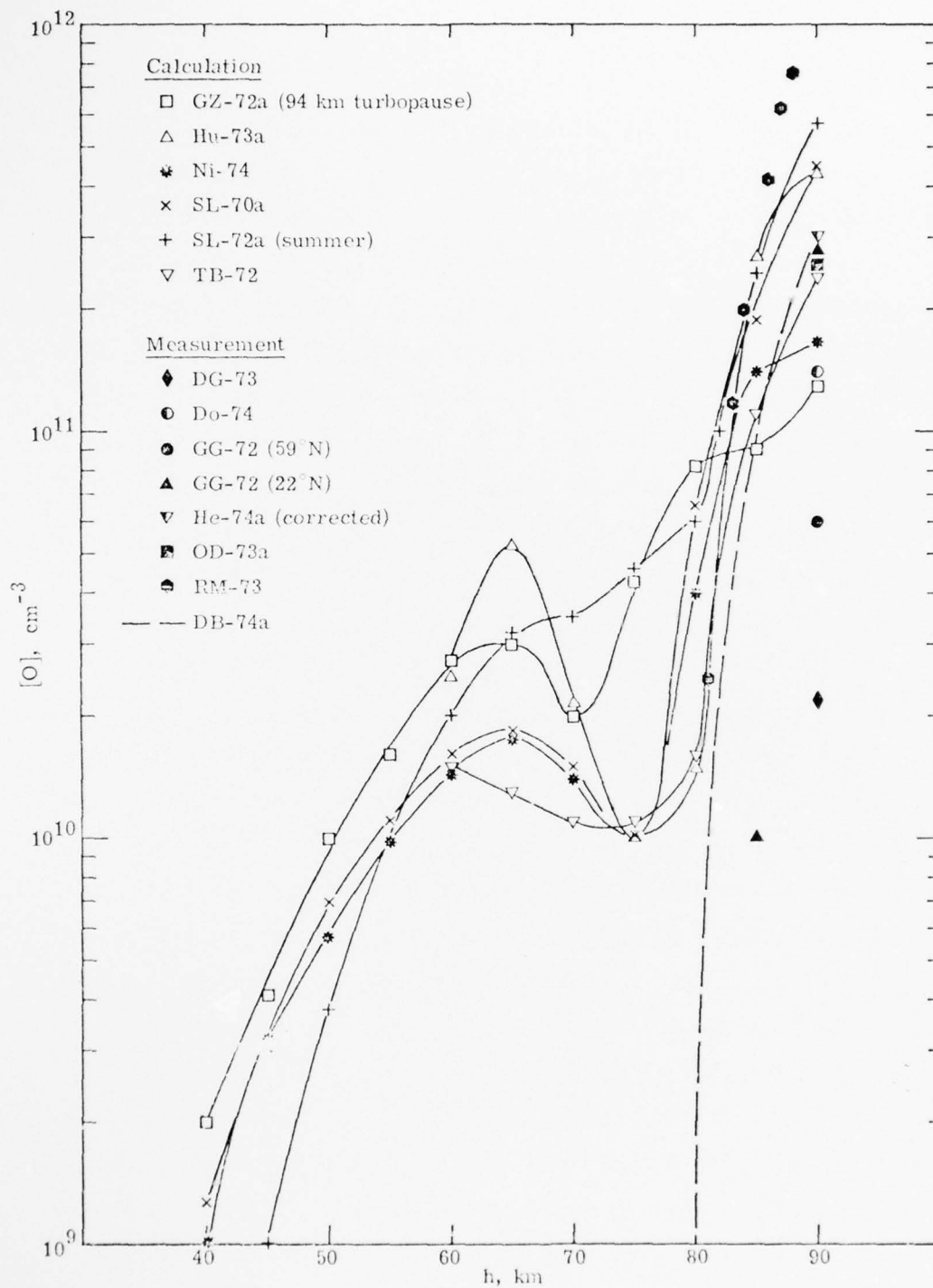


Fig. 2-3. Atomic Oxygen Densities Between 40 and 90 km.

Below 60 km, the calculations of George et al. [GZ-72a] show that the turbopause altitude has no effect on the oxygen atom density. Thus all model calculations could be included in the selection process but the calculations of Thomas and Bowman [TB-72] and Hunt [Hu-73a] extend only to 60 km. In the altitude range below about 50 km, the calculations of Nicolet [Ni-71a] are important. These calculations are based on photochemical equilibrium and the oxygen atom density is calculated by using an ozone profile consistent with observations of the ozone densities.

**2.3.1.2 Nighttime Densities.** Of the recent model calculations, only those of Shimazaki and Laird [SL-70a, SL-72a] and Thomas and Bowman [TB-72] yield nighttime profiles. The altitude at which the calculated oxygen atom densities depart from the daytime values is between 80 and 85 km. In all cases, the oxygen atom density is negligibly small by 60 km. A recent measurement [DB-74a] of the nighttime atomic oxygen density in the altitude range from 79.6 to 90 km is shown on Fig. 2-3. The departure from the daytime values between 80 and 85 km predicted by the calculations [SL-70a, SL-72a, TB-72] is substantiated by the measurements [DB-74a]. The predicted rapid fall in oxygen density is also confirmed by the measurements which show the density to be less than  $3 \times 10^7 \text{ cm}^{-3}$  below 79.6 km. Additional oxygen atom densities shown on Fig. 2-3 between 80 and 90 km are derived [RM-73] from OH volume emission profiles.

### **2.3.2 Selection of Atomic Oxygen Profile**

On the basis of the calculations of Shimazaki and Laird [SL-72a] for summer noon at 60°N and of George et al. [GZ-72a] for noon at 30°N, an average daytime oxygen density is calculated over the mutual range of altitudes of the two calculations, i. e., between 40 and 90 km.

In the range of altitudes between 40 and 50 km, the photochemical equilibrium calculations of Nicolet [Ni-71a] are also included. Furthermore, the rocket observation of Golomb and Good [GG-72] at 85 km for 59°N is included. The data and computed averages are given in Table 2-3.

For the nighttime oxygen atom profiles, the average of the values of the calculations of Shimazaki and Laird [SL-70a, SL-72a] are chosen in the overlap altitudes of these calculations as given in Table 2-3. Below 75 km, the selected oxygen atom densities are calculated on the basis of an exponential decline from the atomic oxygen density at 75 km as indicated in Section 2.5 below. The calculations of Thomas and Bowman [TB-72] are for pre-sunrise and post-sunset conditions; however, above about 78 km, the profiles for pre-sunrise and post-sunset conditions are essentially the same and yield lower densities than do the calculations of Shimazaki and Laird [SL-70a, SL-72a] by up to three orders of magnitude at 78 km. At 85 km, these calculations [TB-72, SL-72a] differ by a factor of 2.5.

## 2.4 ATOMIC OXYGEN DENSITIES BELOW 40 KM

### 2.4.1 Selection of Atomic Oxygen Profile

Below 40 km, the calculated oxygen atom density continues to decline rapidly. We rely on the calculations of Nicolet [Ni-71a] to an altitude of 20 km; see Table 2-4a. The method of obtaining these densities has been mentioned above. The calculations are for an overhead sun. In the calculations, no significant effect of hydrogenous constituents on the oxygen atom densities was found below 50 km.

Below 20 km, the calculations of Nicolet [Ni-72b] were extended by assuming equilibrium between photodissociation of  $O_3$  and

Table 2-3. Average Values of Oxygen Atom Densities for Altitudes from 40 to 85 km.

Daytime Conditions

h, km	GZ-72a	SL-72a	$\langle M \rangle^{\dagger}$	GG-72	$\langle M+E \rangle^{\dagger}$	Ni-71a	$\langle M \rangle^{\dagger}$
85	9.1(9)	2.4(11)	1.6(11)	1.0(10)	1.1(11)		
80	8.1(9)	6.1(10)	7.1(10)				
75	4.3(10)	4.6(10)	4.5(10)				
70	2.0(10)	3.5(10)	2.8(10)				
65	3.0(10)	3.2(10)	3.1(10)				
60	2.8(10)	2.0(10)	2.4(10)				
55	1.6(10)	1.0(10)	1.3(10)				
50	1.0(10)	3.8(9)				6.4(9)	6.7(9)
45	4.2(9)	1.0(9)				3.6(9)	2.9(9)
40	1.5(9)	1.3(8)				1.3(9)	9.8(9)

Nighttime Conditions

h, km	SL-72a	SL-70a	$\langle M \rangle^{\dagger}$
85	2.5(11)	-	$2.5(11)^{\ddagger} \rightarrow 1.7(11)$
80	1.4(10)	4.5(10)	3.0(10)
75	2.1(8)	7.6(8)	4.9(8)
70	-	3.2(5)	3.2(5)
65	-	5.0(1)	5.0(1)
60	-	1.0(0)	1.0(0)

M  $\equiv$  model calculations.

$^{\dagger}\langle X \rangle$  = average, where meaningful, of values in leftward columns.

M+E  $\equiv$  model calculations + experiment.

$^{\ddagger}$  Choose nighttime density  $\equiv$  daytime density.



Table 2-4. Calculated Values of Atomic Oxygen Densities Below 40 km.

a. 20-40 km

h, km	[O], cm <sup>-3</sup>	Ref.
35	2.6(8)	Ni-71a
30	4.5(7)	Ni-71a
25	7.0(6)	Ni-71a
20	1.0(6)	Ni-71a

b. 0-20 km

h, km	[O], cm <sup>-3†</sup>		⟨[O]⟩, cm <sup>-3</sup>
	a	b	(a+b)/2
15	2.61(5)	1.2(5)	1.9(5)
10	2.91(4)	1.46(4)	2.2(4)
5	7.7(3)	4.74(3)	6.2(3)
0	6.6(0)	4.9(0)	5.8(0)

where

$$[O] = \frac{[O_3]}{k[O_2]} \left[ \frac{3 \times 10^{-9} k'}{1 + \frac{k[O_3]}{J}} + \frac{J'}{[M]} \right]$$

with

$k$  = rate coefficient for reaction  $O + O_2 + M \rightarrow O_3 + M$ ;  $M = O_2, N_2$ , see Ni-72b.

$k'$  = rate coefficient for reaction  $NO + O_3 \rightarrow NO_2 + O_2$ ;  $k = 10^{-12} \exp(-1250/T)$ , see Ni-72b.

$J = 0.01 \exp(-0.38) = 6.84(-3)$  for  $\sec \chi = 1$ , see Ni-72b.  $NO_2 + h\nu \rightarrow NO + O$ .

$J' = 3.7(-4)$ ;  $O_3 + h\nu (3000\text{\AA} < \lambda < 11800\text{\AA}) \rightarrow O_2 + O(^3P)$ ; see Le-72a.

and

h, km	T, °K <sup>‡</sup>	[M], cm <sup>-3*</sup>	k, cm <sup>6</sup> sec <sup>-1**</sup>		k', cm <sup>3</sup> sec <sup>-1**</sup>	[O <sub>3</sub> ], cm <sup>-3††</sup>
			a	b		
15	217	4.05(18)	1.1(-33)	2.4(-33)	3.15(-15)	2.60(12)
10	223	8.64(18)	1.0(-33)	2.0(-33)	3.68(-15)	1.13(12)
5	256	1.53(19)	7.7(-34)	1.25(-33)	7.58(-15)	5.68(11)
0	288	2.55(19)	6.25(-34)	8.50(-34)	1.3(-14)	~1(9)

<sup>†</sup> Upper and lower values of [O] calculated using the tabulated upper and lower values of  $k$ .

<sup>‡</sup> Midlatitude model, US-66, p. 119.

\*US-62, p. 71.

\*\*Ni-72b.

††Ca-74.

recombination of O via  $O + O_2 + M$ . The ozone densities recommended by Cadle [Ca-74] were adopted for this calculation and the particle densities were from the U. S. Standard Atmosphere [US-62]; see Table 2-4b. Levy [Le-72a, Le-73] has also calculated species densities in the troposphere but the input data he uses are not the most reliable data available.

## 2.5 ATOMIC OXYGEN PROFILE BETWEEN 0 AND 120 KM

The composite oxygen atom densities are shown in Table 2-5 and Fig. 2-4 between 0 and 120 km for noon and midnight conditions. Extrapolation of the profile from 120 to 130 km is included to aid fitting profiles for altitudes above 120 km to the profile given in Table 2-5 and Fig. 2-4. The profile is for midlatitudes with no seasonal or latitudinal variations taken into account.



Table 2-5. Atomic Oxygen Profile to 120 km for Noon and Midnight Conditions.

h, km	[O], cm <sup>-3</sup>		h, km	[O], cm <sup>-3</sup>	
	Noon	Midnight		Noon	Midnight
0	5.8(0)	1.1(0)	70	2.8(10)	6.3(5)*
5	6.2(3)	↓	75	4.5(10)	4.9(8)
10	2.2(4)		80	7.1(10)	3.0(10)
15	1.9(5)		85	1.1(11)	9.0(10)
20	1.0(6)		90	1.7(11) <sup>‡</sup>	1.7(11) <sup>‡</sup>
25	7.0(6)		95	4.6(11)	4.6(11)
30	4.5(7)		100	4.3(11)	4.3(11)
35	2.6(8)		105	3.3(11)	3.3(11)
40	9.8(8)		110	2.0(11)	2.0(11)
45	2.9(9)		115	1.3(11)	1.3(11)
50	6.7(9)		120	6.3(10)	6.3(10)
55	1.3(10)		125 <sup>†</sup>	4.4(10)	4.4(10)
60	2.4(10)	1.1(0)*	130 <sup>†</sup>	3.7(10)	3.7(10)
65	3.1(10)	8.2(2)*			

<sup>†</sup> The data at 125 and 130 km are extrapolations of the data at lower altitudes and are meant to be used for fitting the profile below 120 km to the atomic oxygen profile above 120 km.

<sup>‡</sup> Noon and midnight values are identical above 85 km.

\* Based on  $[O] = [O]_{75} \exp[-1.33(75 - h)]$  where  $[O]_{75} = 4.9(8) \text{ cm}^{-3}$ .

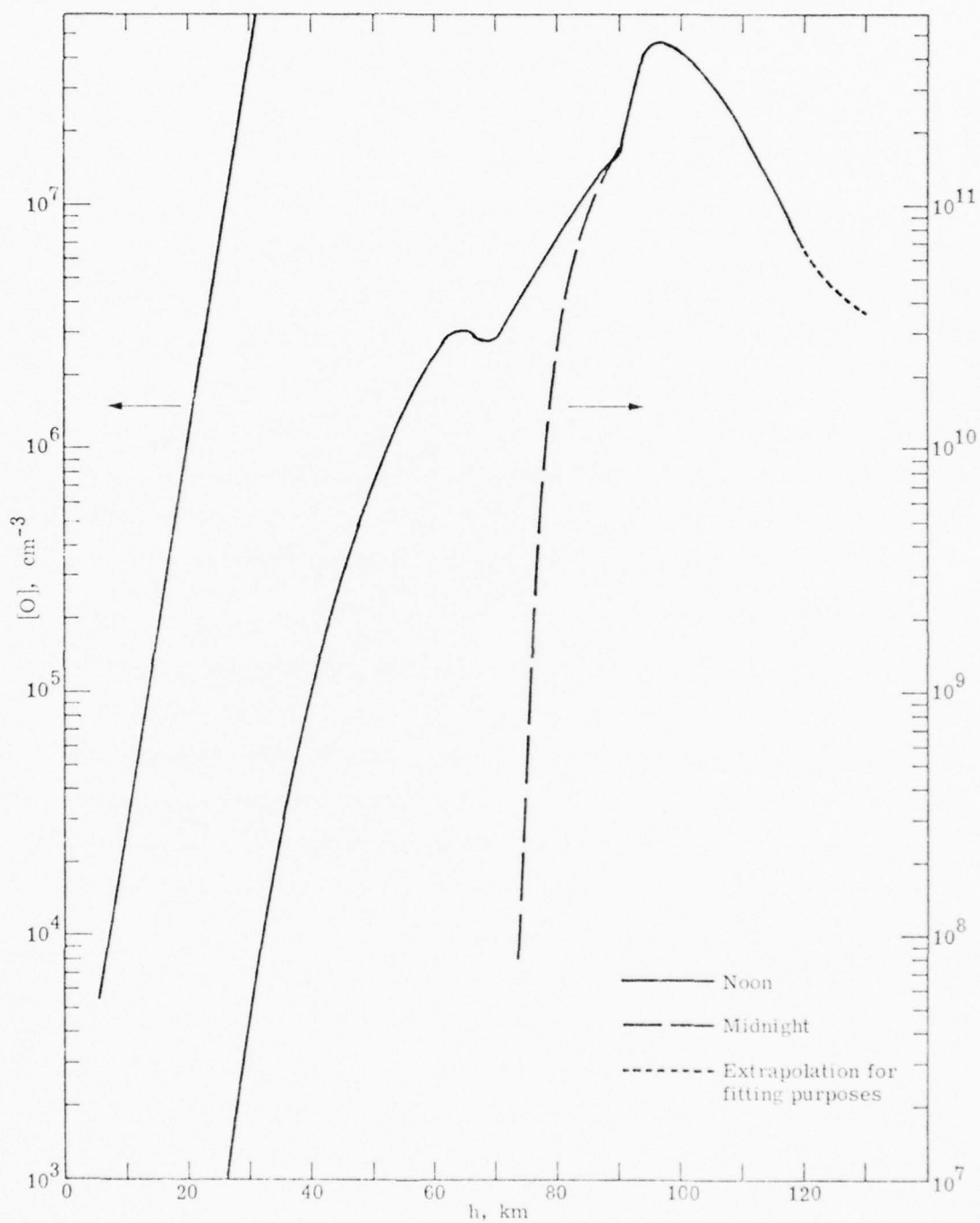


Fig. 2-4. Atomic Oxygen Profile Between 0 and 120 km for Noon and Midnight Conditions.

### 3. DENSITY PROFILE OF MOLECULAR OXYGEN, $O_2(a^1\Delta_g)$

#### 3.1 INTRODUCTION

A midlatitude profile for the first, excited state of molecular oxygen,  $O_2(^1\Delta_g)$ , is selected for altitudes from ground level to beyond 140 km. Fortunately, measurements have been made between 30 and 120 km in the altitude range of principal interest for  $O_2(^1\Delta_g)$ . At other altitudes, as well as the edges of the stated range, reliance has to be placed on model calculations. The measurements of  $O_2(^1\Delta_g)$  profiles have been mainly made at latitudes near  $60^\circ N$  so that latitudinal or hemispherical variations in the profiles have not been established. Also in the preliminary stage is understanding of the seasonal variation of the  $O_2(^1\Delta_g)$  densities.

The measured profiles of  $O_2(^1\Delta_g)$  at altitudes above approximately 50 km are of interest also in connection with the profiles of ozone at these higher altitudes. The photodissociation of ozone below 90 km is the principal source of  $O_2(^1\Delta_g)$ . Since measurements of ozone densities have not been extensively made at altitudes in excess of 70 km, the profile of  $O_2(^1\Delta_g)$  between 70 and 90 km provides information about the ozone density in this altitude range.

#### 3.2 MEASUREMENTS

Measurements of the (0, 0) band at  $1.27 \mu m$  from the radiative decay of  $O_2(^1\Delta_g)$  [EH-68] were made between 30 and 110 km on a rocket flight at  $32^\circ N$  latitude in October 1966. These measurements are shown on Fig. 3-1; a primary peak near 50 km and a secondary peak near 85 km are observed. The overhead emission on this flight is in fair

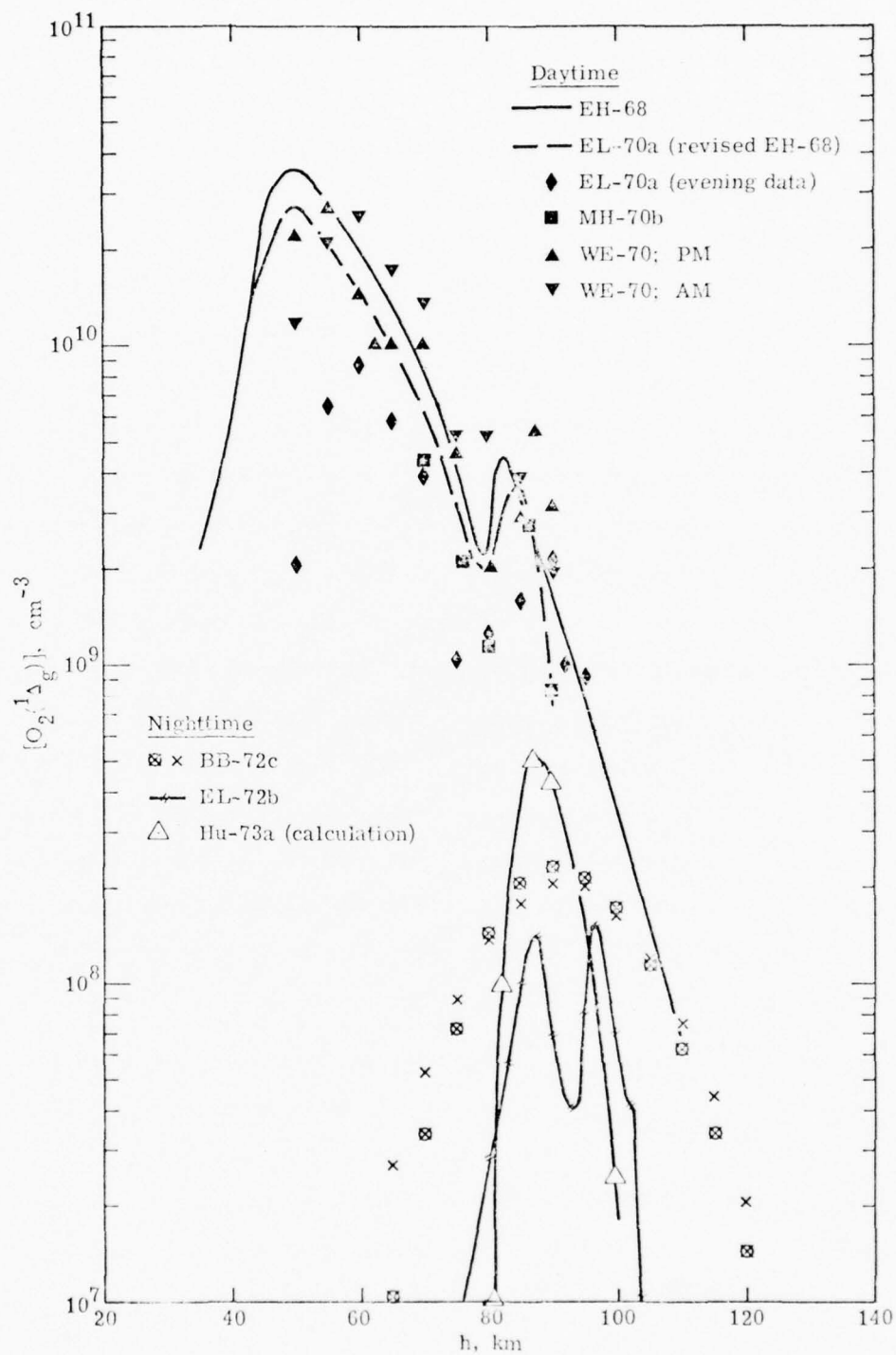


Fig. 3-1. Measured  $O_2(^1\Delta_g)$  Densities Between 30 and 120 km.

agreement with an earlier balloon measurement [EL-67]. Above 80 km, the detector noise for the rocket flight data became large so that errors of factors of 2 and 5 at 90 and 110 km were possible. The rocket flight measurements of Evans et al. [EH-68] were later normalized [EL-70a] to agree with the balloon observations [EL-69]; the revised data are shown on Fig. 3-1 by the dashed line (note that the shift in the secondary peak may be the result of the choice of data represented by the solid line rather than by the dotted line of Fig. 4b of EH-68). Measurements at the higher latitude of 59°N by Wood et al. [WE-70], presumably using the same procedures as Evans et al. [EH-68], have been made for morning and afternoon conditions in July 1967. A shift in the primary  $O_2(^1\Delta_g)$  peak density to higher altitudes (i. e. , 55 to 60 km) is found but the peak densities are comparable to the normalized densities [EL-70a] of the lower latitude (32°N) data. In the measurements of Wood et al. [WE-70], evidence for a secondary layer between 80 and 90 km was obtained. Preliminary data of Wood [EL-70a] for evening measurements are shown in Fig. 3-1; these data yield lower densities than the daytime measurements at altitudes below about 90 km but the two-layer structure of the  $O_2(^1\Delta_g)$  profile is again found. Companion morning measurements [EL-70a] between 70 and 100 km are not significantly different from the evening measurements.

Rocket measurements of Megill et al. [MH-70b] between 70 and 90 km are in qualitative agreement with the normalized values of  $O_2(^1\Delta_g)$  of Evans and Llewellyn [EL-70a] but are significantly smaller in absolute values between 76 and 84 km while having satisfactory agreement otherwise, as shown on Fig. 3-1. These measurements were obtained at 59°N latitude at 0100 UT.



The secondary  $O_2(^1\Delta_g)$  layer was observed with peak intensity at  $80 \pm 5$  km on a rocket flight [HM-73g] in the region of the equator after local sunset; the peak intensity was found to decay with time after sunset and varied from about  $1.8 \times 10^9 \text{ cm}^{-3}$  to  $8.0 \times 10^8 \text{ cm}^{-3}$  during the observations. An apparent latitudinal variation of  $O_2(^1\Delta_g)$  emission was detected over the latitude range of 0 to  $14^\circ$  S.

The decay of both layers of  $O_2(^1\Delta_g)$  is discussed by Vallance Jones [Va-73a]. The lower layer with peak density near 50 km decays within about 10 minutes after solar illumination ceases whereas the upper layer with peak density near 85 km decays in a characteristic time of about 60 minutes, approximately the radiative lifetime of  $O_2(^1\Delta_g)$ . The former, rapid decay is a result of quenching at the lower altitudes [EW-70].

Nighttime measurements [EL-72b, BB-72c] have detected only a single  $O_2(^1\Delta_g)$  layer centered about 90 km. Rocket measurements at  $59^\circ$  N between 70 and 110 km have shown a double peaked profile as exhibited on Fig. 3-1; these investigators [EL-72b] consider the possibility that a single, broad distribution for the  $O_2(^1\Delta_g)$  density profile could form under other atmospheric conditions. By contrast, Bishop et al. [BB-72c] found only a single peaked layer between 70 and 110 km; these investigators considered the possible enhancement of the measured  $1.27 \mu\text{m}$  radiation by auroral phenomena (although a lack of enhancement is indicated by aspects of the observations). The enhancement factor is apparently not relevant to the measurements of Evans et al. [EL-72b].

On the basis of ground-based twilight observations of the  $1.27 \mu\text{m}$  radiation, Evans and Llewellyn [EL-72a; see also EW-70] deduce a seasonal variation of the  $O_2(^1\Delta_g)$  layer density in the 80-90 km layer for which a minimum occurs in mid-summer and a maximum in mid-winter.

The variation of the daytime intensity was found not to be different [EL-69]. A similar seasonal variation has been reported [VG-63] from observations of the  $1.58 \mu\text{m}$  radiation (the (0,1) band from radiative decay of  $\text{O}_2(^1\Delta_g)$ ); a maximum in intensity was found around January and a minimum in the summer. These measurements [VG-63] were evening twilight measurements at  $52^\circ\text{N}$ . Note, however, that a clear seasonal variation is not evident in the compilation of twilight and day airglow density profiles presented by Vallance Jones [Va-73a] in the altitude range of 80 to 90 km. For the lower  $\text{O}_2(^1\Delta_g)$  layer, no seasonal variation is evident [EL-72a].

Diurnal measurements of  $\text{O}_2(^1\Delta_g)$  densities above 30 km have been made by Evans et al. [EL-67, EL-69]; these show a relatively rapid rise and decline at twilight and a slowly varying emission during the day with a peak density at noon. This is consistent with the comparisons of Haslett et al. [HM-69c] in which the integrated intensity measurements for the  $1.27 \mu\text{m}$  radiation of several groups of investigators for restricted intervals of solar zenith angle are combined.

### 3.3 MODEL CALCULATIONS

Very simple photo-equilibrium calculations by Vlasov [Vl-69] and by Evans and Llewellyn [EL-70a] are in good agreement with measurements [EH-68, EL-70a] between 30 and 75 km. These calculations require an ozone density profile as input but otherwise take into account only the photodissociation of ozone and the de-excitation of  $\text{O}_2(^1\Delta_g)$ . Note that Evans and Llewellyn [EL-70a] assume that  $\text{O}_2(^1\Delta_g)$  is formed by photodissociation of ozone at wavelengths greater than  $2660 \text{ \AA}$  whereas Vlasov [Vl-69] may have accounted for photodissociation at wavelengths greater than  $2100 \text{ \AA}$ . Comparison of these calculations with the experimental data is shown on Fig. 3-2.

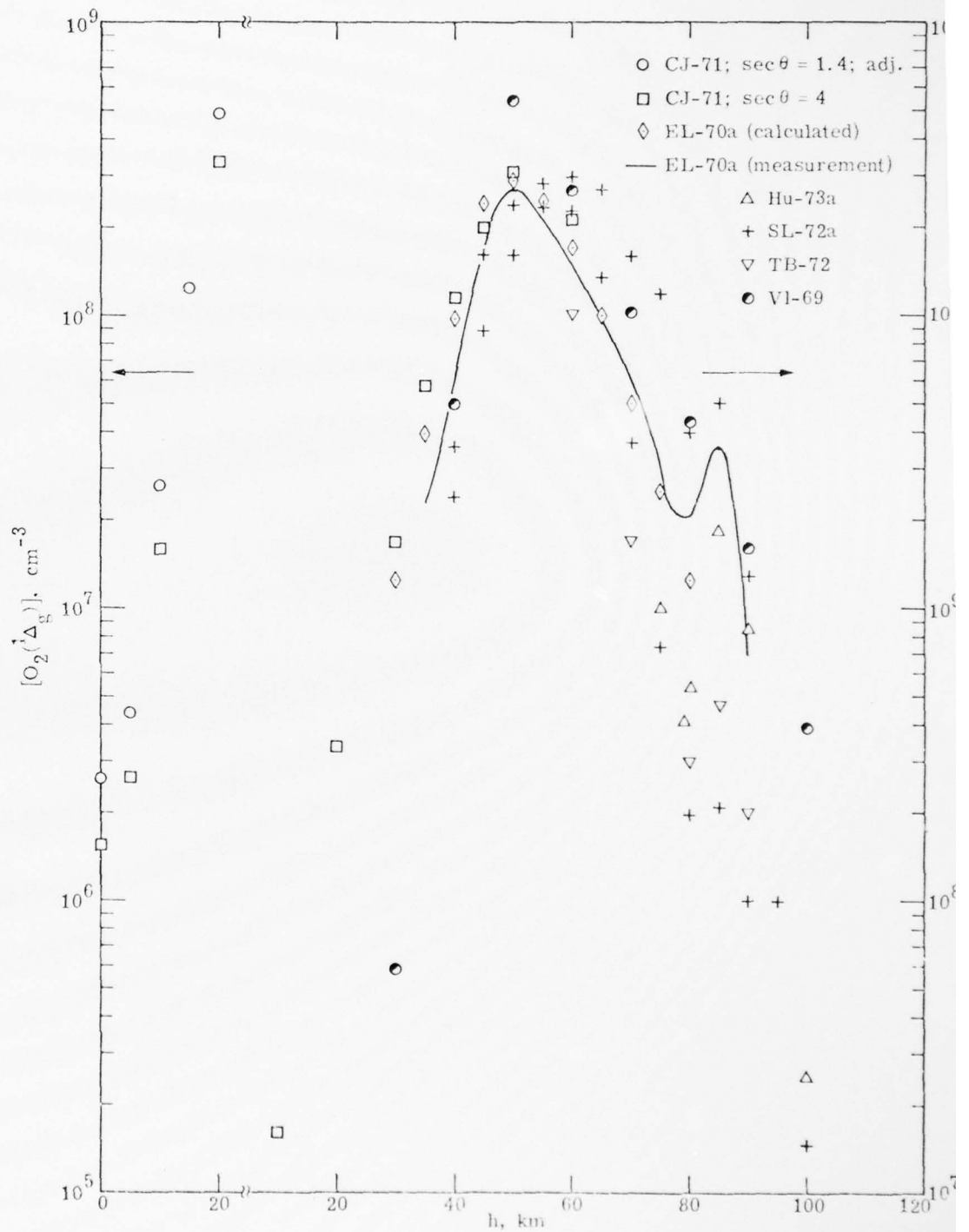


Fig. 3-2. Calculated  $O_2(^1\Delta_g)$  Densities Between 0 and 100 km.

The very extensive calculations of Hunt [Hu-73a] yield  $O_2(^1\Delta_g)$  profiles with density values significantly smaller than observations [EL-70a] in the range 75 to 85 km. This discrepancy is attributed [Hu-73a] to deficiencies in the model ozone densities which are apparently too small above 70 km. Likewise, the calculations of Thomas and Bowman [TB-72] yield values of  $O_2(^1\Delta_g)$  density significantly smaller than observed values, see Fig. 3-2, and this discrepancy can apparently also be traced to small values of the calculated ozone density above 60 km. However, both the calculations of Hunt [Hu-73a] and of Thomas and Bowman [TB-72] are in qualitative agreement with observations and do predict the occurrence of the second  $O_2(^1\Delta_g)$  layer with peak density at 85 km; this prediction results from the inclusion of hydrogenous species in the chemistry for these calculations. The calculations of Turco and Sechrist [TS-72b] are not in qualitative agreement with the observations [EL-70a]. By contrast, the midnight  $O_2(^1\Delta_g)$  profile of Hunt [Hu-73a] has larger density values in the altitude range between 85 and 95 km than observations as shown on Fig. 3-1.

The calculations of Shimazaki and Laird [SL-72a] for  $60^\circ N$  latitude shown on Fig. 3-2 are in fair agreement with the measurements of Wood et al. [WE-70] (see Fig. 3-1). The peak density occurs at 60 km in the calculation and at 55 and 60 km in the afternoon and morning measurements of Wood et al. [WE-70]; since the measurements [WE-70] were in July, they should be compared with the summer calculations of Shimazaki and Laird [SL-72a] (the upper points in the density spread as shown on Fig. 3-2).

Crutzen et al. [CJ-71] have made calculations of the  $O_2(^1\Delta_g)$  profile from 0 to 70 km using recent experimental data. Crutzen et al. took into account the formation of  $O_2(^1\Delta_g)$  at wavelengths below 2660 Å as well as formation of  $O_2(^1\Delta_g)$  via the spin forbidden, ozone photolysis

at wavelengths greater than 3100 Å; the latter process is important for  $O_2(^1\Delta_g)$  production at low altitudes and small zenith angles. The calculations of Crutzen et al. [CJ-71] were made for zenith angles corresponding to sec  $\theta$  values of 4 and 1.4. The latter corresponds to noon at 45°N in spring and the former to zenith angles for the rocket experiments of Evans et al. [EH-68]. The calculations [CJ-71] and experimental results [EL-70a] are in reasonable agreement above 40 km as shown on Fig. 3-2.

Calculations of the diurnal variation of  $O_2(^1\Delta_g)$  densities between 40 and 80 km have been made by Vlasov [Vl-70]; these are in qualitative agreement with observations [EL-67, EL-69, HM-69c].

### 3.4 SELECTION OF $O_2(^1\Delta_g)$ PROFILE

#### 3.4.1 Daytime Densities

In the altitude region between 50 and 90 km, the corrected, observations of Evans et al. [EH-68, EL-70a] are selected for the recommended profile at noon and midlatitudes. These data [EL-70a] are midlatitude data (32°N) but were obtained in the afternoon. However, calculations by Crutzen et al. [CJ-71] indicate that above 55 km, the  $O_2(^1\Delta_g)$  densities do not differ significantly over the range of zenith angles corresponding to the time between noon and the time of the rocket flight [EL-70a]. Also note that the rocket flight [EL-70a] was in October, roughly midway between maximum and minimum of the possible seasonal extremes [EL-69, EW-70, EL-72a] in  $O_2(^1\Delta_g)$ .

Above 90 km, the  $O_2(^1\Delta_g)$  apparently continues to decline; the decline has not been measured in daytime but measurements above 100 km have been made at night; also calculations [Hu-73a] have been extended to 160 km. While the calculations are not in qualitative agreement with



observations between 70 and 90 km, at 90 km, the calculations agree with the corrected data of Evans et al. [EH-68, EL-70a] and are in reasonable agreement with nighttime data [EL-72b]; the calculations show equality of day and night  $O_2(^1\Delta_g)$  densities above 100 km so the previously mentioned agreement is further evidence that the calculations above 90 km may be adequate for the purposes of profile selection. Thus above 100 km, we choose the data from calculations by Hunt [Hu-73a]. At 100 km the nighttime value of the  $O_2(^1\Delta_g)$  density [EL-72b] is chosen for the reference curve, and between 90 and 100 km values of the densities are chosen by interpolation.

Below 55 km, the calculations of Crutzen et al. [CJ-71] indicate that the noon profiles will have consistently larger values of  $O_2(^1\Delta_g)$  densities than those obtained in the afternoon observations of Evans et al. [EH-68]. To account for this, the calculations of Crutzen et al. [CJ-71] have been normalized to the 55 km  $O_2(^1\Delta_g)$  density of the corrected rocket data [EL-70a] and the resulting values between 0 and 50 km chosen as reference data; these data are plotted on Fig. 3-2 where they may be compared with the rocket data.

The composite data for the noon, midlatitude,  $O_2(^1\Delta_g)$  profile are given in Table 3-1 and shown in Fig. 3-3.

#### 3.4.2 Nighttime Densities

Above 100 km we rely on the calculations of Hunt [Hu-73a] which indicate no difference in  $O_2(^1\Delta_g)$  densities between noon and midnight. Below 100 km, the measurements of Evans et al. [EL-72b] are applicable but rather than carry the detailed two-peak profile, we will follow the calculated profile [Hu-73a] but adjust the peak to near the peak values observed [EL-72b, BB-72c], i. e., adjust the peak nighttime

Table 3-1. Profile of  $O_2(^1\Delta_g)$  for Noon and Midnight Conditions.

h, km	$[O_2(^1\Delta_g)], \text{ cm}^{-3}$		h, km	$[O_2(^1\Delta_g)], \text{ cm}^{-3}$	
	Noon	Midnight		Noon	Midnight
0	2.6(6)	3.4(0)	90	1.3(9)	2.0(8)
5	4.4(6)	↓	95	3.0(8)	1.4(8)
10	2.7(7)		100	5.6(7)	5.6(7)
15	1.25(8)		105	4.3(6)	4.3(6)
20	4.9(8)		110	6.2(5)	6.2(5)
25	1.25(9)		115	1.0(5)	1.0(5)
30	2.7(9)		120	1.4(4)	1.4(4)
35	9.0(9)		125	3.3(3)	3.3(3)
40	1.8(10)		130	7.1(2)	7.1(2)
45	2.7(10)		135	2.6(2)	2.6(2)
50	3.5(10)		140	1.0(2)	1.0(2)
55	2.1(10)		145	4.7(1)	4.7(1)
60	1.5(10)		150	2.3(1)	2.3(1)
65	1.0(10)	↓	155	1.2(1)	1.2(1)
70	6.1(9)	3.4(0)	160	6.1(0)	6.1(0)
75	3.1(9)	5.8(2)	165	Constant at 160 km value	
80	2.05(9)	1.0(5)	↓		
85	3.6(9)	8.6(7)			

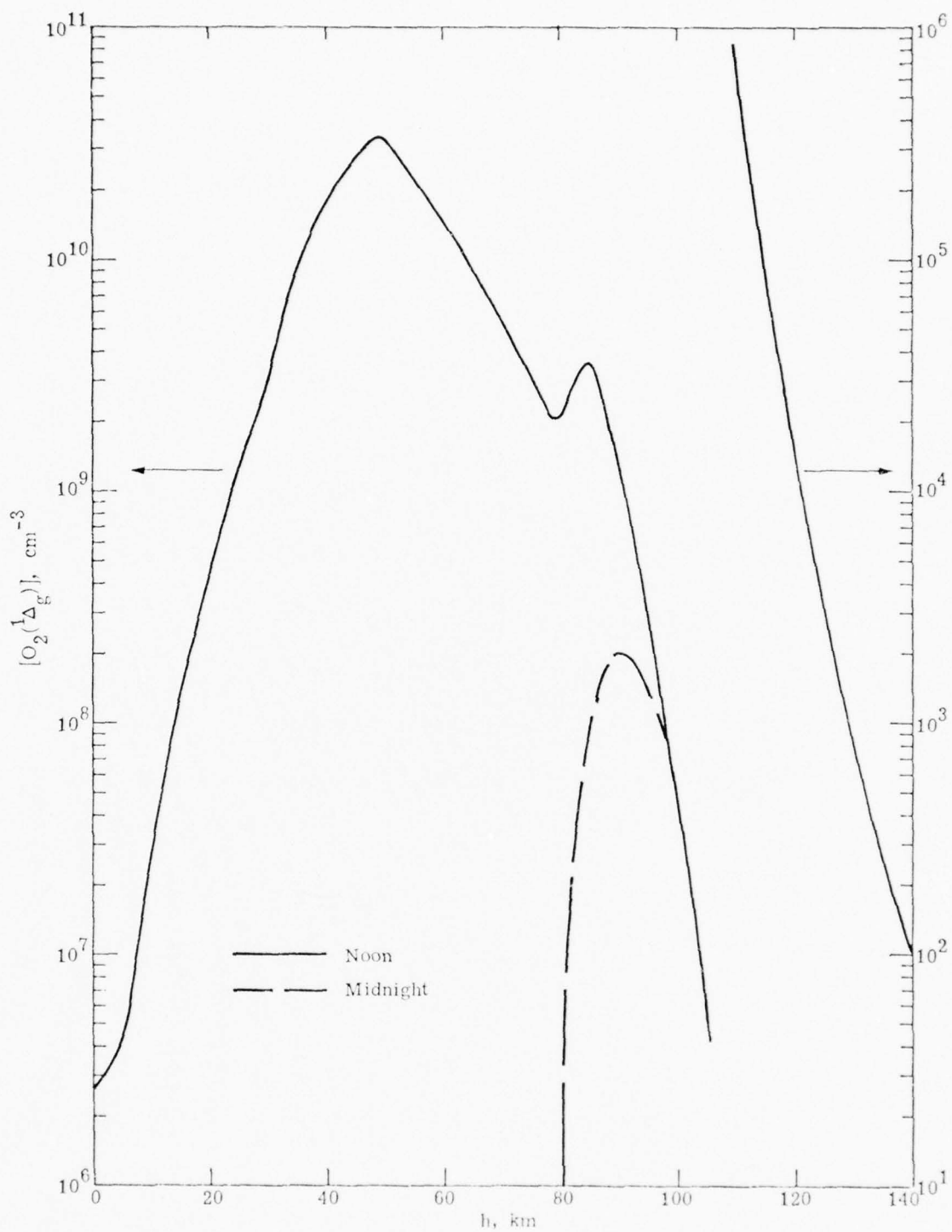


Fig. 3-3. Profile of  $O_2(^1\Delta_g)$  Between 0 and 140 km for Noon and Midnight Conditions.

$\text{O}_2(^1\Delta_g)$  density to a value of  $2 \times 10^8 \text{ cm}^{-3}$  at 90 km. The selected night-time data are given in Table 3-1 and on Fig. 3-3.

## 4. DENSITY PROFILE OF OZONE

### 4.1 INTRODUCTION

The densities of ozone have been extensively measured for altitudes up to 70 km. These measurements demonstrate important variations of the ozone density diurnally, seasonally and with latitude and longitude [Du-71, Du-74, PL-74a]; there is also a significant difference between the ozone distribution in the northern and southern hemispheres [Du-70a]. At lower altitudes, between about 20 and 40 km, vertical and horizontal transport processes dominate the distribution while at greater altitudes, photochemical processes are more important [Ni-74]. Reviews of atmospheric ozone have been given by Dütsch [Du-70a, Du-71, Du-74]. While fewer measurements have been made above 70 km than below, a second ozone layer has been observed above 80 km.

From the available data, a midlatitude ozone profile is formulated for noon and midnight conditions in the northern hemisphere; seasonal and geographical variations are not included in the model.

### 4.2 DAYTIME DENSITIES

#### 4.2.1 Measurements

From the daytime observations, a midlatitude, northern-hemisphere model of the ozone profile has been constructed by Krueger and Minzner and presented prior to publication by Cadle [Ca-74]. This model applies to altitudes up to 72 km for a latitude of 45° N. In the altitude region between 0 and 26 km, the model is the same as that of the U. S. Standard Atmosphere Supplements [US-66]. Between 26 and 34 km, balloon and rocket data were used and above 34 km, rocket data alone were used. Data from only 17 of 37 rocket flights were selected



for use in the model on the basis of accuracy of measurements, height resolution, absence of abnormal geophysical conditions and deviation from the statistical distribution of rocket data. Data from satellite observations based on backscattered UV radiation were used to latitudinally adjust the mean rocket data. The data employed in the model contain no significant longitudinal gradients. Because of the time at which many of the soundings were made, the data for altitudes above 30 km are biased for solar conditions in the years 1968 to 1970, i. e., for solar minimum conditions. The model profile is plotted in Fig. 4-1.

Between 72 and 80 km, two additional measurements [WS-68, RM-63] provide data which are not inconsistent with the model atmosphere profile of Krueger and Minzner; these data are shown in Fig. 4-1. Also, measurements of Krueger as given in Park and London [PL-74a] from altitudes between 70 and 79 km are in agreement with other measurements shown on Fig. 4-1.

Above 80 km, there are few, direct measurements of the ozone density. The results of Rawcliffe et al. [RM-63] extend to about 85 km and indicate a ledge in the ozone density but do not show the maximum in ozone density which recent nighttime [HR-72a, HR-73, SU-74] or sunset [MR-73] measurements reveal. The latter measurements of Miller and Ryder [MR-73] were obtained by an occultation technique from rocket experiments made at 59°N latitude. The ascent and descent profiles are shown on Fig. 4-1; the ascent profile has the larger peak value. These profiles have peak densities between 86 and 89 km. Another ozone profile extending above 80 km has been derived [EL-70a] from a measured  $O_2(^1\Delta_g)$  profile and is shown on Fig. 4-1 between 40 and 90 km. This profile generally has larger densities above 80 km than either of the profiles obtained from other experiments [RM-63, MR-73] but below 70 km, is in good agreement with the model profile of Krueger and Minzner.

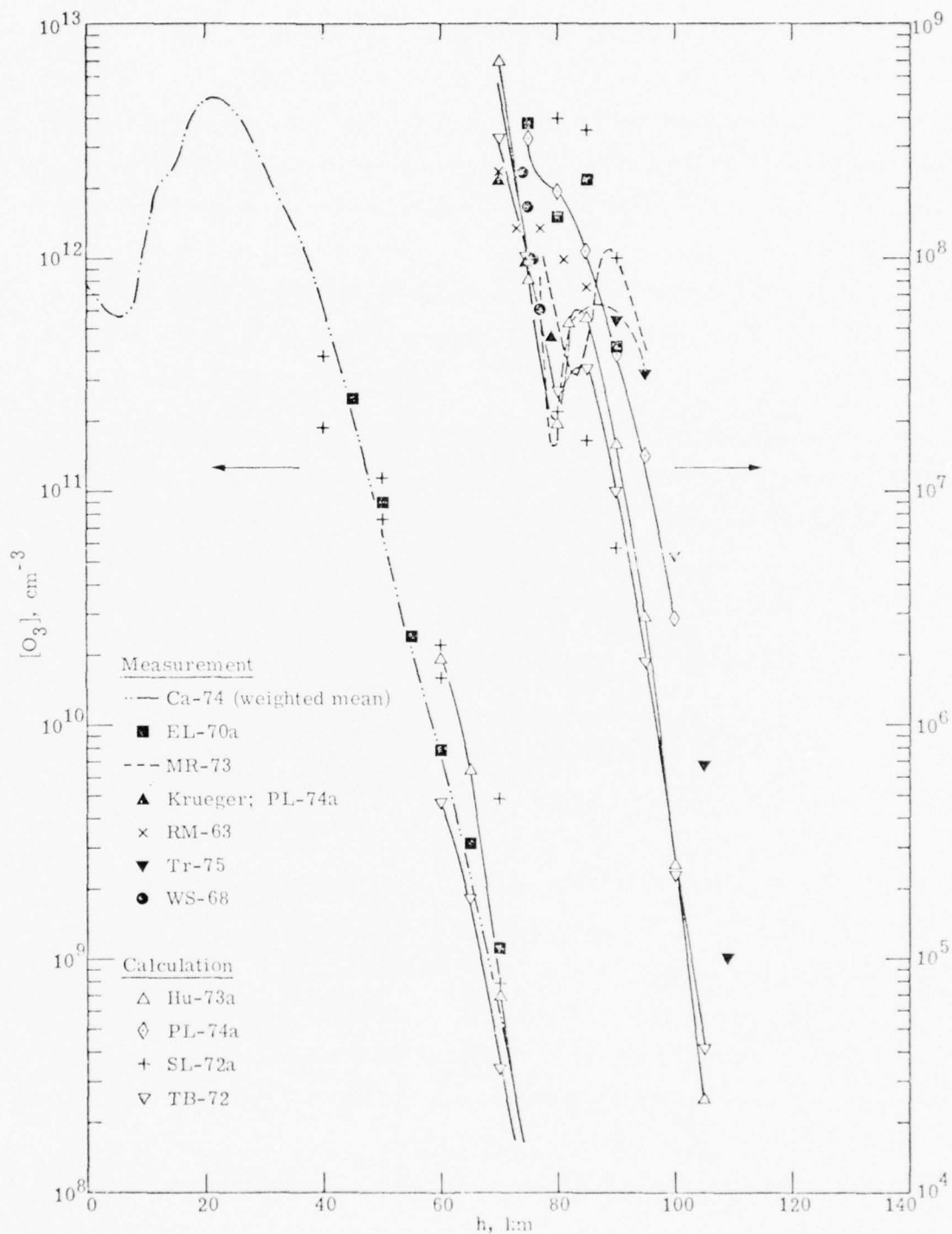


Fig. 4-1. Daytime Ozone Densities Between 0 and 110 km.

#### 4.2.2 Model Calculations

Near 70 km, the calculations of Hunt [Hu-73a] are in close agreement with the ozone profile of Krueger and Minzner [Ca-74] and at 85 km yield a secondary peak in ozone density which is in qualitative agreement with the ozone profile derived from measured  $O_2(^1\Delta_g)$  profiles [EL-70a]. The comparison of these profiles can be made from the data on Fig. 4-1. The ozone profile derived from  $O_2(^1\Delta_g)$  data [EL-70a] for  $32^\circ N$  has larger densities than the calculations of Hunt [Hu-73a]; the latter, however, considers his  $O_3$  densities to be too low above 70 km based on a comparison of model calculations for dawn conditions with satellite measurements [HR-72a]. Other data from Evans and Llewellyn [EL-70a], for a latitude of  $60^\circ N$ , yield profiles in the 75 to 90 km range which exhibit a considerable variation of densities; but the lowest density at 80 km is still twice as large as the computed density of Hunt [Hu-73a].

The calculations of Thomas and Bowman [TB-72] extend from 60 km to 125 km; between 60 and 75 km, these calculations are in good agreement with the model ozone profile [Ca-74]. Above 75 km, the calculations agree moderately well with the calculations of Hunt [Hu-73a], being somewhat lower between 75 and 100 km and slightly higher between 100 and 125 km.

The calculations by Shimazaki and Laird [SL-72a] for  $60^\circ N$  for summer and winter conditions yield  $O_3$  densities greater than the ozone model profile for altitudes  $\leq 70$  km but practically span the other calculations [Hu-73a, TB-72] and observations [WS-68, RM-63, EL-70a, MR-73] at altitudes between 70 and 91 km. The previous calculations of Shimazaki and Laird [SL-70a] for  $0^\circ$  latitude yield significantly smaller densities than those shown on Fig. 4-1.

Park and London [PL-74a] have also calculated ozone profiles up to 100 km; the profile in the altitude range between 75 and 100 km does not qualitatively agree with the measured [EL-70a, MR-73] or calculated [Hu-73a, TB-72] profiles as shown on Fig. 4-1.

#### 4.2.3 Selection of Ozone Profile

For altitudes between 0 and 75 km, the model ozone profile from Cadle [Ca-74] is selected. Between 70 and 80 km, several of the rocket and satellite experiments [RM-63, WS-68, Krueger, 1968 — see PL-74a] are in rough agreement and also roughly agree with an extrapolation of the model ozone profile to about 80 km. The ozone profile derived from measurements of the  $O_2(^1\Delta_g)$  emission [EL-70a] has larger  $O_3$  densities than the other measurements between 75 and 80 km, yet does exhibit the maximum at about 85 km which the comprehensive calculations [Hu-73a, TB-72] predict. (As discussed below — Section 4.3.1 — the nighttime measurements [HR-73, SU-74] also reveal a maximum in ozone density near 85 km.) However, these calculations [Hu-73a, TB-72] predict lower densities at 80 km than the set of observations [RM-63, WS-68, Krueger, 1968 — see PL-74a] at 80 km. As a compromise, the average of the rocket and satellite observations between 75 and 80 km will be used and between 80 and 90 km the profile will be the average of the indirect observations [EL-70a] and the calculations [Hu-73a, TB-72, SL-72a]. Above 90 km, the average of the calculations will be chosen [Hu-73a, TB-72]. The input data and calculated averages are shown on Table 4-1. (The measurements of Miller and Ryder [MR-73] were not included in the selection of the ozone profile as they were unknown to us at the time; by including the average of the ascent and descent measurements, the average ozone density would change by less than 15% between 75 and 90 km and by +33% at 90 km.)

Table 4-1. Calculation of Average Ozone Densities  
Between 75 and 125 km.

h, km	[O <sub>3</sub> ], cm <sup>-3</sup>							⟨[O <sub>3</sub> ⟩, cm <sup>-3</sup>
	RM-63	WS-68	Kr; <sup>§</sup> PL-74a	EL-70a	Hu-73a	TB-72	SL-72a <sup>#</sup>	
75	1.3(8)*	1.7(8)	1.0(8)					1.3(8)
80	1.0(8) <sup>†</sup>		4.4(7) <sup>‡</sup>	1.5(8)	2.65(7)	1.95(7)		6.8(7)
85				2.2(8)	5.6(7)	3.3(7)	1.8(8)	1.2(8)
90				4.0(7)	1.6(7)	1.0(7)	5.2(7)	3.0(7)
95					2.9(6)	1.85(6)		2.4(6)
100					2.5(5)	2.4(5)		2.5(5)
105					2.5(4)	4.2(4)		3.4(4)
110					2.8(3)	4.6(3)		3.7(3)
115					2.9(2)	4.6(2)		3.8(2)
120					3.7(1)	4.6(1)		4.2(1)
125					1.0(1)	4.6(0)		7.3(0)

<sup>§</sup> Work of Krueger reported in reference PL-74a.

\* Average value.

<sup>†</sup> Interpolated value.

<sup>‡</sup> Extrapolated value.

<sup>#</sup> Average of summer and winter values.



The selected data are plotted on Fig. 4-2 and listed in Table 4-2. The secondary layer in the  $O_3$  density centered about 85 km has a strong, seasonal variation [EL-72a], as deduced from twilight measurements of the  $O_2(^1\Delta_g)$  emission; this layer has a maximum ozone density in midwinter and a minimum density in midsummer. The mean annual concentration in a 10-km layer, as deduced from the observed  $O_2(^1\Delta_g)$  emission, is  $8 \times 10^7 \text{ cm}^{-3}$ , whereas the mean concentration of the selected profile shown in Fig. 4-2 in a 10-km layer centered at 85 km is  $7 \times 10^7 \text{ cm}^{-3}$ . Thus the selected profile in this 10-km layer represents a type of mean annual profile. Note, however, that Hayes and Roble [HR-73] found, in the equatorial regions, no apparent seasonal pattern in the ozone profiles between 50 and 100 km for nighttime measurements.

#### 4.2.4 Late Reports on Ozone

Recently [Tr-75] a daytime measurement of the ozone density in the altitude region between 90 and 110 km has been successfully made for the first time by use of a cryogenic, neutral gas, mass spectrometer. Preliminary results are shown on Fig. 4-1; these data are upper limit values and could be smaller by 60% at 90 km but only by 5% at 110 km. Above 100 km, the measured densities are significantly larger than the calculated densities of Hunt [Hu-73a] and Thomas and Bowman [TB-72]. These ozone measurements [Tr-75] are put on an absolute basis by using the CIRA-72 density of argon at 90 km as a normalizing point.

### 4.3 NIGHTTIME DENSITIES

#### 4.3.1 Measurements

The nighttime ozone density only varies significantly from the daytime ozone density at altitudes above about 55 km, according to

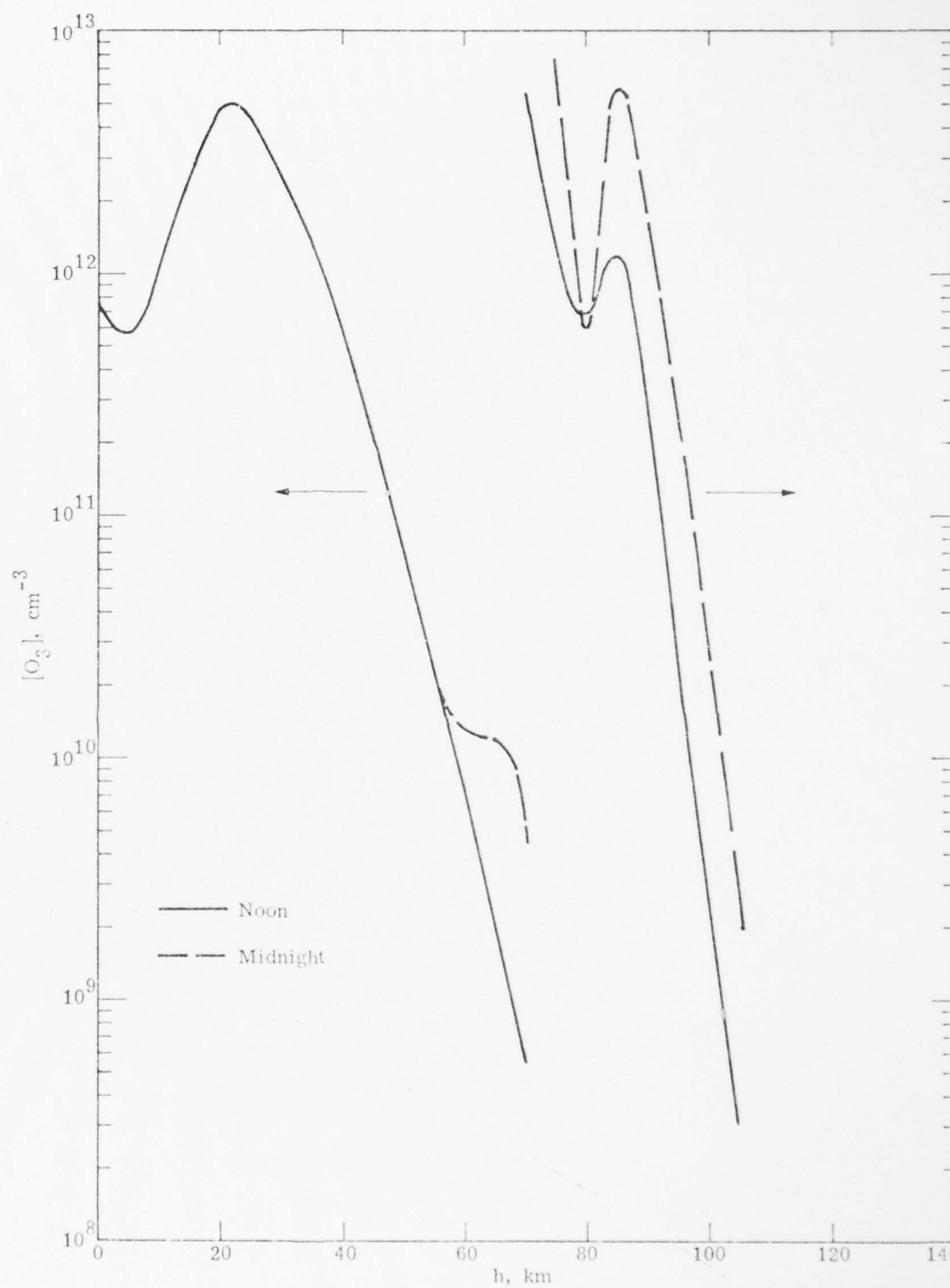


Fig. 4-2. Profile of Ozone Between 0 and 110 km for Noon and Midnight Conditions.

Table 4-2. Profile of Ozone for Noon and Midnight Conditions.

h, km	[O <sub>3</sub> ], cm <sup>-3</sup>		h, km	[O <sub>3</sub> ], cm <sup>-3</sup>	
	Noon	Midnight		Noon	Midnight
0	8.0(11)	8.0(11)	70	5.5(8)	4.5(9)
5	5.7(11)	5.7(11)	75	1.3(8)	7.7(8)
10	1.1(12)	1.1(12)	80	6.8(7)	6.1(7)
15	2.5(12)	2.5(12)	85	1.2(8)	5.8(8)
20	4.8(12)	4.8(12)	90	3.0(7)	1.7(8)
25	4.3(12)	4.3(12)	95	2.4(6)	2.7(7)
30	2.5(12)	2.5(12)	100	2.5(5)	2.7(6)
35	1.4(12)	1.4(12)	105	3.4(4)	2.9(5)
40	6.1(11)	6.1(11)	110	3.7(3)	4.0(4)
45	2.0(11)	2.0(11)	115	3.8(2)	3.5(3)
50	6.7(10)	6.7(10)	120	4.2(1)	1.9(2)
55	2.0(10)	2.0(10)	125	7.3(0)	2.4(1)
60	7.4(9)	1.3(10)	130	-	2.8(0)
65	2.1(9)	1.2(10)			

theoretical expectations [Ca-74] and according to observations [CH-66a, Re-68c, Hi-71a, CH-72]. This is demonstrated on Fig. 4-3 where the ozone profile selected as the daytime reference is drawn as a smooth curve. At altitudes below about 55 km, there is excellent agreement between the nighttime measurements [CH-66a, Re-68c, Hi-71a, CH-72] and the daytime ozone profile with the exception of satellite measurements [HR-73]; above 55 km, the nighttime observations yield larger densities. In the vicinity of 65 km, there is a large spread in the experimental values. The rocket firings [CH-66a, Re-68c, Hi-71a, CH-72], in the latitude range 30-38°N, yielded data up to about 70 km. These experiments used as a radiation source lunar UV radiation [CH-66a, CH-72] and airglow [Re-68c] or employed a chemiluminescent ozone sonde [Hi-71a]. The satellite observations [HR-73], between 50 and 80 km, have ozone densities smaller than the daytime profile and this is in contrast to all other measurements as well as calculations (see below). However, these measurements extend to 100 km and do exhibit the secondary ozone peak at 85 km. Recent nighttime rocket experiments [SU-74] in which emission measurements of ozone at 9.6  $\mu\text{m}$  have been made, indicate a peak ozone density at about 86 km.

#### 4.3.2 Model Calculations

The calculations of Hunt [Hu-73a], Thomas and Bowman [TB-72], Shimazaki and Laird [SL-70a, SL-72a] and Park and London [PL-74a] are shown on Fig. 4-3. Between 55 and 75 km, the calculated nighttime ozone densities exceed the daytime values of the model ozone profile; between 75 and 85 km, the computed densities [Hu-73a, TB-72] are smaller than the daytime profile densities and at altitudes above 85 km, all nighttime calculated ozone densities are larger than the daytime profile densities. The calculations span the latitude range from zero to 60°.

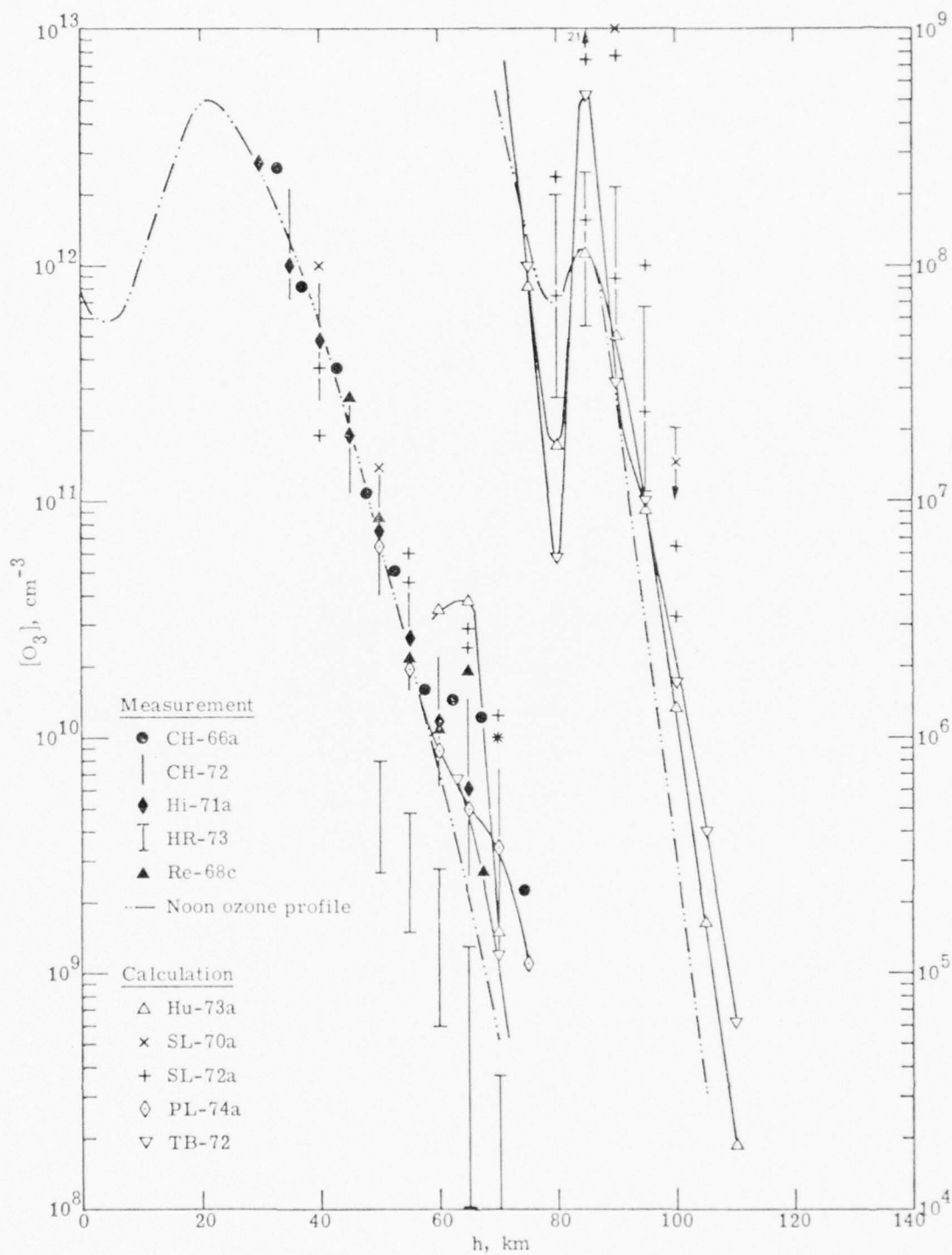


Fig. 4-3. Nighttime Ozone Densities Between 0 and 110 km.

The total ozone content of the atmosphere increases with increasing latitude [Du-74], however this is not generally true for the ozone content at specific altitudes. Between about 30 and 50 km, the ozone density decreases with increasing latitude and between 60 and 80 km this dependence is found for January but the reverse dependence is found for July [PL-74a]. Between 50 and 60 km there is little dependence on the latitude. See Fig. 4-4. The calculations of Shimazaki and Laird [SL-70a, SL-72a] are in qualitative agreement with these trends for altitudes between 40 and 70 km; at higher altitudes an increase in the ozone density with latitude is predicted for summer and winter seasons. The calculations of Hunt [Hu-73a] at  $0^\circ$  in comparison with those of Shimazaki and Laird [SL-72a] at  $60^\circ$ , results in a prediction of an increase in ozone density with latitude.

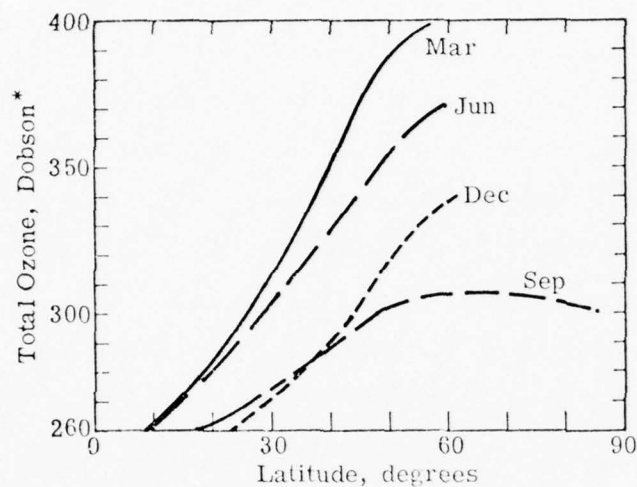
The diurnal variation of ozone has been calculated [Hu-73a, TB-72, PL-74a]; Park and London [PL-74a] point out that diurnal asymmetry results from inclusion of hydrogenous compounds in the chemical system.

#### 4.3.3 Selection of Ozone Profile

For altitudes of 55 km and smaller, the nighttime ozone profile will be taken to be identical to the daytime profile. This is supported by the excellent agreement between the selected daytime ozone profile and the nighttime observations. Between 55 and 75 km, reliance will be placed on the observations and the average of the observed values will be used as the selected ozone nighttime profile (with the exception of satellite observations [HR-73] which are significantly different from the total sets of calculations and remaining observations). At and above 75 km, the average of the recent calculations [TB-72, SL-72a, Hu-73a, PL-74a] will be used. In the case of the calculations of Shimazaki and

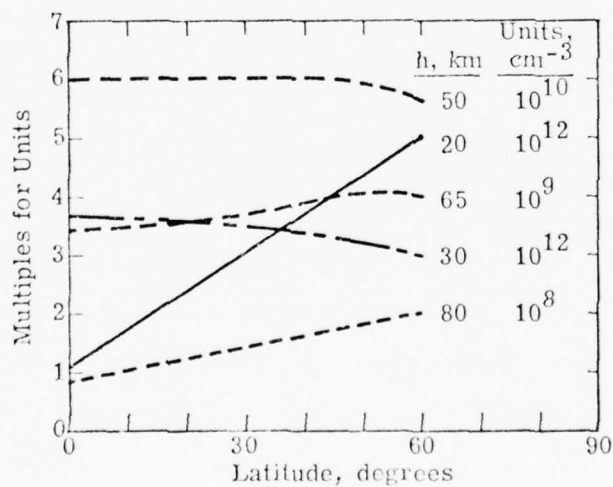


A. Dependence of Total Atmospheric Ozone on Latitude for Various Seasons - Du-74



\*Dobson  $\equiv 10^{-3}$  cm ozone, at normal temperature and pressure.

B. Dependence of Atmospheric Ozone Density on Latitude for Various Altitudes and Seasons - PL-74a



Curves are for July; curves have similar trends for Jan except curves at 65 and 80 km which have opposite trends for Jan.

Fig. 4-4. Dependence of Atmospheric Ozone on Latitude and Season.

Laird [SL-72a] the average of the summer and winter calculations is used; this has an effect of converting the calculations [SL-72a] to a lower, effective latitude than the  $60^{\circ}\text{N}$  latitude of the calculations since the ozone density in summer (upper point on Fig. 4-3 for SL-72a) will be lower at midlatitudes than at  $60^{\circ}\text{N}$  [PL-74a] and the ozone density in winter (lower point on Fig. 4-3 for SL-72a) will be higher at midlatitudes than at  $60^{\circ}\text{N}$  [PL-74a], at least between 60 and 80 km. Furthermore, at midlatitudes (say  $45^{\circ}\text{N}$ ) the seasonal variation in total ozone density will peak near summer and show a minimum near winter [Du-74], so that an average is appropriate for a mean, midlatitude ozone model.

The average values are calculated from data in Table 4-3 for  $h \geq 60$  km. The selected nighttime profile is shown in Fig. 4-2.

Table 4-3. Average Ozone Densities Above 60 km for Nighttime Conditions.

h, km	[O <sub>3</sub> ], cm <sup>-3</sup>								<[O <sub>3</sub> ]> cm <sup>-3</sup>
	CH-66a	Re-68c	CH-72*	Hi-71a	SL-72a	PL-74a	Hu-73a	TB-72	
60	1.5(10)	1.1(10)	1.5(10)	1.2(10)					1.3(10)
65	1.35(10)	1.9(10)	8.6(9)	6.3(9) <sup>†</sup>					1.2(10)
70	4.6(9)	-	4.4(9)	-					4.5(9)
75					1.8(9)	1.1(9)	8.2(7)	1.0(8)	7.7(8)
80					1.6(8)	-	1.8(7)	5.9(6)	6.1(7)
85					1.1(9)	-	1.15(8)	5.3(8)	5.8(8)
90					4.4(8)	-	5.0(7)	3.2(7)	1.7(8)
95					6.2(7)	-	9.3(6)	1.0(7)	2.7(7)
100					4.9(6)	-	1.35(6)	1.75(6)	2.7(6)
105					-	-	1.65(5)	4.1(5)	2.9(5)
110					-	-	1.85(4)	6.3(4)	4.0(4)
115					-	-	1.7(3)	5.3(3)	3.5(3)
120					-	-	1.9(2)	1.9(2)	1.9(2)
125					-	-	2.9(1)	1.9(1)	2.4(1)
130					-	-	3.7(0)	1.9(0)	2.8(0)

\*Average value from data of CH-72.

<sup>†</sup>This value was actually 8.2(9); however the average, to two significant digits, is unaffected by correcting this error.

## 5. DENSITY PROFILE OF NITRIC OXIDE

### 5.1 INTRODUCTION

A midlatitude profile for nitric oxide is selected in the altitude range from ground level to 240 km. While measurements of nitric oxide have been made in a large fraction of this altitude range, significant discrepancies and uncertainties remain among the data. Similarly, agreement among calculated nitric oxide profiles is lacking. However, in at least one instance of apparent discrepancy between experimental results, the difference in season and solar activity at the time of the measurements has been shown, by model calculations [OJ-74], to be important in accounting for the discrepancy. Discussions of the effect of solar activity and season on nitric oxide density are presented in Sections 5.2.3 and 5.4.2. Additional measurements and model calculations are necessary for establishing reliable nitric oxide atmospheric densities.

### 5.2 DAYTIME NITRIC OXIDE DENSITIES ABOVE 120 KM

#### 5.2.1 Measurements

There have been two measurements at altitudes above 120 km from which daytime NO densities are obtained: a rocket experiment at 32°N [FT-74] in which the twilight emission from the  $\gamma$ - and  $\delta$ -bands of nitric oxide were observed and a satellite experiment [Kr-70a] in which the  $\gamma$ - and  $\delta$ -bands were also measured. Near 215 km where NO densities have been derived from the two measurements, there is about an order of magnitude scatter in the densities as shown on Fig. 5-1. This scatter is discussed in Section 5.2.3 below; the nighttime measurements shown on Fig. 5-1 are discussed in Section 5.5 below.

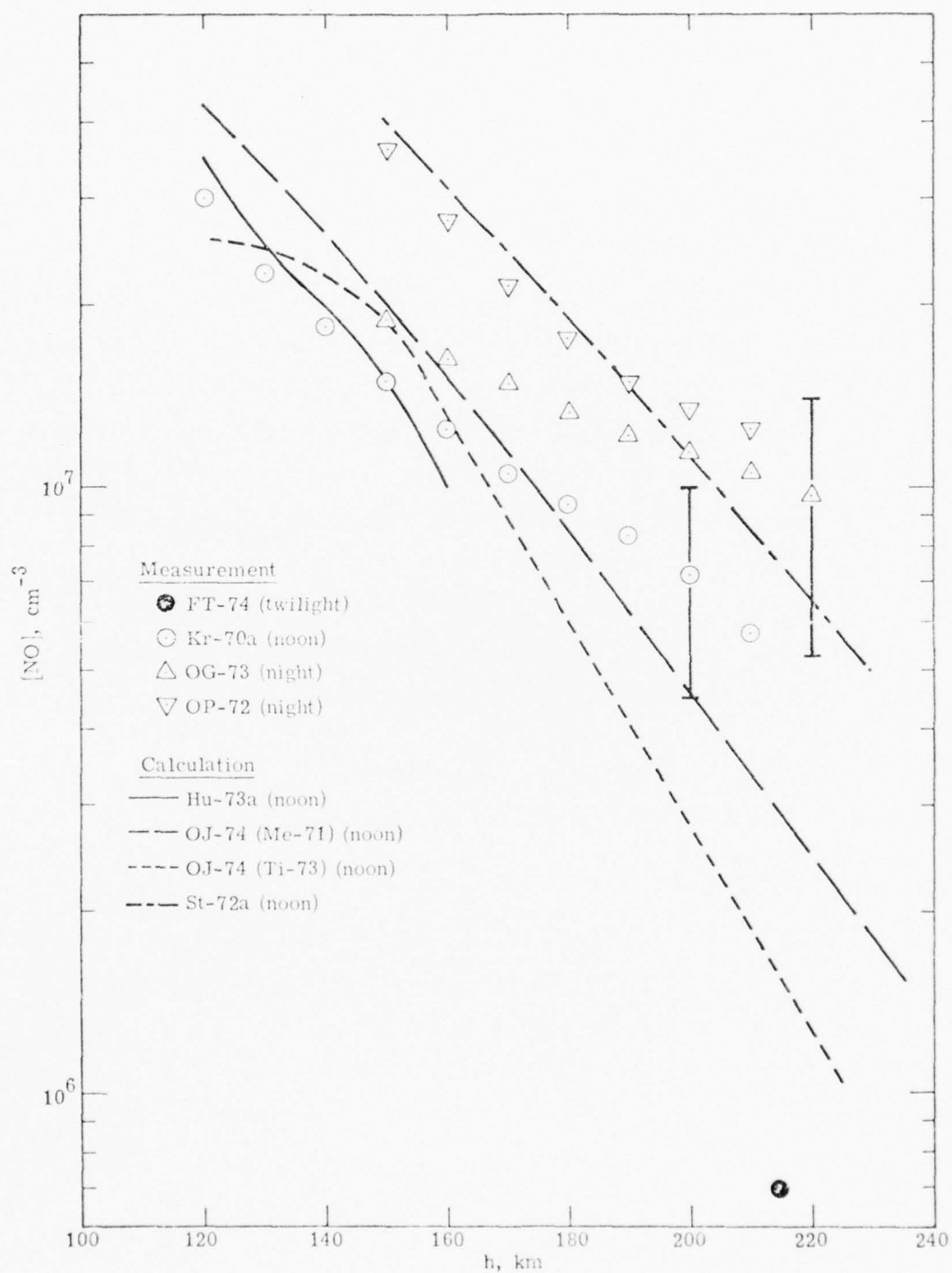


Fig. 5-1. Nitric Oxide Densities Above 120 km.

### 5.2.2 Model Calculations

A number of model calculations have been made [St-71, SH-70, St-72a, Hu-73a, SL-70a, SL-72a, Ru-73a, Ni-70, OJ-74] for altitudes above 120 km. In the calculations of Strobel [St-72a] shown on Fig. 5-1, boundary conditions were carefully treated but a constant eddy diffusion coefficient [St-71] was used; the latter is not in accord with observational data. The calculation of Hunt [Hu-73a] employed an eddy diffusion coefficient which varied with altitude; here the boundary conditions at the upper boundary were different from those of Strobel. Hunt [Hu-73a] used a diffusive equilibrium condition where Strobel [St-72a] used a flux condition.

The calculations of Rusch [Ru-73a] yielded larger densities than observed or calculated by others and the calculations of Shimazaki and Laird [SL-70a, SL-72a] are significantly smaller since ionic reactions were not included. The calculations of Nicolet [Ni-70] do not include transport effects. These calculations [Ni-70, Ru-73a, SL-70a, SL-72a] were omitted from the comparisons of Fig. 5-1.

Recently, calculations [OJ-74] have been made, based on a model similar to previous models [SM-70, St-71, St-71d] but with an improved description of chemical processes for higher altitudes and an altitude-dependent, eddy diffusion coefficient. These calculations were specifically made for the conditions on the days of the rocket flights of Meira [Me-71] and Tisone [Ti-73]; the noon profiles for altitudes above 100 km are shown on Fig. 5-1. The noon profiles of Oran et al. [OJ-74] are in agreement with the calculations of Hunt [Hu-73a] for altitudes up to 160 km. At higher altitudes, a significant difference in nitric oxide density for the conditions of the two flights [Me-71, Ti-73] is predicted by Oran et al. [OJ-74]; this difference is further considered in Section 5.2.3.



### 5.2.3 Further Analysis of Measurements and Calculations

A large disparity among measurements at 215 km has been noted. Also, mention has been made of recent calculations [OJ-74] in which the influences of solar activity and seasonal variations on the nitric oxide density are considered. These influences will be further examined here before attempting to select a nitric oxide profile.

In the vicinity of the altitude of 215 km, there are two daytime measurements from which nitric oxide densities have been derived [Kr-70a, FT-74]. In addition, recent calculations [OJ-74], made specifically for the conditions of two other measurements at lower altitudes [Me-71, Ti-73], have been extended to 215 km. By comparing the measured and calculated nitric oxide densities with the 10.7 cm solar flux for the days or measurement period of the four related experiments [FT-74, Kr-70a, Me-71, Ti-73], a correlation is found as shown by the data of Table 5-1 and their graphical representation; note circles on Fig. 5-2. The curve on Fig. 5-2 will be discussed later. The datum of Feldman and Takacs [FT-74] is reported as an upper limit and is shown as such on Fig. 5-2. Note that the calculations of Oran et al. [OJ-74] are included in Fig. 5-2 on the basis that they are assumed to predict reasonably well the nitric oxide densities at high altitudes and not on the basis that the solar intensities used in the calculation [OJ-74] are corrected, in some manner, to correspond to values of the solar flux associated with the calculated nitric oxide densities shown on Fig. 5-2. The text [OJ-74] is not explicit on this point but apparently no such correction was made. The rationale for the relation between nitric oxide density and the solar flux is as follows. According to Jacchia [Ja-71c], the exospheric temperature, and consequently the

Table 5-1. Nitric Oxide Densities at 215 km and the Decimetric Solar Flux

Day or Period	Solar 10.7 cm Flux, $F_{10.7}$ $10^{-22} \text{ W m}^{-2} \text{ Hz}^{-1}$	Ref. <sup>†</sup>	[NO] $\text{cm}^{-3}$	Ref.
Jan 4, 1974	75	a	$\leq 7.0(5)$	FT-74
June 1968	142	b	5.0(6)	Kr-70a
Jan 31, 1969	130	c	} 2.9(6)	Me-71
Feb 6, 1969	142.5	d		Me-71
May 26, 1971	91	e	1.5(6)	Ti-73

- <sup>†</sup> a. "Solar-Geophysical Data," 354, Part I, 7, Feb. 1974.  
b. Ibid, IER-FB-287, 7, July 1968.  
c. Ibid, IER-FB-294, 7, Feb. 1969.  
d. Ibid, IER-FB-295, 7, Mar. 1969.  
e. Ibid, 322, Part I, 7, June 1971, U. S. Department of Commerce (Boulder, Colorado 80302).

molecular oxygen density at high altitudes, is proportional to the 10.7 cm solar flux. But the nitric oxide density is also proportional to the molecular oxygen density [OJ-74]; therefore the nitric oxide density is proportional to the decimetric solar flux. The basis of the dependence of the nitric oxide density on the molecular oxygen density is the following reaction couple:



An increase in molecular oxygen increases the formation rate of NO via reaction 1 and reduces the loss rate of NO in reaction b as a result of the increased loss rate of  $\text{N}(^4\text{S})$  in reaction a.

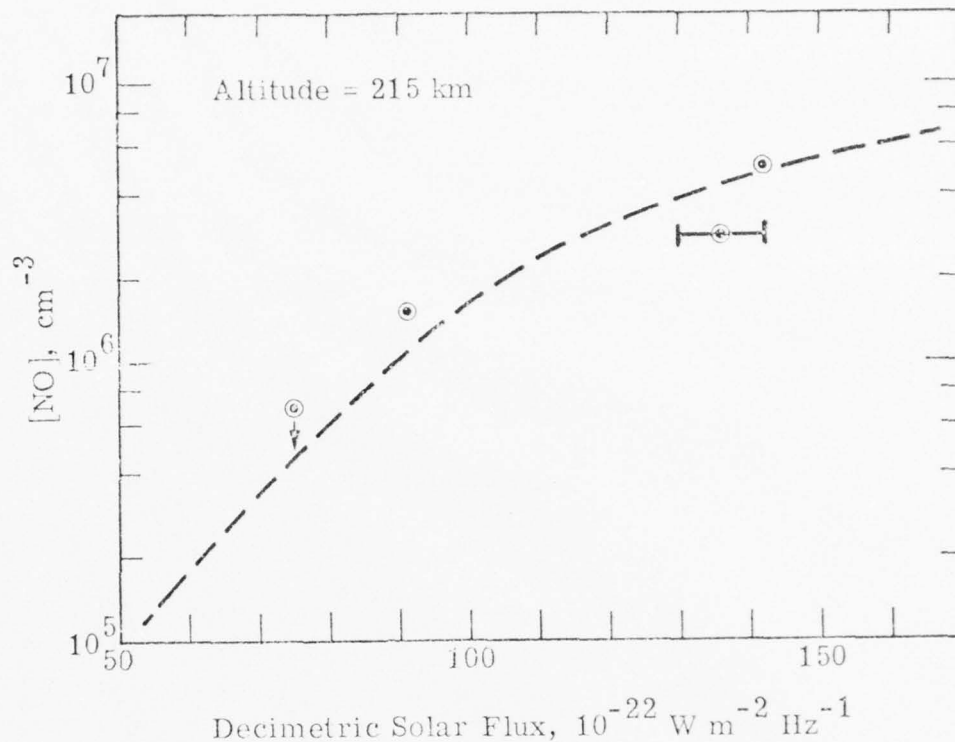


Fig. 5-2. Nitric Oxide Densities vs Decimetric Solar Flux.

At lower altitudes, between 120 and 160 km, the available measurements [OG-73, Kr-70a] and calculations [Hu-73a, OJ-74] are in much better agreement than at 215 km so that the strong dependence of the nitric oxide density on the 10.7 cm solar flux is not expected at these lower altitudes. This is consistent with the fact that the variation in the molecular oxygen density with variation in the exospheric temperature (and thus solar flux) is smaller, by factors of 220 to 15, in the altitude range between 120 and 160 km than at 220 km, according to the Jacchia atmosphere [Ja-71c]. Consequently, at 120 km, the assumption will be made that the nitric oxide density is independent of the decimetric solar flux (see, however, Section 5.4.2 below).

Another possible influence on the oxygen density, and hence on the nitric oxide density, is seasonal. Roble and Norton [RN-72a] find a seasonal variation in the oxygen densities for altitudes in the range 100 to 120 km. The measurements are from solar occultations performed over a nine month period and show a minimum molecular oxygen density in winter and a maximum density in the summer about two to three times larger than the winter minimum. Previous collations of data [Ch-70b] have shown no seasonal variation at midlatitudes. At altitudes above 120 km, apparently no seasonal variation has been established.

#### 5.2.4 Selection of Nitric Oxide Profile

Since the variation of nitric oxide density with solar activity appears to be strong and to be useful in accounting for the disparity in measured and calculated densities, the selected profile will include the dependence of density on solar activity. Any possible seasonal variation of nitric oxide density will be neglected. At 215 km, the relationship between density and solar activity will be roughly approximated by use of the following equation:

$$\ln[\text{NO}]_{215} = 10.22 + \frac{6.08 F_{10.7}^3}{5 \times 10^5 + F_{10.7}^3} \quad (1)$$

where  $F_{10.7}$  is the solar activity in units of  $10^{-22} \text{ W m}^{-2} \text{ Hz}^{-1}$ . The dashed curve on Fig. 5-2 is based on Eq. (1). At 120 km, the nitric oxide density will be fixed at  $3 \times 10^7 \text{ cm}^{-3}$  based on observation [Kr-70a]. To establish the nitric oxide profile at and above 120 km, the slopes ( $\equiv -d \ln[\text{NO}]/dh$ ) will be determined by the relations:

$$S = S^\circ \quad h = 120 \text{ km} \quad (2)$$

$$S_v = S^\circ - \left( \frac{h - 120}{h_r - 120} \right) (S^\circ - S_c) \quad 120 \text{ km} < h \leq h_r \quad (3)$$

$$S_c = - \frac{\ln \{ [NO]_{215} / [NO]_r \}}{215 - h_r} \quad h_r \leq h \quad (4)$$

where  $S^\circ$  is the slope at 120 km,  $S_v$  the variable slope between 120 and  $h_r$  km, and  $S_c$  the constant slope at and above  $h_r$  km. By using the definition of slope and Eq. (3), the nitric oxide density between 120 and  $h_r$  km is found to be

$$\ln [NO] = \ln [NO]_{120} - (h - 120)S^\circ + \frac{1}{2} \frac{(h - 120)^2}{(h_r - 120)} (S^\circ - S_c) \quad (5)$$

and at  $h_r$  km, the density is thus

$$\ln [NO]_r = \ln [NO]_{120} - \frac{(h_r - 120)}{2} (S^\circ + S_c) \quad (6)$$

At altitudes above  $h_r$

$$\ln [NO] = \ln [NO]_r - S_c (h - h_r) \quad (7)$$

By using Eqs. (4) and (6), the slope,  $S_c$ , becomes

$$S_c = - \left\{ \frac{2 \ln \{ [NO]_{215} / [NO]_{120} \} + (h_r - 120)S^\circ}{310 - h_r} \right\} \quad (8)$$

Profiles for nitric oxide at altitudes above 120 km can be calculated by using Eqs. (5)-(8) together with the selected nitric oxide density at 120 km, the nitric oxide density at 215 km as calculated with Eq. (1), and the slope  $S^\circ$  at 120 km as determined from the nitric oxide profile

for 120 km and lower altitudes. (See Section 5.3.3.) The profiles of nitric oxide above 120 km are illustrated in Fig. 5-3 where  $h_r = 125$  km.

### 5.3 DAYTIME NITRIC OXIDE DENSITIES BELOW 120 KM

#### 5.3.1 Measurements

A number of observations have been made [Ba-66d, Pe-69a, Me-71, Ru-73a, Ti-73] at altitudes above 60 km by measurement of the radiation from the NO  $\gamma$ -bands. For all but one investigation [Pe-69a], the NO densities lie between  $10^7$  and  $10^8$  cm<sup>-3</sup>; the results of Pearce [Pe-69a] as can be seen on Fig. 5-4 are more than an order of magnitude larger than the other observations. The profiles deduced by Pearce [Pe-69a] have been criticized by Meira [Me-71] on the basis of inadequate correction for Rayleigh scattering and ozone absorption contributions.

From the measurements of Rusch [Ru-73a] only upper and lower limits are obtained; these are shown on Fig. 5-4. The measurements of Tisone [Ti-73] and Barth [Ba-66d] are in qualitative agreement with discrepancies of less than a factor of two over a large fraction of the common altitude range. The measurements of Meira [Me-71] are distinctly different from either those of Tisone [Ti-73] or Barth [Ba-66d] by the pronounced minimum at about 85 km. Between the measurements of Tisone [Ti-73] and Meira [Me-71] there is a difference in time of day, season and latitude: the measurements of Tisone [Ti-73] were obtained about 0500 LT in May at 22°N whereas those of Meira [Me-71] were obtained about 1400 LT, in January and February at 38°N.

There are four sets of measurements [AF-73, RS-73d, TF-73, PB-74] in the altitude range of 15 to 40 km; these are plotted on Fig. 5-4. The apparently most reliable measurement is that of Patel et al. [PB-74] in which the measured species, NO, is unequivocally



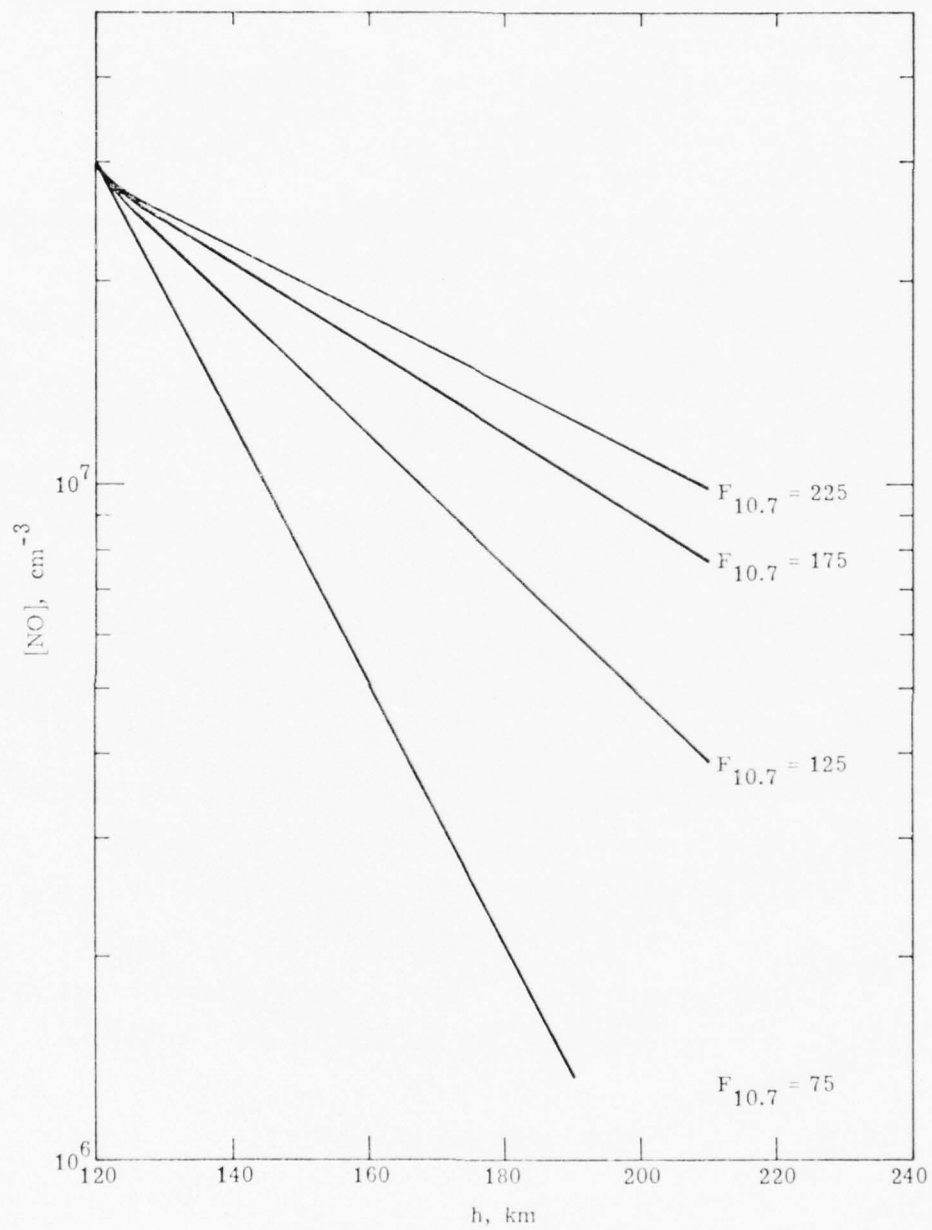


Fig. 5-3. Profiles of Nitric Oxide Above 120 km as a Function of Solar Activity.

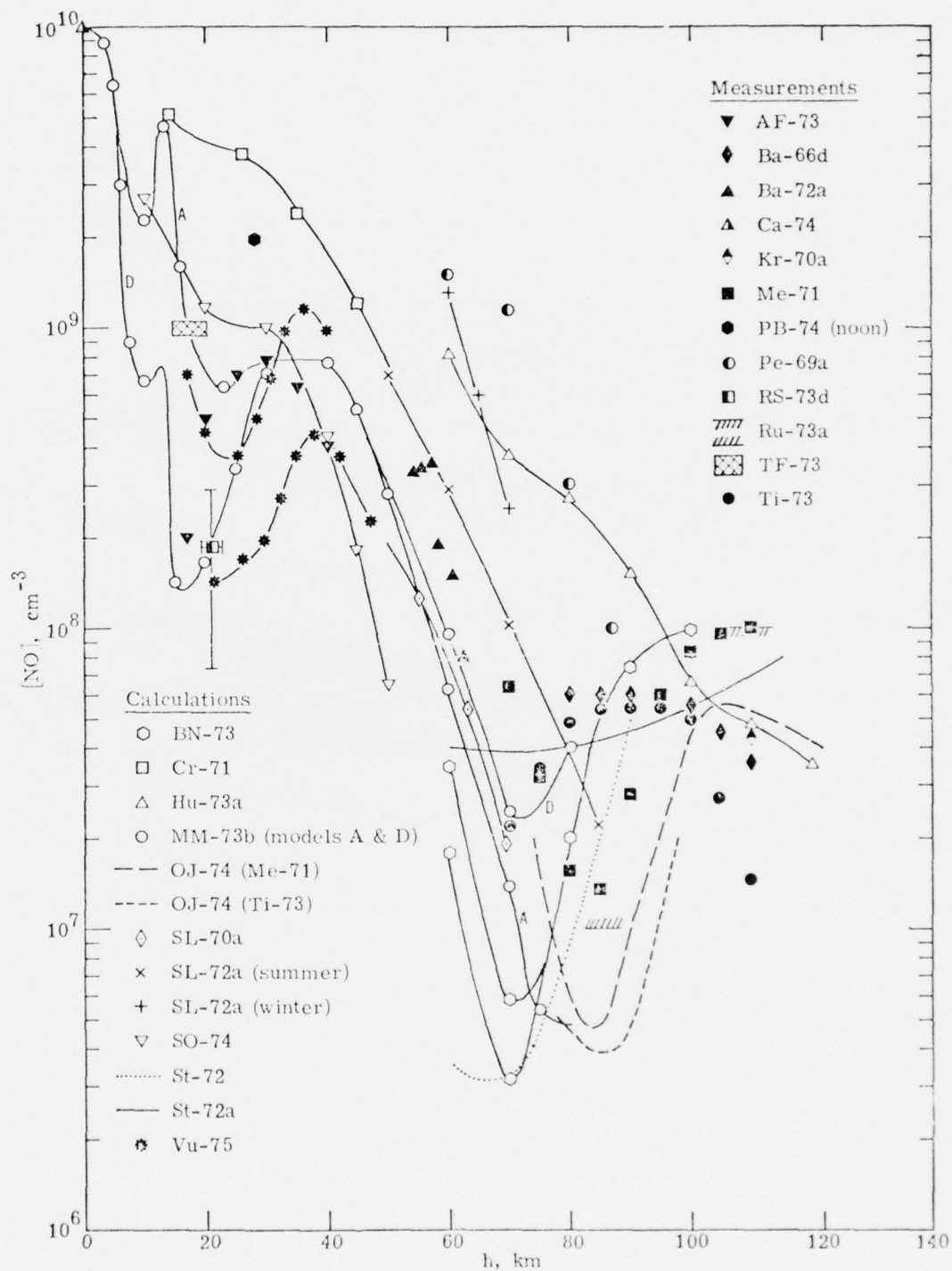


Fig. 5-4. Nitric Oxide Densities Below 120 km.

identified by use of a spin-flip Raman laser. This measurement clearly demonstrates the variation of nitric oxide density between sunrise and noon at 28 km. The most extensive set of measurements are those of Ackerman et al. [AF-73] based on absorption by NO in the 5.2  $\mu\text{m}$  band using the setting sun as the light source. As the solar zenith angle increases above  $90^\circ$ , the path between the sun and the detector, at 40 km, passed through lower and lower altitudes. The nitric oxide densities were inferred by analysis of the extent of absorption for the changing optical paths. The measurements of Ridley et al. [RS-73d] depended on the reaction of ambient nitric oxide with ozone in the detector to produce the chemiluminescence which was measured. Calibration was provided by an on-board source of nitric oxide. These were midday measurements at  $32^\circ\text{N}$  latitude in March at altitudes in the range of 17.4 to 22.9 km. These results are an order of magnitude smaller than the midday results of Patel et al. [PB-74] at 28 km in the same latitude region in October of the same year (1973). Measurements by Toth et al. [TF-73] provide an upper limit in the altitude range between 15 and 20 km. A ground-level value of the nitric oxide density, recommended by Cadle [Ca-74], is plotted on Fig. 5-4.

### 5.3.2 Model Calculations

The model calculations of nitric oxide density in the lower range of altitudes are difficult to make because of uncertainties in chemical and transport input data. As in the case of atomic oxygen, a thorough comparison of the various models was not made for this review. Several of the model calculation results are plotted on Fig. 5-4. The most extensive model calculations are those of McConnell and McElroy [MM-73b] and Brasseur and Nicolet [BN-73]. The latter investigators have carried out a parametric study; the results which are shown on Fig. 5-4

are for calculations using the upper values of the eddy diffusion coefficients they considered and the variations in these results below 75 km correspond to nitrogen atom production rates of 0 (lower curve) and 10 (upper curve) atoms/(cm<sup>3</sup> sec). Brasseur and Nicolet [BN-73] stress the sensitivity of nitric oxide densities to values of the eddy diffusion coefficient. For a critique of eddy diffusion coefficient values, see Hunten and Strobel [HS-74a]. For the calculations of McConnell and McElroy [MM-73b] two models, A and D, are shown on Fig. 5-4. Model A is their favored model; model D differs only by use of a lower quantum yield for the photolysis of HNO<sub>3</sub>. The value of the quantum yield is presently in doubt but is clearly important for the calculation of NO densities, particularly in the altitude regions between 10 and 30 km. By comparison with model A, model D fits the observational data somewhat better. The calculations of Hunt [Hu-73a] and Crutzen [Cr-71] appear to generally overestimate the NO densities. The calculations of Shimazaki and Laird [SL-70a, SL-72, SL-72a] at 0° and 60°N latitude, bound the midlatitudes of interest in the present analysis. The calculations of Shimazaki and Ogawa [SO-74] for altitudes below 50 km yield densities which are generally not in accord with observations and differ by factors up to three from the calculations of McConnell and McElroy [MM-73b]. The earlier calculations of Strobel [St-72, St-72a] are shown on Fig. 5-4; more recent calculations using an improved version of Strobel's calculations [OJ-74] are shown for the conditions of the observations of Meira [Me-71] and Tisone [Ti-73]. (The curves from these calculations [OJ-74] as drawn on Fig. 5-4 are accurate only at selected altitudes since they were deduced from diurnal nitric oxide contours given [OJ-74] only for a few values of the nitric oxide density.) There is qualitative agreement of the density profiles only with the data from Meira [Me-71]. In the altitude range between 75 and 100 km, the calculated values are smaller than any of the observed values of nitric oxide density.

### 5.3.3 Selection of Nitric Oxide Profile

In selecting the *nitric oxide* daytime profile below 120 km, reliance has been placed exclusively on observations. Seasonal and latitudinal variations are not taken into account explicitly although these variations may be contributing to the data used. In the region below about 40 km, nitric oxide is no longer the principal odd nitrogen species; in the region below 20 km,  $\text{NO}_2$  and  $\text{HNO}_3$  have generally greater densities than nitric oxide. Use of the selected profile in calculations which ignore species such as  $\text{NO}_2$  and  $\text{HNO}_3$  will have little meaning at these altitudes.

In the 70-115 km interval, the average of the observations of Meira [Me-71], Barth [Ba-66d] and Tisone [Ti-73] were used. The observations of Pearce [Pe-69a] were excluded by virtue of the large discrepancy between these observations and others for this altitude region as well as between 60 and 70 km. These averages are given in Table 5-2. At 115 km, the density was obtained by interpolation using the values at 110 km and the value at 120 km (see Section 5.2.4).

For the altitude range between 28 km and 60 km, the datum of Patel et al. [PB-74] was selected as the absolute NO density at 28 km; the data of Ackerman et al. [AF-73] were normalized at 28 km to the datum of Patel et al. [PB-74]. These data together with the data of Hale [Ba-72a] determine the nitric oxide profile between 28 and 60 km. See Table 5-2.

Between 60 and 90 km, a smooth curve was drawn using the previously selected values at 60, 75 and 90 km to determine the locus of the curve.

Table 5-2. Selection of Values of Nitric Oxide Densities Below 120 km.

h, km	[NO], cm <sup>-3</sup>								⟨NO⟩, cm <sup>-3</sup>
	Me-71	Ba-66d	Ti-73	Kr-70a	⟨[NO]⟩	Text <sup>†</sup>	Ba-72a <sup>‡</sup>	RS-73d	
115						3.60(7)			
110	8.1(7)	3.6(7)	1.5(7)	4.35(7)	4.38(7)				
105	9.6(7)	4.6(7)	2.75(7)		5.65(7)				
100	8.2(7)	5.5(7)	5.1(7)		6.27(7)				
95	6.0(7)	6.0(7)	5.5(7)		5.83(7)				
90	2.8(7)	6.0(7)	5.5(7)		4.77(7)				
85	1.35(7)	6.0(7)	5.5(7)		4.28(7)				
80	1.55(7)	6.0(7)	4.9(7)		4.15(7)				
75	3.25(7)	-	3.4(7)		3.33(7)				
70	6.4(7)		2.2(7)		4.3(7)				
65						5.5(7)			
60							1.4(8)		
55							3.3(8)		
50						5.1(8)			
45						8.5(8)			
40						1.25(9)			
35						1.75(9)			
30						2.05(9)			
25						1.75(9)			
20						1.23(9)		1.75(8)	7.0(8)
15						5.8(8)			
10						1.3(9)			
5						3.4(9)			
0						1.0(10)			

<sup>†</sup> See text.

<sup>‡</sup> Hale's results as reported in Ba-72a.



At 25 km, the nitric oxide density was selected from the adjusted data of Ackerman et al. [AF-73]; at 20 km, the average of the datum from the adjusted curve of Ackerman et al. [AF-73] and of that from Ridley et al. [RS-73d] was selected; below 20 km, a smooth curve was drawn using the selected, 20 km datum, a datum for 16.5 km from the adjusted curve of Ackerman et al. [AF-73] and the recommended [Ca-74] nitric oxide density at ground level. Below 20 km, where only calculations are available [MM-73b, Le-72a, Le-73], peaks in the calculated nitric oxide profile [MM-73b] have been ignored.

The nitric oxide profile data are collated in Table 5-3 and shown on Fig. 5-5 for altitudes below 120 km.

#### 5.4 ADDITIONAL DAYTIME NITRIC OXIDE DATA

##### 5.4.1 Indirect Determinations of Densities

Nitric oxide densities have been deduced "indirectly" [Da-72e, KB-74c, NP-72a, MR-74b, Ol-74a, ZS-74] by use of measurements on electron and ion densities and Lyman-alpha radiation. Most of these deductions are summarized by Mitra and Rowe [MR-74b]; their summary demonstrates that between 65 and 100 km, the deduced densities of nitric oxide have values between  $10^7$  and  $10^8 \text{ cm}^{-3}$  with but few exceptions. This summary of deduced, nitric oxide densities provides [MR-74b] constraints on the nitric oxide density on the basis of electron densities for ambient conditions, for conditions resulting from solar activity reversal, for flare conditions and from ion composition measurements. Not included in this summary are nitric oxide densities derived from rocket experiment data [KB-74c, ZS-74] for measuring ion composition and Lyman-alpha intensities and from data on charged particle density variations measured during an eclipse [Ol-74a]. For the experiments of Zalpuri and Somayajulu [ZS-74] between 85 and 90 km,

Table 5-3. Nitric Oxide Profile for Noon and Midnight Conditions.

h, km	[NO], cm <sup>-3</sup>		h, km	[NO], cm <sup>-3</sup>	
	Noon	Midnight		Noon	Midnight
0	1.0(10)	1.0(0)	60	1.4(8)	1.0(6)
5	3.4(9)	↓	65	5.5(7)	8.3(6)
10	1.3(9)		70	3.7(7)	1.65(7)
15	5.8(8)		75	3.3(7)	2.5(7)
20	7.0(8)		80	3.5(7)	3.3(7)
25	1.75(9)		85	4.0(7)	4.0(7)
30	2.1(9)		90	4.8(7)	4.8(7)
35	1.75(9)		95	5.8(7)	5.8(7)
40	1.25(9)		100	6.3(7)	6.3(7)
45	8.5(8)		105	5.7(7)	+
50	5.1(8)		110	4.4(7)	+
55	3.0(8)	1.0(4)	115	3.6(7)	+
			120	3.0(7)	+

#### Noon Conditions

125 km  $\geq$  h > 120 km

$$\ln[\text{NO}]_{\text{noon}} = 17.2167 - (h - 120)S^0 + \frac{(h - 120)^2}{10} (S^0 - S_c)$$

h > 125 km

$$\ln[\text{NO}]_{\text{noon}} = 17.2167 - 2.5(S^0 + S_c) - (h - 125)S_c$$

#### Midnight Conditions

<sup>+</sup> h  $\geq$  105 km

$$[\text{NO}]_{\text{midnight}} = [\text{NO}]_{\text{noon}} \frac{\left( \frac{(h - 100)^2}{10} + 7200 \right)}{\left( \frac{(h - 100)^2}{10} + 7200 \right)}$$

where

$$S^0 = - (d \ln[\text{NO}]/dh)_{h=120 \text{ km}}$$

$$S_c = 0.07564 - 0.02703S^0 - 0.06573 F_{10.7}^3 / (5.0 \times 10^5 + F_{10.7}^3)$$

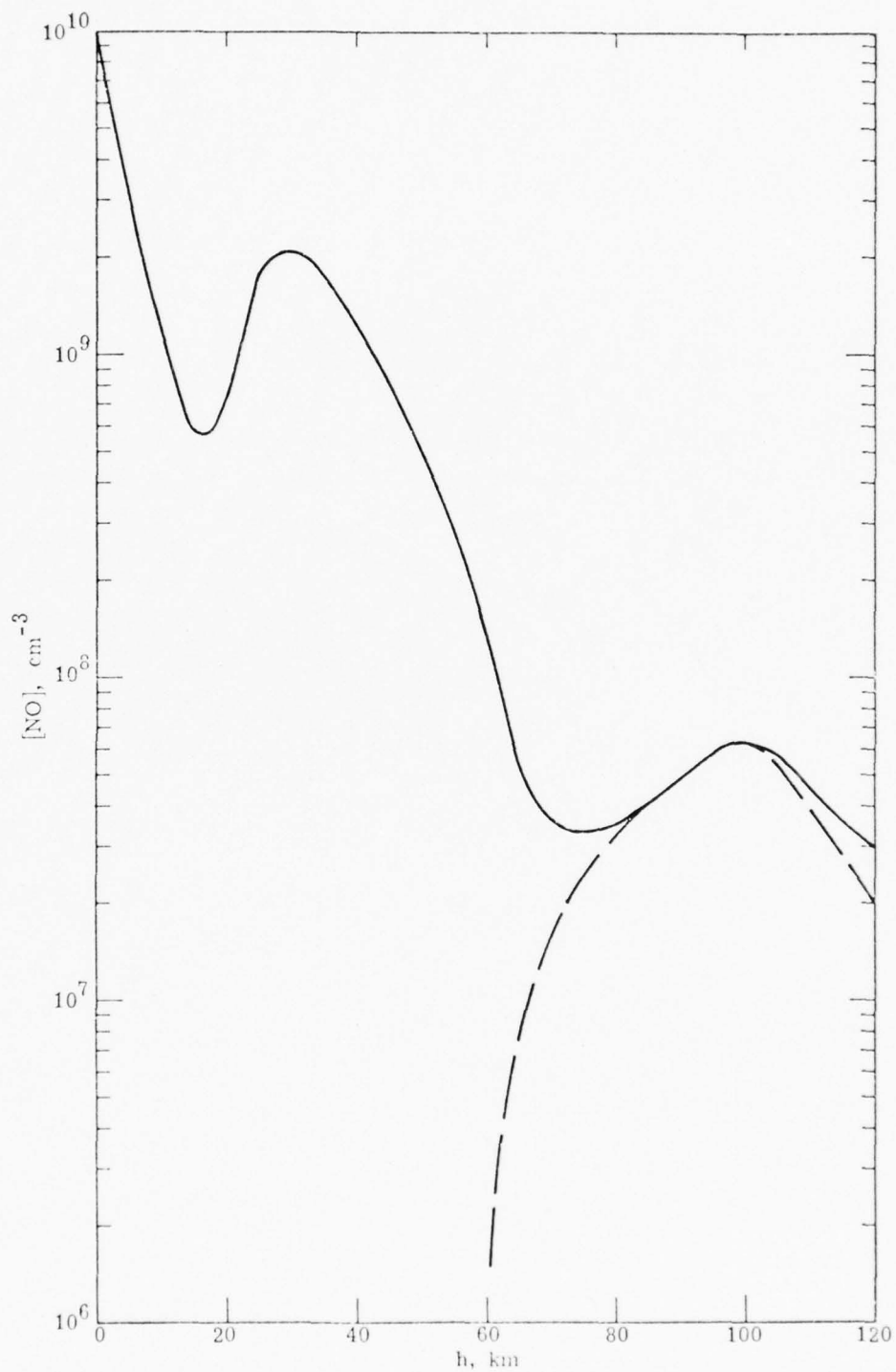


Fig. 5-5. Nitric Oxide Profile Below 120 km for Noon and Midnight Conditions.

the derived densities are in the range  $(1-4) \times 10^7 \text{ cm}^{-3}$  whereas below 85 km there is a wide disparity in deduced nitric oxide densities with the noontime profile exhibiting much smaller densities than the early morning profile.

The nitric oxide densities deduced by Koshelev and Belinska [KB-74c] lie between  $10^7$  and  $2 \times 10^8 \text{ cm}^{-3}$  between 100 and 200 km. to 180 km, these deduced nitric oxide densities are in fair agreement with the daytime observed and calculated nitric oxide densities shown Fig. 5-1, provided allowance is made for the solar activity. However above 180 km, the densities of Koshelev and Belinskaya [KB-74c] increase and become significantly greater than expected on the basis of the treatment of Section 5.2.3. The densities deduced by Oliver [Ol-74a] between 110 and 280 km, tend to be slightly lower than the data calculational results shown on Fig. 5-1 for altitudes below 180 km, but exhibit a general increase above 180 km in contrast to direct observations and calculations.

A difficulty with these indirect determinations of nitric oxide densities is the necessity of modelling correctly the production and loss mechanisms for nitric oxide. The results of indirect determinations of nitric oxide densities have not been included in the process of selecting a nitric oxide profile in the present report.

Chakravarty and Mitra [See MR-74b] have deduced nitric oxide densities from ion composition measurements over a solar cycle variation. They find a corresponding nitric oxide density variation of a factor of four down to 100 km with a decreasingly smaller variation down to 90 km. While a smoothed profile [CI-72] of solar flux over a solar cycle has a larger variation in  $F_{10.7}$  values than contained in the data of Table 5-1 above, nevertheless, the results of Chakravarty and Mi

[MR-74b] lend credence to a variation of nitric oxide density with solar activity below 120 km. By using the directly obtained data at 110 km [Ba-66d, Me-71, Kr-70a, OJ-74, Ti-73], the most probable variation in nitric oxide density with decimetric solar flux is found to be a factor of two increase between  $F_{10.7}$  values of 90 and 145, respectively; the uncertainty is such that the factor could lie between zero and four. (Further discussion is presented below in Section 5.4.2.) However, in the present construction of profiles, the approximation of solar flux independence for nitric oxide densities below 120 km is retained for convenience and simplicity in quantitative description of the profile.

#### 5.4.2 Late Reports on Nitric Oxide

Two reports [GS-75a, MS-75a] have recently appeared in which nitric oxide densities in the E-region are determined indirectly on the basis of electron and ion densities. In both reports, the dependence of the deduced nitric oxide density on solar activity is demonstrated. Monroe and Smith [MS-75a] have found at 130 km that the nitric oxide density increases with the sunspot number; this relation is shown on Fig. 5-6 along with the NO densities determined directly or calculated at 110 km [Ba-66d, Me-71, Kr-70a, OJ-74, Ti-73] and which have been considered in previous sections. Thus one can see that roughly the same average dependence on sunspot number is found for nitric oxide by direct measurement or calculation at 110 km as by indirect determination at 130 km for sunspot numbers greater than 20. The absolute concentrations of nitric oxide determined by Monroe and Smith [MS-75a] at sunrise, are, however, larger by factors of 3 to 4 than the daytime density measurements of Barth [Ba-66c] and Meira [Me-71]. These results also disagree with calculations [OJ-74, Hu-73a]. The method of analysis used by Monroe and Smith [MS-75a] requires that the increase in electron

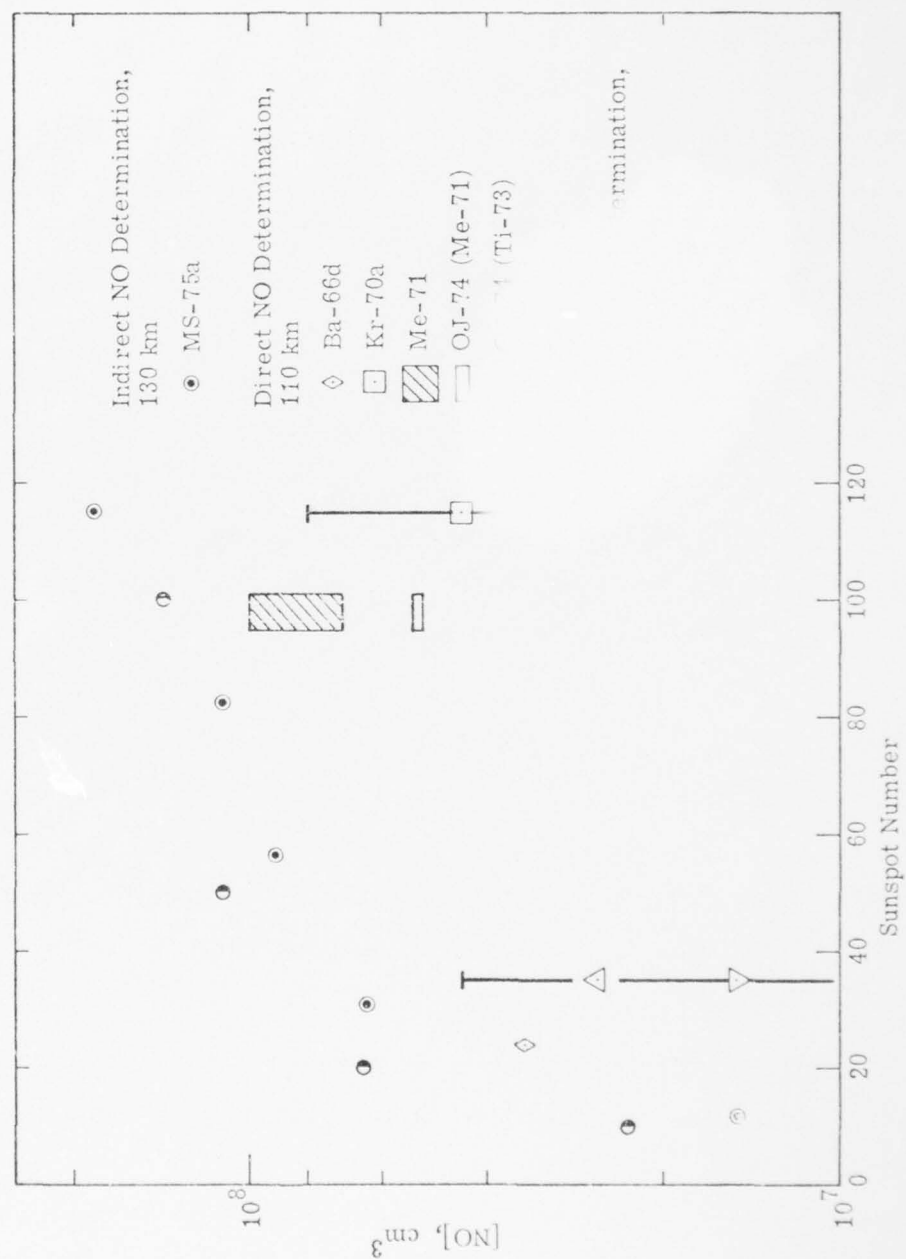


Fig. 5-6. Dependence of Nitric Oxide Density on Sunspot Number



density in the sunrise E-region result mainly from ionization of nitric oxide by Lyman- $\alpha$  radiation for a specified range of solar zenith angles.

Golshan and Sechrist [GS-75a], using a different set of observations than those of Monro and Smith [MS-75a], employ the observed  $[\text{NO}^+]/[\text{O}_2^+]$  ratios in conjunction with atmospheric composition, flux and cross-section data to deduce nitric oxide densities; at 105 km, they find the dependence on sunspot number,  $R_z$ , of the nitric oxide density as shown on Fig. 5-6. These data are qualitatively consistent with the data at 110 km shown on Fig. 5-6 and are roughly a factor of two larger. The dependence of nitric oxide density on sunspot number is related [GS-75a] to the corresponding variation in the intensity of radiation in the 10 to 130 Å spectral region. Thus the rationale for variation of nitric oxide density with solar activity differs for altitudes near 100 km and those near 200 km. From the data assembled on Fig. 5-6, a clear justification for the future refinement of the model presented in this review is derivable.

Golshan and Sechrist [GS-75a] also find a seasonal dependence: above 100 km, the nitric oxide density increases from winter to summer. This is in contrast to the calculations of Oran et al. [OJ-74] in which the calculations for winter predict more nitric oxide than those for summer at altitudes above 100 km and for a constant molecular oxygen density.

A recent calculation on the seasonal and latitudinal variation of oxides of nitrogen in the stratosphere has been reported [Vu-75]. This work consists of a preliminary, two-dimensional calculation which incorporates photochemical, vertical and horizontal (north-south) transport processes. The preliminary nature is primarily a result of the parameterization of the ozone and temperature distributions and the mean

meridional motions rather than their calculations. The profiles from this calculation at  $45^\circ$  latitude for both summer and winter are shown on Fig. 5-4 for altitudes between 17 and 48 km.

## 5.5 NIGHTTIME NITRIC OXIDE DENSITIES

### 5.5.1 Measurements

Two nighttime rocket flights [OP-72, OG-73] have gathered data on nitric oxide densities. On one rocket flight [OG-73] at  $39^\circ\text{N}$  latitude, a cryocooled mass spectrometer was the detector; on the companion flight [OP-72] an uncooled detector was used; nevertheless the results of the two measurements [OP-72, OG-73] agree over the altitude range between 170 and 210 km. In plotting the data of Offermann et al. [OP-72] on Fig. 5-1, the assumption has been made that the ratio of the M30/M28 signal for the two flights [OP-72, OG-73] is the same as the ratio of the densities; MX is the mass of species X. However, since Offermann and Grossmann [OG-73] chose not to consider the data obtained with the uncooled detector, we will not further consider the uncooled, mass-spectrometer data. For the data presented by Offermann and Grossmann [OG-73], no correction was made for the possible contributions to the nitric oxide signal from interactions occurring in the mass spectrometer; thus the data on Fig. 5-1 represent upper limits. Nevertheless, the magnitudes of the deduced densities are clearly in contradiction to the results of calculations, as discussed below, and indirect determinations of densities [KB-74c] since the nighttime nitric oxide densities of Offermann and Grossmann are greater than those measured or calculated for daytime. Since these data cannot be rationalized at present, the selected nighttime density profile for nitric oxide will rely solely on calculations.

### 5.5.2 Calculations and Selection of Nitric Oxide Profile

The diurnal variation in nitric oxide density above 70 km obtained from the calculations of Oran et al. [OJ-74] and Hunt [Hu-73a] shows a smaller density for nitric oxide at midnight than at noon above an altitude of 100 km. These relative values are also obtained in the deduced densities of Koshelev and Belinskaya [KB-74c]. In the calculations [OJ-74, Hu-73a], the difference increases with altitude and at 160 km, the noon nitric oxide density is greater than the midnight density by factors of 1.8 [Hu-73a],  $\sim 3.4$  [OJ-74 for Me-71] and  $\sim 7.1$  [OJ-74 for Ti-73]. We select an average value of 4 ( $\equiv [\text{NO}]_{\text{noon}} / [\text{NO}]_{\text{midnight}}$ ) at 160 km, a value of 1 at 100 km and a maximum value of 10 at arbitrarily high altitudes; then

$$[\text{NO}]_{\text{midnight}} = [\text{NO}]_{\text{noon}} \left\{ \frac{(h - 100)^2 + 7200}{10(h - 100)^2 + 7200} \right\} \quad (9)$$

where  $h$  is in km.

Below 70 km, a significant diurnal variation in nitric oxide density is predicted by Hunt [Hu-73a], Shimazaki and Laird [SL-70a, SL-72a] and Thomas [Th-71a]. In view of the disparity between these calculations and observations for daytime conditions in the altitude range below 70 km, the calculated density profiles for midnight conditions must be viewed skeptically. Therefore, the fall in nitric oxide density below 70 km will have a large error associated with it. We shall use the results of Shimazaki and Laird [SL-70a, SL-72] from 70 to 50 km and extrapolate below 50 km. The use of these calculations [SL-70a, SL-72] is based on the better agreement with observations in the region between 50 and 70 km than for the calculations of Hunt [Hu-73a]. The values are shown on Table 5-3. A partial plotting of these values is given on Fig. 5-5. Values are interpolated between 65 and 85 km.

## 6. DENSITY PROFILE OF ATOMIC NITROGEN

### 6.1 INTRODUCTION

Despite the fact that a moderate number of measurements and of calculations of atomic nitrogen densities have been made, larger discrepancies exist among the measured values and between the measured and calculated values than for any of the other atmospheric species considered in this report. Thus the selected profile has a large uncertainty associated with the atomic nitrogen densities.

### 6.2 MEASUREMENTS

The measurements of atomic nitrogen have been made at altitudes above 100 km on rocket flights with mass spectrometers [GH-68a, HN-72a, MB-72b, OP-72, Po-72a] and by a chemiluminescent technique involving the reaction of nitrogen atoms with ethylene. The data from these measurements are shown on Fig. 6-1. The mass spectrometric measurements are difficult to make. Important corrections to the raw data must be made, as for example, to account for the ionization of molecular nitrogen to  $N_2^{++}$  and  $N^+$  [HN-72a]. Also, the possible influence of vibrationally excited nitrogen has been considered [BB-74]. One may also ask whether electron excitation of molecular nitrogen to predissociating states contributes ultimately to the measured nitrogen ion signal. At electron energies of 25 eV, for example, the cross section for dissociation of molecular nitrogen [Wi-66] (accounted for primarily by predissociation of excited states of molecular nitrogen) is comparable to the cross section for ionization of molecular nitrogen. Can the nitrogen atoms formed by electron impact contribute to the nitrogen ion signal and in significantly different ways in the atmosphere and the laboratory calibration measurements?

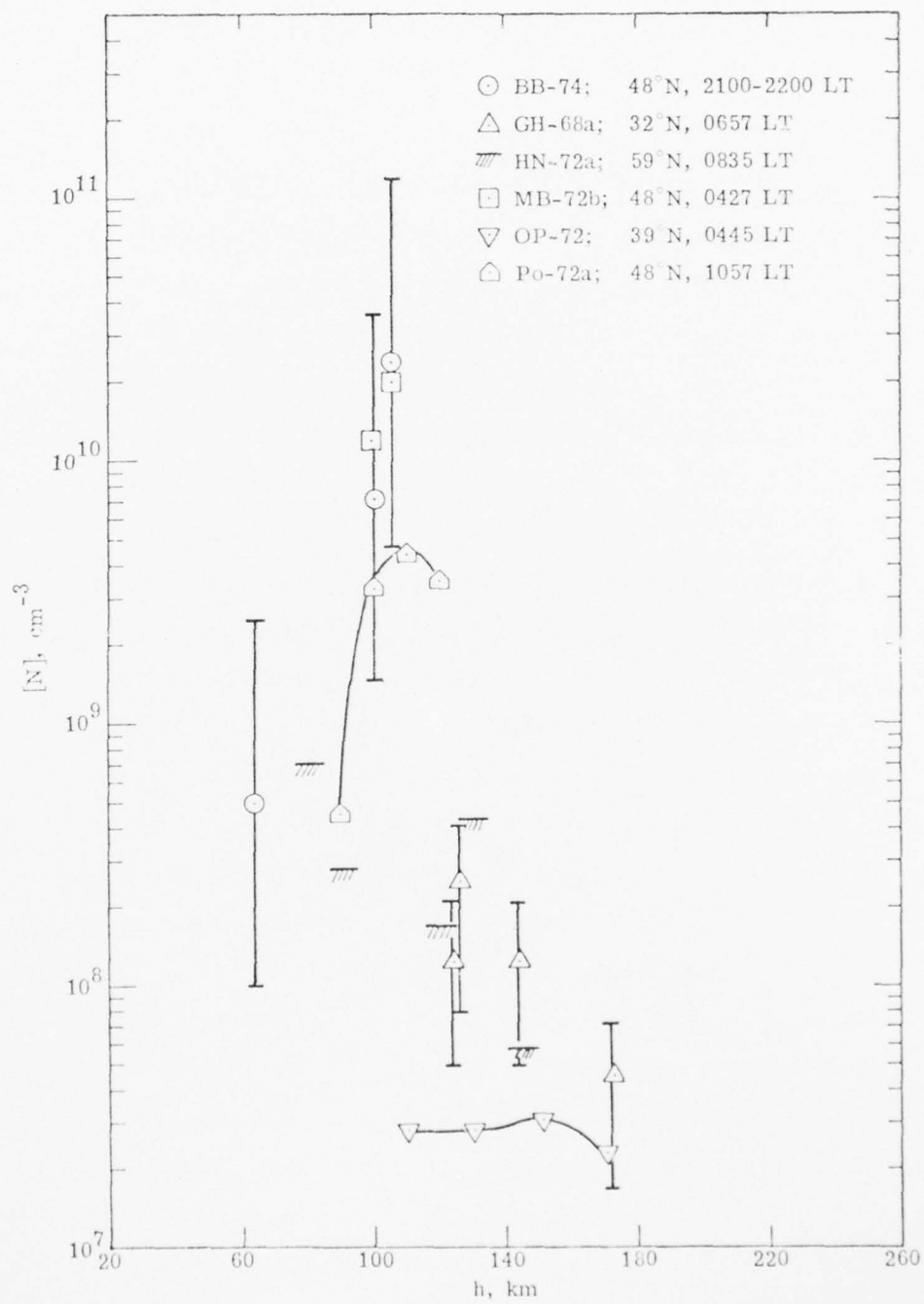


Fig. 6-1. Measured Atomic Nitrogen Densities.

The chemiluminescent measurements were based on a rate coefficient derived from experiments in one laboratory [BB-74]. On the other hand, any error in the rate coefficient is more likely to result in too large a rate coefficient which would have the effect of increasing the nitrogen atom density calculated from the proper coefficient.

The measurements shown on Fig. 6-1 were conducted in the early morning or at night with one exception. There is no significant correlation of the spread in measurements with latitude; the experiments conducted at Volgograd ( $48^{\circ}\text{N}$ ) have yielded larger nitrogen atom densities than experiments conducted elsewhere. Note also, that the experiments of Hickman and Nier [HN-72a] yield only upper limit estimates of atomic nitrogen densities. For the experiments of Hickman and Nier [HN-72a] and Offermann et al. [OP-72], we have used the CIRA 1972 [CI-72] mean atmosphere to convert from the signal ratios of mass 14 to mass 28 to nitrogen atom densities and for the experiment of Pokhunkov [Po-72a], a mean of the atmospheres corresponding to  $T_{\infty} = 1200^{\circ}\text{K}$  and  $1300^{\circ}\text{K}$  has been used for the conversion. The conversion of the data of Martynkevich and Byuro [MB-72b] has been given by Balabanova et al. [BB-74].

The measurements shown in Fig. 6-1 have been examined with respect to the solar 10.7 cm flux observed for the day of the rocket flight; any correlation of the atomic nitrogen density with the 10.7 cm flux is obscured by differences in the atomic nitrogen density of one to two orders of magnitude for measurements corresponding to very similar solar flux values.



### 6.3 MODEL CALCULATIONS

The results of model calculations for atomic nitrogen are shown on Fig. 6-2. The calculations of Hunt [Hu-73a] and Strobel and colleagues [St-71, St-72a, OJ-74] have included ionic reactions as well as neutral reactions and transport. The calculations of Shimazaki and Laird [SL-70a, SL-72, SL-72a] have not included ionic reactions and their calculations of atomic nitrogen densities are in error at least for altitudes above 85 km. Nicolet [Ni-70] has calculated atomic nitrogen densities but with photo-equilibrium conditions. The calculations of Hunt [Hu-73a] are more comparable with the Oran et al. [OJ-74] calculations for the experimental conditions of Tisone [Ti-73] than for those of Meira [Me-71] on the basis of solar activity; the Hunt calculations yield densities at least a factor of three smaller than those of Oran et al. for conditions of Tisone's experiment. The calculations of Oran et al. [OJ-74] show, for both day and night conditions, a larger nitrogen atom density for the conditions of Tisone's experiment [Ti-73] than for the condition of Meira's experiment [Me-71] at altitudes above 100 km. This is consistent with the expectation, based on the analysis of Section 5.2.3, that a lower solar flux would result in a larger atomic nitrogen density. However, for the higher altitudes, the effect of solar flux on density is apparently considerably smaller for atomic nitrogen than for nitric oxide, at least in the daytime.

### 6.4 SELECTION OF ATOMIC NITROGEN PROFILE

Because of the very large disparity among measurements and calculations, a noon and midnight profile will be derived by freely drawing a curve through the calculated profiles and no attempt will be made to consider the effect of solar activity on atomic nitrogen densities. The

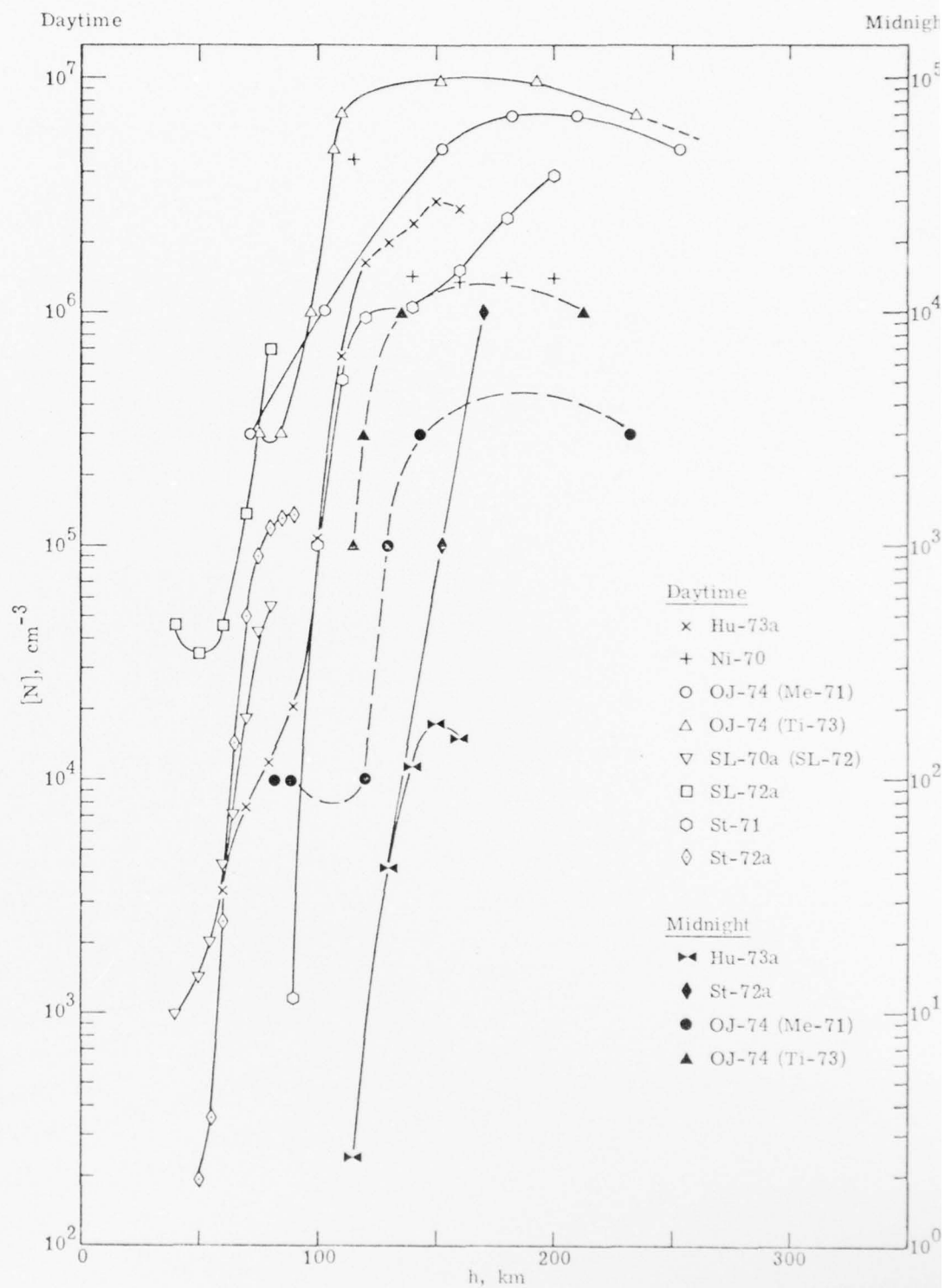


Fig. 6-2. Calculated Atomic Nitrogen Densities.

greatest weight is given to the recent calculations of Oran et al. [OJ-74]; zero weight is given to the measurements although this might be negligent.

Data for the selected profile are listed in Table 6-1 and shown on Fig. 6-3 for altitudes up to 230 km.

Table 6-1. Nitrogen Atom Densities for Noon and Midnight Conditions.

h, km	[N], cm <sup>-3</sup>		h, km	[N], cm <sup>-3</sup>	
	Noon	Midnight		Noon	Midnight
0	1.0(0)	1.0(0)	120	3.4(6)	7.3(4)
5	↓	↓	125	4.3(6)	1.6(5)
10			130	5.0(6)	3.0(5)
15			135	5.9(6)	4.0(5)
20			140	6.5(6)	4.8(5)
25			145	7.0(6)	5.6(5)
30			150	7.5(6)	6.3(5)
35			155	7.9(6)	6.8(5)
40			160	8.1(6)	7.2(5)
45			165	8.3(6)	7.5(5)
50			170	8.4(6)	7.8(5)
55	5.0(2)	↓	175	8.5(6)	7.9(5)
60	1.8(3)		180	8.5(6)	7.9(5)
65	7.4(3)		185	8.4(6)	7.8(5)
70	2.1(4)		190	8.3(6)	7.7(5)
75	5.2(4)		195	8.2(6)	7.5(5)
80	1.1(5)		200	8.1(6)	7.2(5)
85	2.2(5)		205	8.0(6)	6.9(5)
90	3.7(5)		210	7.8(6)	6.6(5)
95	6.4(5)		215	7.5(6)	6.3(5)
100	1.0(6)	7.0(2)	220	7.3(6)	6.0(5)
105	1.3(6)	3.1(3)	225	7.1(6)	5.6(5)
110	2.0(6)	1.1(4)	230	6.8(6)	5.1(5)
115	2.7(6)	3.0(4)	235	†	†

† Above 230 km,  $[N] = ([N]/[N_2])_{230} [N_2]$  where the subscript indicates the nitrogen atom to nitrogen molecule ratio at 230 km.

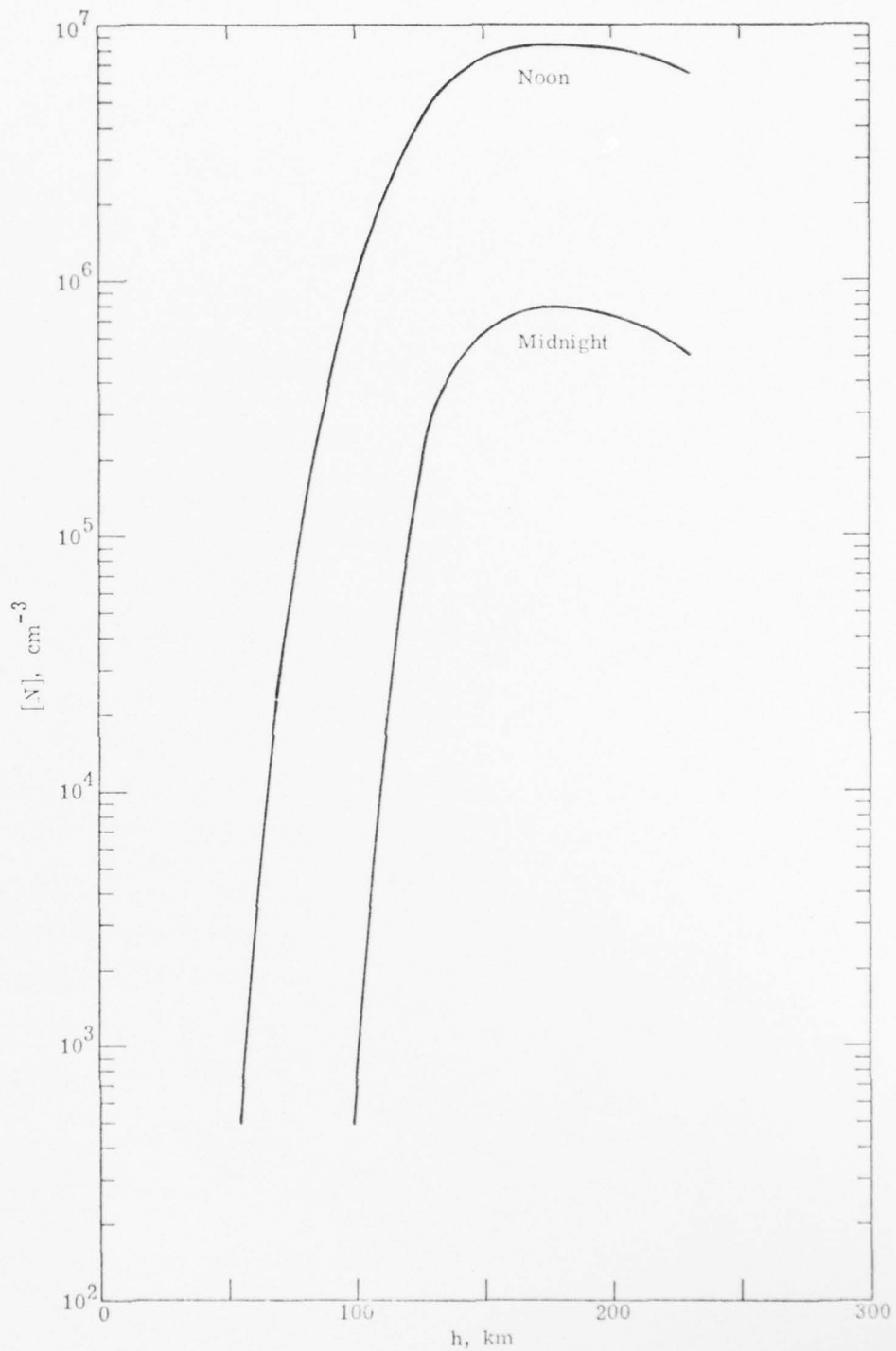


Fig. 6-3. Atomic Nitrogen Profile for Noon and Midnight Conditions

## 7. DENSITY PROFILE OF NITROGEN DIOXIDE

### 7.1 INTRODUCTION

Only recently has nitrogen dioxide been detected at altitudes much above ground level [MK-68b, MM-69, GM-70c]. Thus it is not surprising that nitrogen dioxide densities show a scatter of an order of magnitude in the principal altitude region of the measurements, i. e., the stratosphere.

The selected nitrogen dioxide profile applies to the altitude region from ground level to 160 km. This profile is based on measurements and calculations for altitudes below 30 km but above this model calculations are the sole basis.

### 7.2 DAYTIME NITROGEN DIOXIDE DENSITIES

#### 7.2.1 Measurements

The measurements of nitrogen dioxide are generally limited to the altitude range from about 14 to 34 km and in that range show large scatter. The scatter in the measured densities is particularly large only in the range from about 14 to 18 km. This is shown in Fig. 7-1. Note that the densities attributed to Farmer [Fa-70] are based on a tentative value of the mixing ratio determined for the altitude range 15 to 20 km. By using the extensive data on nitric acid, Schiff [Sc-69] has calculated a mixing ratio band (converted here to densities) for the U. S. Standard Atmosphere [US-62] number densities) for the altitude range from 14 to 27.6 km; the derived band of nitrogen dioxide densities favors small values below 20 km. Also supporting the nitrogen dioxide densities are the values derived by Schiff [Sc-69].



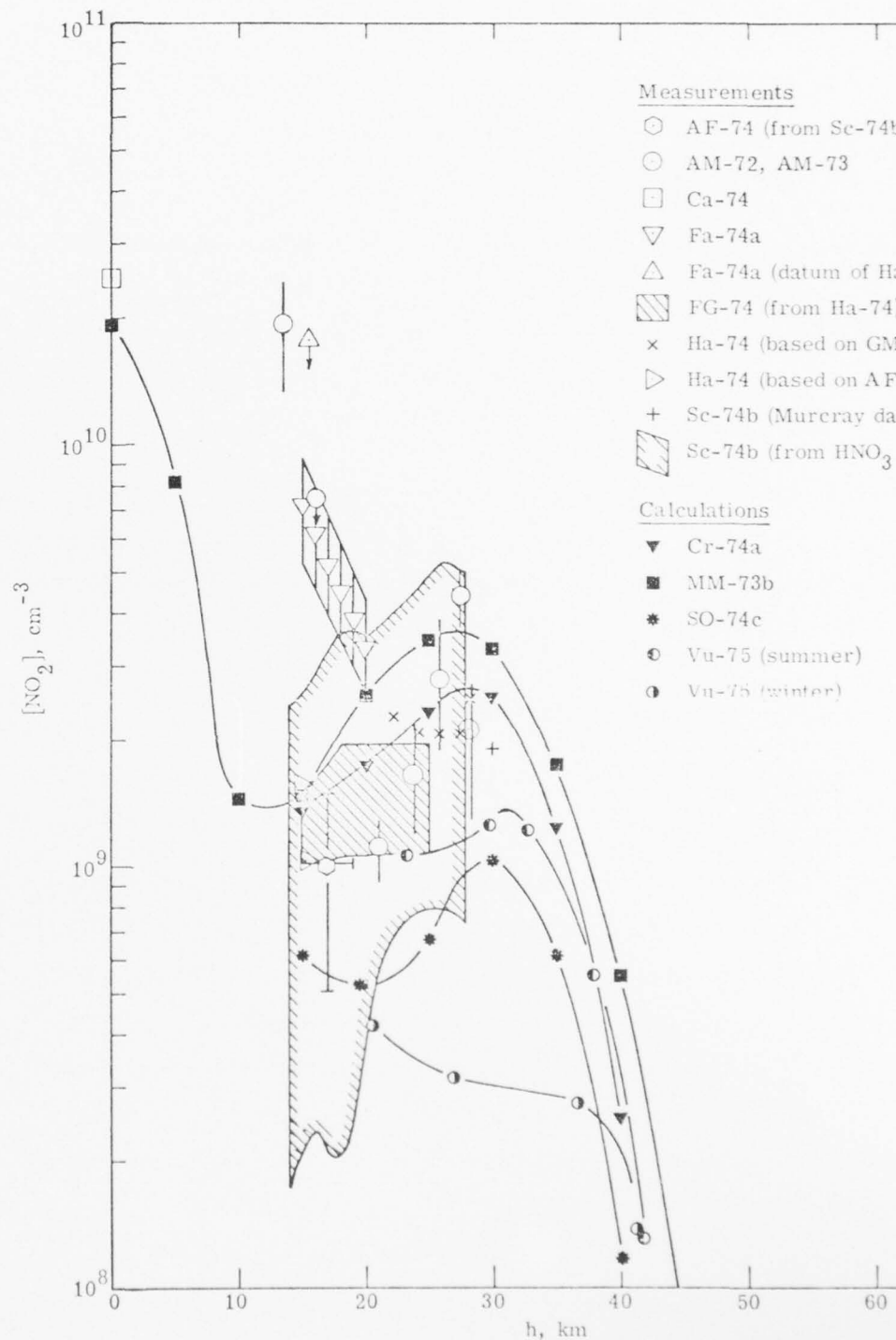


Fig. 7-1. Nitrogen Dioxide Densities Below 50 km.

the data of Ackerman et al. [AF-74], the data of Fontanella et al. [FG-74] as reported by Hard [Ha-74], and the value calculated by Murcra based on data of Ackerman et al. [AF-73a] and as reported by Hard [Ha-74].

The measurements of nitrogen dioxide densities have generally been absorption measurements with the sun as the radiation source. The measurements shown on Fig. 7-1 but with the three exceptions noted below are from observations of the  $\text{NO}_2$ - $\nu_3$  band at  $6.25 \mu\text{m}$ ; this band is strong and relatively free from interference. Heretofore, a difficulty with the use of the  $\nu_3$  band has been uncertainty about the rotational quantum assignments. Reference to new laboratory data of Murcra of the  $\nu_3$  band of nitrogen dioxide is made by Schiff [Sc-74b]; Schiff has reported the density at 30 km based on these new data as calculated by Murcra and as shown on Fig. 7-1. The measurements of Ackerman and Muller [AM-72, AM-73] and of Farmer [Fa-74a] have used the  $\nu_1 + \nu_3$  band at  $3.4 \mu\text{m}$  which is much weaker than the  $\nu_3$  band and is overlapped by methane bands. Harries [Ha-73e] has used high resolution emission measurements in the sub-millimeter infrared spectral region. The datum of Harries, as given on Fig. 7-1, is a revision of earlier nitrogen dioxide densities [Ha-73e]; the revised value is reported by Farmer [Fa-74a] as well as Schiff [Sc-74b].

All of the measurements of Fig. 7-1 have been made between about  $30^\circ\text{N}$  and  $50^\circ\text{N}$  latitude, except those of Harries [Ha-73e]; for these aircraft observations, the latitude and longitude varied widely from  $40^\circ\text{S}$  to  $48^\circ\text{N}$  and from  $8^\circ\text{W}$  to  $151^\circ\text{E}$ . The accuracy of the measurements was limited and any dependence on geographic location is obscured. The measurements of Fig. 7-1 were made for zenith angles close to  $90^\circ$ .

AD-A043 499

GENERAL RESEARCH CORP SANTA BARBARA CALIF

F/G 17/9

THE ROSCOE MANUAL. VOLUME 14B. MIDLATITUDE DENSITY PROFILES OF --ETC(U)

JUN 75 B F MYERS

DNA001-74-C-0182

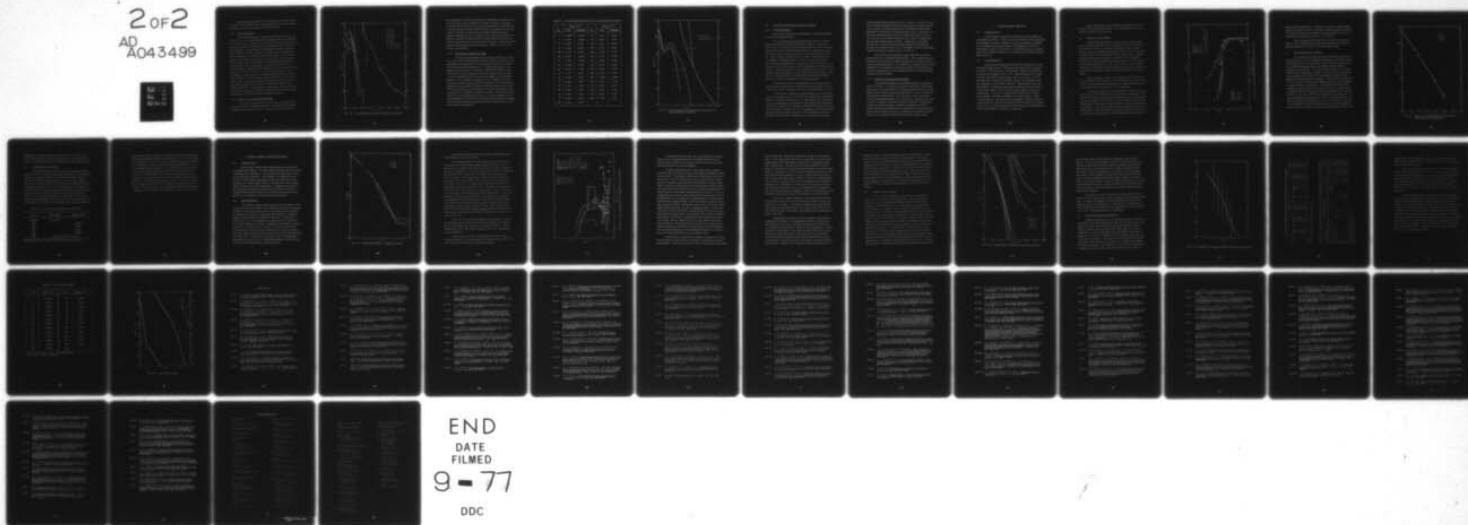
UNCLASSIFIED

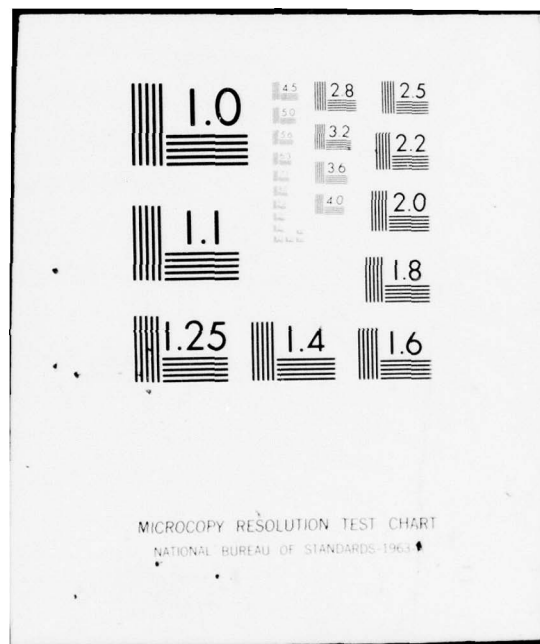
DNA-3964F-14B

NL

2 OF 2

AD  
A043499





Additional measurements not given on Fig. 7-1 have been made by Brewer et al. [BM-73a]; these measurements have not been included on the basis of the discussion given by Schiff [Sc-74b].

#### 7.2.2 Model Calculations

The model calculation results are shown both on Fig. 7-1 and on Fig. 7-2. For the calculations of McConnell and McElroy [MM-73b], the curves on Figs. 7-1 and 7-2 represent their model A which is based on the best estimate of parameters; the calculations apply to 30°N latitude at equinox. The calculations of Shimazaki and Ogawa [SO-74c], which are shown on Figs. 7-1 and 7-2, are the model 4 calculations of these investigators (see Table 5 of SO-74c) and apply to 45°N latitude at equinox. The shape of the profile is similar to that of McConnell and McElroy [MM-73b] but the profile has smaller densities; these differences may be due to differences in rate coefficients [SO-74c]. A third calculation, applicable at low altitudes, was carried out by Crutzen [Cr-74a] for  $\sec \theta = 1.4$  where  $\theta$  is the solar zenith angle. This calculation is in best agreement with experimental data between 25 and 30 km and also in good agreement with the data of Murcray [Ha-74] at 16 km. The calculations of Hunt [Hu-73a] yield densities an order of magnitude larger at 60 km than those calculated by McConnell and McElroy [MM-73b]. The calculations of Shimazaki and Laird [SL-72a] have larger nitrogen dioxide densities between 40 and 60 km than other calculations and smaller densities between 60 and 70 km.

#### 7.2.3 Selection of Nitrogen Dioxide Profile

The profile is selected mainly on the basis of calculations but taking into account the experimental data. At ground level, the datum reported by Cadle [Ca-74] is used. Between ground level and 10 km,

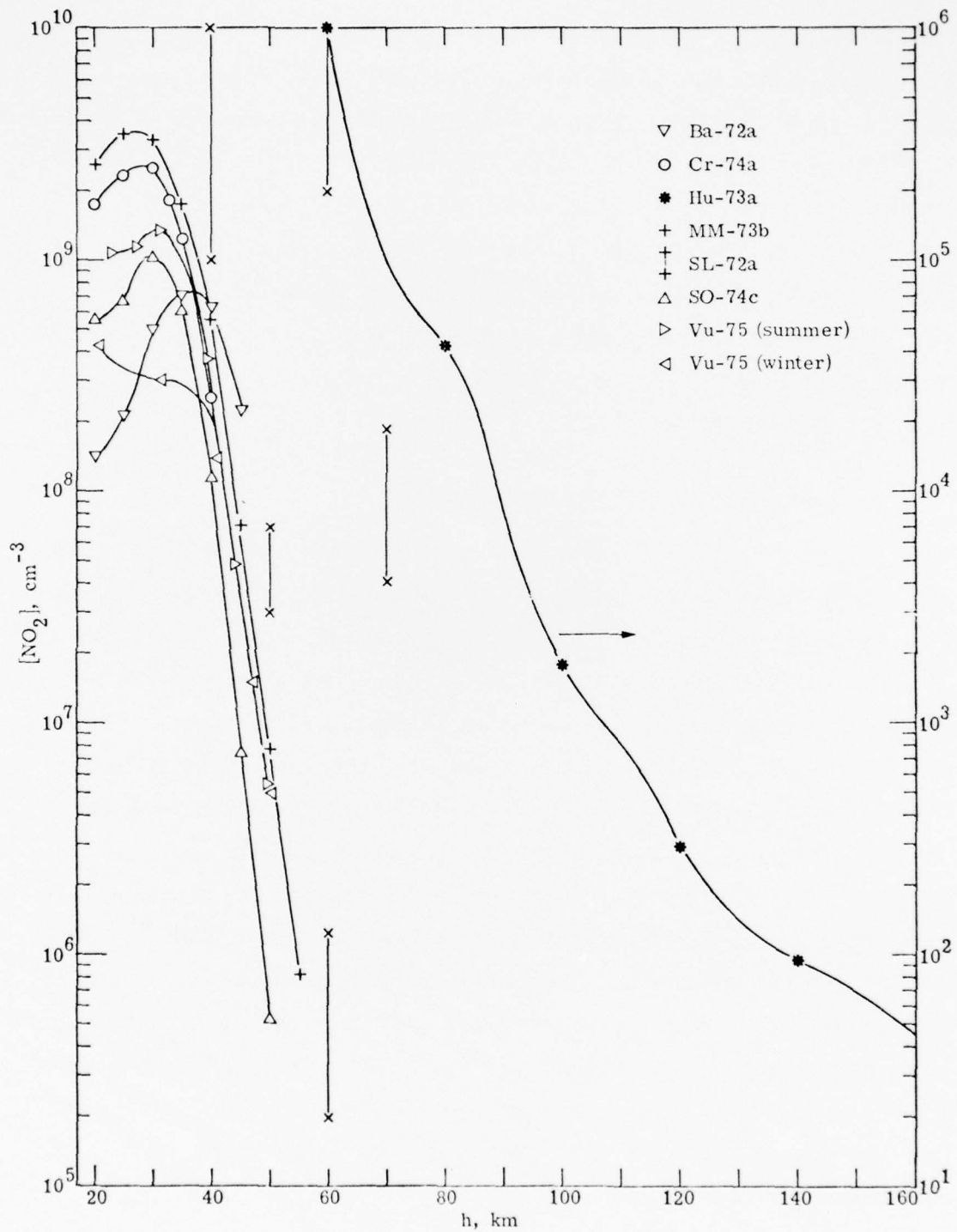


Fig. 7-2. Calculated Nitrogen Dioxide Densities Above 20 km.



the calculations of McConnell and McElroy [MM-73b] are adopted; from 10 to near 40 km, the calculations of Crutzen [Cr-74a] are used and from above 40 to 55 km, those of McConnell and McElroy [MM-73b] and for 60 km and above, those of Hunt [Hu-73a]. Interpolation between the results of Crutzen [Cr-74a] at 35 km and those of McConnell and McElroy [MM-73b] at 45 km and between the results of McConnell and McElroy [MM-73b] at 50 km and those of Hunt [Hu-73a] at 65 km provided the transitions from one calculation to the other. Above 70 km, the profile of Hunt [Hu-73a] has been smoothed. Table 7-1 and Fig. 7-3 show the selected data.

#### 7.2.4 Late Reports on Nitrogen Dioxide

After the nitrogen dioxide profile had been selected, a calculation on the seasonal and latitudinal variation of oxides of nitrogen in the stratosphere was reported [Vu-75] as indicated in Section 5.4.2 above. The profiles from this calculation for 45° latitude both summer and winter are shown on Figs. 7-1 and 7-2. Between 41 and 60 km, these profiles [Vu-75] are in agreement with other profiles shown on Figs. 7-1 and 7-2 but below 41 km show generally smaller nitrogen dioxide densities. The calculation of Vupputuri [Vu-75] exhibits a decline in the nitrogen dioxide mixing ratio from the summer to the winter pole for altitudes below about 41 km and this is indicated by the curves on Figs. 7-1 and 7-2 (densities were computed from the calculated mixing ratios by using the U. S. Standard Atmosphere [US-66]). A superficial assessment of the measurements shown on Fig. 7-1 does not support the seasonal dependence of nitrogen dioxide densities as calculated by Vupputuri [Vu-75]; however both the calculations and the measurements are in the early stages of development.

Table 7-1. Nitrogen Dioxide Densities for Noon and Midnight Conditions.

h, km	[NO <sub>2</sub> ], cm <sup>-3</sup>		h, km	[NO <sub>2</sub> ], cm <sup>-3</sup>	
	Noon	Midnight		Noon	Midnight
0	2.5(10)	3.5(10)	85	1.2(4)	1.2(4)
5	8.3(9)	1.2(10)	90	6.4(3)	6.4(3)
10	1.4(9)	2.7(9)	95	3.4(3)	3.4(3)
15	1.4(9)	2.0(9)	100	1.8(3)	1.8(3)
20	1.8(9)	2.5(9)	105	1.1(3)	1.1(3)
25	2.4(9)	4.15(9)	110	6.7(2)	6.7(2)
30	2.5(9)	4.55(9)	115	4.3(2)	4.3(2)
35	1.25(9)	3.0(9)	120	2.8(2)	2.8(2)
40	3.4(8)	1.6(9)	125	1.9(2)	1.9(2)
45	7.1(7)	9.2(8)	130	1.4(2)	1.4(2)
50	7.8(6)	5.2(8)	135	1.15(2)	1.15(2)
55	2.3(6)	3.0(8)	140	9.5(1)	9.5(1)
60	7.0(5)	1.4(8)	145	8.0(1)	8.0(1)
65	2.6(5)	5.5(7)	150	7.0(1)	7.0(1)
70	1.0(5)	1.2(7)	155	6.0(1)	6.0(1)
75	5.0(4)	1.0(6)	160	4.6(1)	4.6(1)
80	2.4(4)	3.0(4)			

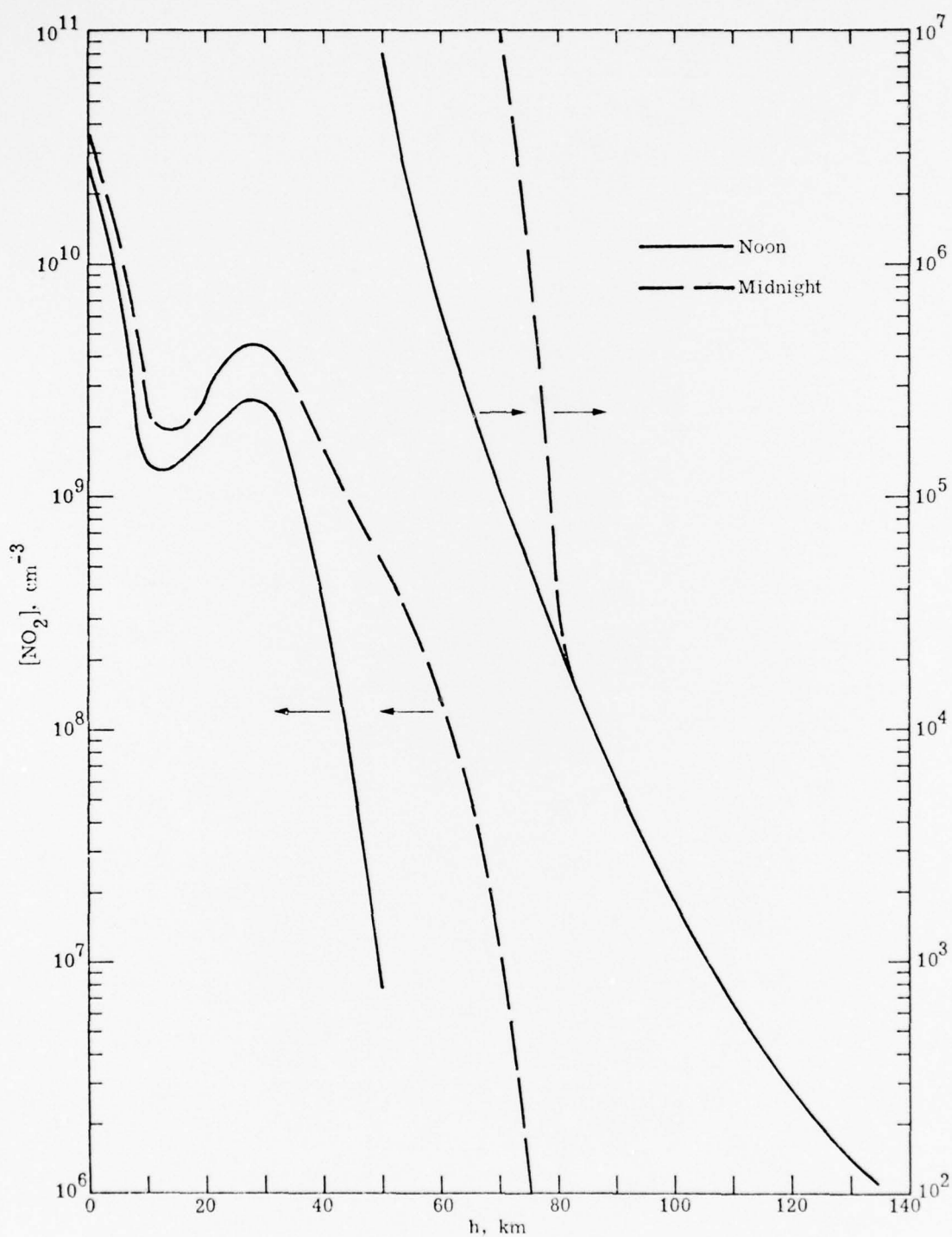


Fig. 7-3. Nitrogen Dioxide Profile Between 0 and 140 km for Noon and Midnight Conditions.

### 7.3 NIGHTTIME NITROGEN DIOXIDE DENSITIES

#### 7.3.1 Model Calculations

Only model calculations are available for estimating the nighttime nitrogen dioxide densities.

The calculations of Shimazaki and Ogawa [SO-74c] show the diurnal variation in nitrogen dioxide density at 20 km. Much of the nitric oxide is converted to nitrogen dioxide within a short time interval about twilight and the nitrogen dioxide density is constant until sunrise. While other species densities increase at sunset and during the night, i.e.,  $\text{NO}_3$  and  $\text{N}_2\text{O}_5$ , these densities are small. The calculated ratio of midnight to noon  $\text{NO}_2$  densities is 1.87; in combination with the selected nitrogen dioxide daytime profile, this ratio would result in a nitrogen dioxide nighttime density which exceeds the total of the daytime densities of  $\text{NO}$  and  $\text{NO}_2$  from the corresponding selected profiles. This difficulty apparently reflects, in part, the relatively small values of the daytime nitrogen dioxide density calculated by Shimazaki and Ogawa [SO-74c] at 20 km in comparison to the measured values.

Below 20 km, the sum of the densities of nitric oxide and nitrogen dioxide corresponds to a fixed value of the mixing ratio [Le-73]; at night, nitric oxide is rapidly converted to nitrogen dioxide [Le-73].

At 60 km, the calculations of Hunt [Hu-73a] and of Shimazaki and Laird [SL-70a, SL-72, SL-72a] show the nighttime nitrogen dioxide density to be equal to the daytime nitric oxide density (plus the daytime nitrogen dioxide density, presumably) and this obtains also between 40 and 60 km according to the calculations of Shimazaki and Laird [SL-70a, SL-72, SL-72a]. At 60 km, the ratio of midnight to noon nitrogen dioxide densities given by Hunt [Hu-73a] is 794, by Shimazaki and Laird [SL-70a, SL-72, SL-72a] is 1232 and, by use of the nitric oxide and

nitrogen dioxide daytime profiles of Figs. 5-5 and 7-3, is 212. For the case of the Hunt calculation [Hu-73a], the large ratio results primarily from a greater calculated daytime nitric oxide density at 60 km than indicated by observations on which the profile of Fig. 5-5 is based. In the case of the Shimazaki and Laird calculation [SL-70a, SL-72, SL-72a], the large ratio results primarily from a smaller calculated daytime nitrogen dioxide density at 60 km. Differences in calculated daytime nitric oxide and nitrogen dioxide densities at high latitudes [SL-72a] also result in larger ratios of midnight to noon nitrogen dioxide densities than 212 as found from Figs. 5-5 and 7-3.

Above 80 km, the calculations of Hunt [Hu-73a] show little diurnal variation in nitrogen dioxide densities. This is expected on the basis that reactions of atomic oxygen dominate the formation and loss of nitrogen dioxide above 80 km. The absence of a diurnal variation is also indicated by the calculations of Shimazaki and Laird [SL-72a] whereas in earlier calculations for lower latitudes [SL-70a, SL-72] the diurnal variation persists to 90 km.

### 7.3.2 Selection of Nitrogen Dioxide Profile

The selected midnight nitrogen dioxide profile is presented in Table 7-1 and Fig. 7-3. Between ground level and 60 km, the daytime nitric oxide is converted entirely to nitrogen dioxide and the sum of this quantity and the daytime nitrogen dioxide density is taken to be the midnight nitrogen dioxide density. This results in a ratio of midnight to noon nitrogen dioxide densities of 1.4 at 20 km as compared to the value of 1.87 as computed by Shimazaki and Ogawa [SO-74c]. Above 80 km, any diurnal variation in  $\text{NO}_2$  is neglected. Between 60 and 80 km, nitrogen dioxide midnight densities are obtained by interpolation guided by the relative change in the ratio of midnight to noon nitrogen dioxide density values calculated by Hunt [Hu-73a] in this altitude range.



## 8. CARBON DIOXIDE PROFILES

### 8.1 INTRODUCTION

Carbon dioxide is apparently well mixed in the atmosphere up to altitudes near 100 km. There is extensive evidence for this up through the troposphere [Ca-74], at altitudes in the range 44-62 km [SH-69a] and, by deduction from measurements of CO<sub>2</sub> densities in the lower thermosphere [OG-73], up to 100 km. Above 100 km, CO<sub>2</sub> is generally taken to be in diffusive equilibrium on the basis of observations [OG-73, OP-72, OZ-71].

### 8.2 MEASUREMENTS

Measurement of CO<sub>2</sub> densities up to the stratosphere are summarized by Cadle [Ca-74]. The annual mean mixing ratio is reported to be  $3.22 \times 10^{-4}$  [Ca-74] for a 45°N latitude. Between 11 and 20 km, the value recommended is  $3.21 \times 10^{-4}$ . Between 20 and 37 km, Ackerman [Ac-74] found the volume mixing ratio to be  $2.6 \pm 0.7 \times 10^{-4}$  by absorptiometry; between 44 and 62 km, Scholz et al. [SH-69a] found the mixing ratio to be  $(3.228 \pm 0.025) 10^{-4}$ . Observations in the lower thermosphere, at altitudes between 120 and 140 km have been made on rocket flights [OG-73, OP-72, OZ-71] using a helium-cooled mass spectrometer. From these measurements, the densities of CO<sub>2</sub> at three altitudes, 124, 129, and 135 km, have been obtained. These measurements are consistent with the assumption of diffusive equilibrium above 100 km. Recent measurements [SU-74] of the infrared emission from the  $\nu_2$  band of CO<sub>2</sub> should yield a CO<sub>2</sub> profile between 60 and 150 km when reduction of the data is completed.



All the observations considered here are plotted on Fig. 8-1 in terms of the volume mixing ratios. Also, the rocket flight measurements are plotted as  $\text{CO}_2$  densities.

### 8.3 MODEL CALCULATIONS

Three model calculations for  $\text{CO}_2$  have been recently made [Hu-73a, WM-72, HO-70]. The most extensive of these calculations is that of Hunt [Hu-73a]. The model considered an oxygen-hydrogen-nitrogen-carbon atmosphere between 60 and 160 km with both molecular and eddy diffusion for the long-lived species including  $\text{CO}_2$ . Photolytic and chemical reactions for  $\text{CO}_2$  were included. Only at the upper boundary was diffusive equilibrium assumed; thus it is worth noting that the calculated  $\text{CO}_2$  densities, at least above 120 km, are essentially identical to the densities calculated on the basis of diffusive equilibrium above 120 km but starting with the calculated  $\text{CO}_2$  density [Hu-73a] at 120 km.

The calculations of Wofsy et al. [WM-72], which extend only to about 120 km, agree with those of Hunt [Hu-73a] (see mixing ratio plot of Fig. 8-1) except below about 100 km where slightly different values of the mixing ratio were used in the two investigations.

The earlier calculations of Hays and Olivero [HO-70] are also shown on Fig. 8-1 on both mixing ratio and density profile plots. The densities have been calculated from the mixing ratio by using the CIRA-65 mean atmosphere model [CI-65]. These calculations yield smaller values than the calculations of Hunt [Hu-73a] for the mixing ratios and  $\text{CO}_2$  densities. The chemical system of Hays and Olivero [HO-70] was restrictive by comparison with that of Hunt [Hu-73a] and according to Hunt [Hu-73a], Hays and Olivero [HO-70] specified O and OH profiles

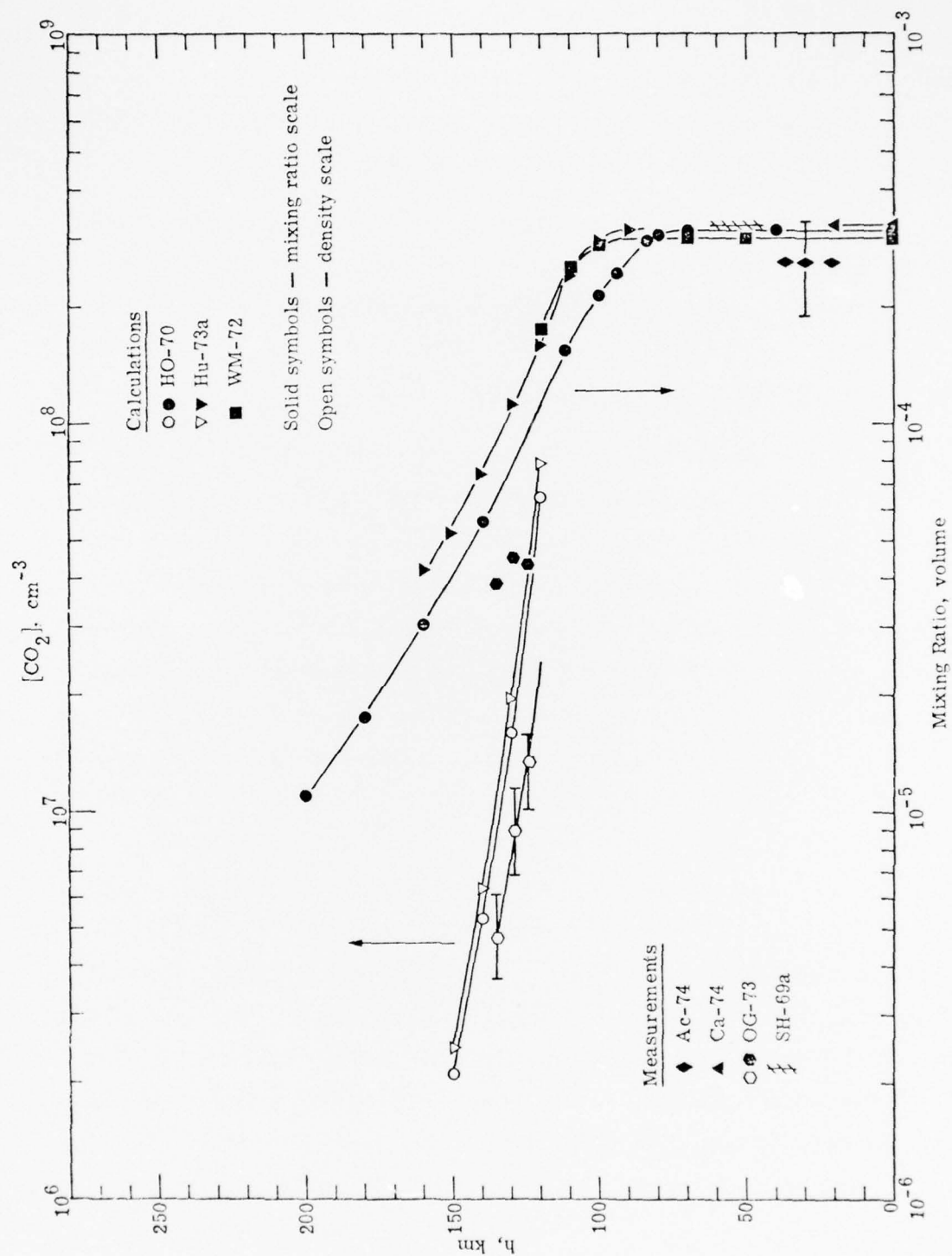


Fig. 8-1. Carbon Dioxide Density and Mixing Ratio Profiles.

rather than calculated them. In addition to the smaller calculated CO<sub>2</sub> densities, the Hays and Olivero [HO-70] calculations predict a departure from mixing above 80 km in contrast to the value of 100 km for the calculations of Hunt [Hu-73a] and Wofsy et al. [WM-72].

The calculations of Hunt [Hu-73a] were made for diurnal conditions. Only a small diurnal variation was reported; thus at 100 km, CO<sub>2</sub> increased by 25% in daytime over the nighttime value.

#### 8.4 SELECTION OF CO<sub>2</sub> PROFILE

By comparing the model calculations and measurements in the density plot of Fig. 8-1 for altitudes above 100 km, one finds the measured CO<sub>2</sub> densities to be significantly smaller than the calculated densities. Both the measurements and calculations indicate diffusive equilibrium above 100 km. The measurements, however, are limited to three specific altitudes, at present. We choose to give equal weight to the measurements [OG-73] and to the model calculation of Hunt [Hu-73a] for 120 km and higher altitudes. Thus we select a CO<sub>2</sub> density of  $5.65 \times 10^7 \text{ cm}^{-3}$  at 120 km and calculate densities at higher altitudes by assuming diffusive equilibrium. At altitudes of 100 km and below, complete mixing is assumed in accordance with the two recent model calculations [Hu-73a, WM-72] and observations below 63 km [SH-69a, Ca-74]; a value of  $3.2 \times 10^{-4}$  is recommended for the mixing ratio. In the interval between 100 and 120 km, values of the CO<sub>2</sub> density are obtained by interpolation as shown on Fig. 8-2. Also shown on Fig. 8-2 are the densities calculated by Hunt [Hu-73a], by use of the ATMOSU program [HS-75], and data of Offermann and Grossmann [OG-73]. The

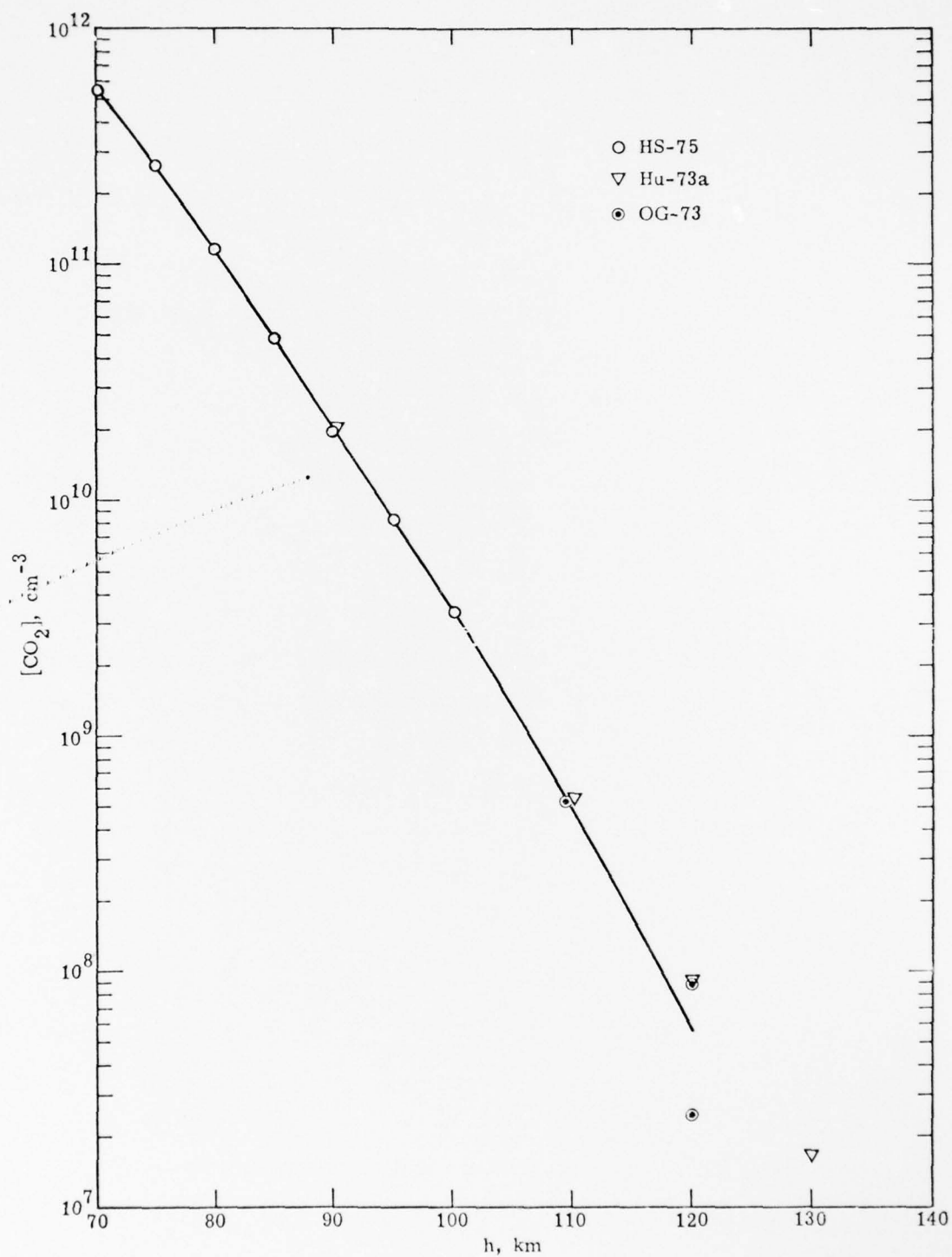


Fig. 8-2. Selection of Carbon Dioxide Densities Between 100 and 120 km by Interpolation.

ATMOSU program [HS-75] uses a mixing ratio of  $3.2 \times 10^{-4}$ . The recommended mixing ratios and  $\text{CO}_2$  densities are summarized in Table 8-1. Any diurnal variation is neglected in the recommended profile.

## 8.5 COMPARISON OF PROFILES

The profile recommended above differs at altitudes of 120 km and greater from a recently proposed profile [SD-73b]. This difference arises as a result of the manner of selecting the density of  $\text{CO}_2$  at 120 km from the data of Offermann and coworkers. In the reports of the German group [OG-73, OP-72] the ratios of the  $\text{CO}_2$  density to the (measured) Ar density were given. The  $\text{CO}_2$  density can be obtained from these ratios by using the measured Ar density as reported in Offermann and Grossmann [OG-73]; this was the procedure used above. However, for the profile of Stephens et al. [SD-73b], the  $\text{CO}_2$  density was obtained by multiplying a value from the curve representing the reported density ratios [OP-72] by the density of Ar as given in CIRA-65;

Table 8-1. Carbon Dioxide Mixing Ratio and Densities.

h, km	Mixing Ratio	$[\text{CO}_2], \text{cm}^{-3*}$
0 to 100	$3.2 \times 10^{-4}$	
105		1.30(9)
110		4.8(8)
115		1.7(8)
120		5.65(7)
> 120	Assume diffusive equilibrium	

\*No diurnal variation; values to be used for noon and midnight.



this procedure yields a  $\text{CO}_2$  density at 120 km 4.5 times larger than the  $\text{CO}_2$  density as obtained above and shown in Fig. 8-1 (i. e., the Ar density in CIRA-65 is about 4.5 times the measured argon density [OG-73]). As a consequence of these considerations, the  $\text{CO}_2$  density used in the recommended profile of Stephens et al. [SD-73b] is too large provided the measured  $\text{CO}_2$  densities [OG-73, OP-72] are accepted as being accurate. The actual difference at 120 km in the  $\text{CO}_2$  profile recommended in the present report and that recommended by Stephens et al. [SD-73b] is smaller than corresponds to the factor of 4.5 as a result of the averaging procedure used here to obtain the recommended density of  $\text{CO}_2$  at 120 km; the ratio of the  $\text{CO}_2$  density at 120 km in the profile of Stephens et al. [SD-73b] to that used here is only 1.9 rather than 4.5.



## 9. DENSITY PROFILE FOR WATER VAPOR

### 9.1 INTRODUCTION

Water density measurements and calculations are presented for altitudes up to 160 km. The experimental measurements are limited to altitudes below about 60 km. For the data of the experiments, there is a considerable variability. The variability is considered by some [Ca-74] to merit further consideration while others [HS-74a] dismiss the higher set of water density values as resulting from water contamination or other errors in the experiments. Continued improvements in the experimental techniques, particularly those based on emission or absorption spectroscopy (which has only recently been extensively employed), are most likely to resolve the different appraisals.

### 9.2 MEASUREMENTS

A discussion of measurements has been given by Cadle [Ca-74] for water vapor at the surface, in the troposphere and in the stratosphere. A profile of water vapor mixing ratios from ground to 16 km prepared by Sissenwine on the basis of radiosonde data [GS-66b] is reported by Cadle [Ca-74] for nominal, midlatitude conditions. This profile is shown on Fig. 9-1. For comparison, measurements of Sissenwine et al. [SG-68a, SG-68b] and an older, midlatitude mean profile by Gutnick [Gu-61] are also shown on Fig. 9-1 over the common altitude range. Note that values of the mixing ratio used here are in parts per million by volume (ppmv) whereas in the literature for water vapor measurements, the mixing ratio is mostly given in parts per million by weight (ppmw). In the present review, the U. S. Standard Atmosphere [US-62] has been used to convert between densities and mixing ratios.

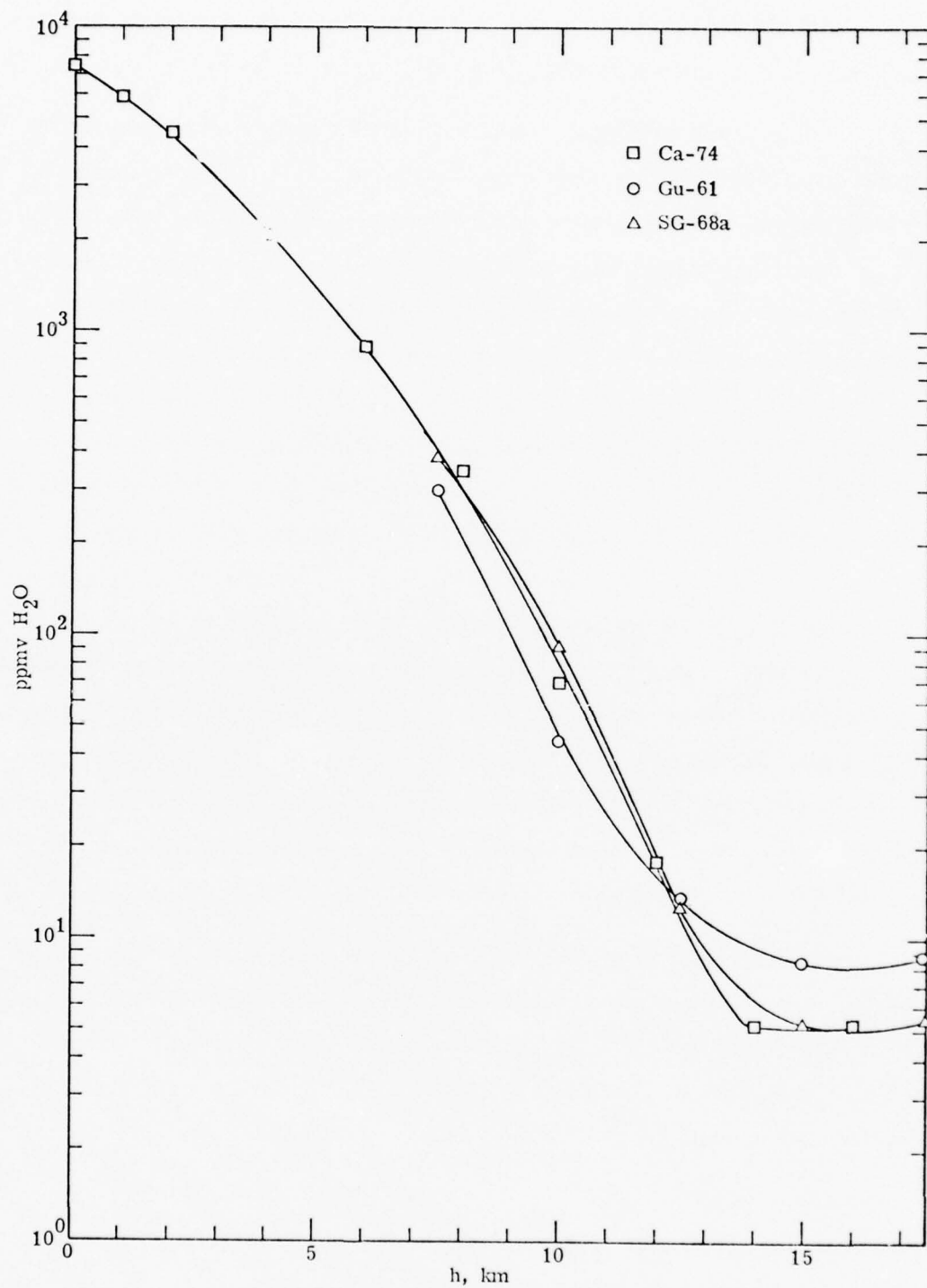


Fig. 9-1. Volume Mixing Ratios for H<sub>2</sub>O Up To 16 km.

The volume mixing ratios for water vapor at altitudes between 10 and 100 km are shown on Fig. 9-2.

The altitude profiles of mixing ratios have been derived from infrared emission and absorption spectra obtained by the University of Denver group on balloon flights [BG-73c, MG-73a, GM-73b] in February and June at midlatitudes. A minimum between 15 and 20 km is found and this is confirmed by comparison of two other optical measurements [Ac-74, Fa-74a]. The measurements of Farmer [Fa-74a] in the altitude range of 14 to 20 km based on the  $\nu_2$  band of water yielded a constant mixing ratio of  $2.4 \pm 0.3$  ppmv with no significant variation over the latitude range between  $30^\circ\text{N}$  and  $80^\circ\text{N}$ . Absorption measurements of Ackerman [Ac-74], also using the  $\nu_2$  band of water, gave a mixing ratio of  $3.4 \pm 0.7$  ppmv in the altitude range between 20 and 37 km. The measurements of Ackerman [Ac-74] are also consistent with a slight and broad maximum between 20 and 30 km. The measurements of Goldman et al. [GM-73b] also indicate a seasonal variation in the mixing ratio with summer values smaller than winter values. Other measurements [MG-73a] by the University of Denver group in India showed a steady decline in mixing ratio between 10 and 26 km; these measurements are not shown on Fig. 9-2.

By means of frost-point temperature measurements, a series of midlatitude measurements have been made by Mastenbrook [Ma-74c, Ma-71c] for altitudes up to 30 km over a period of ten years. These median mixing ratios [Ma-74c] are shown in Fig. 9-2 for altitudes between 16 and 28 km.

Data by Evans [Ev-74a], as reported by Hard [Ha-74] but without any details of the measurements, are plotted on Fig. 9-2, having been converted from densities to mixing ratio values.

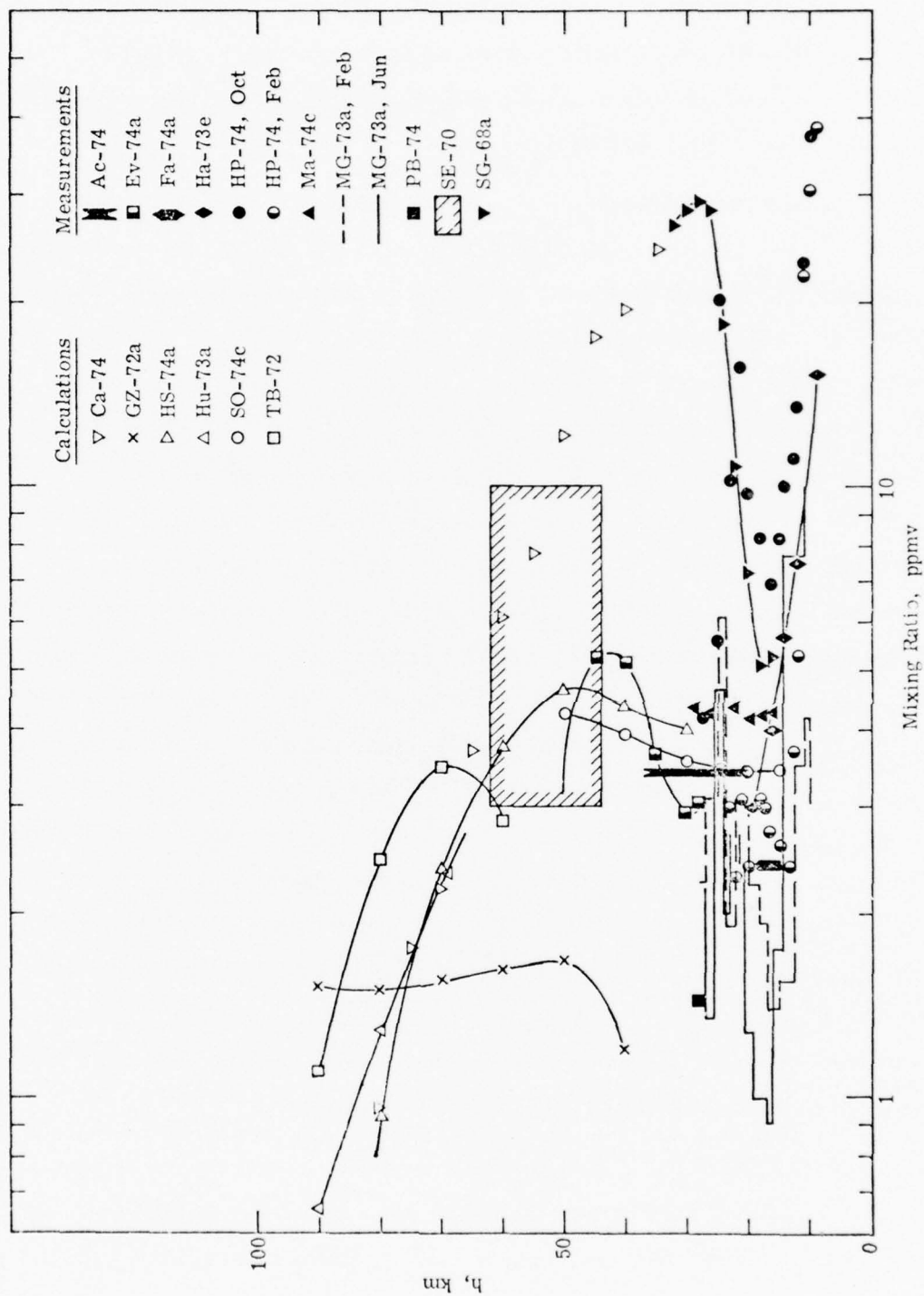


Fig. 9-2. Volume Mixing Ratios for H<sub>2</sub>O Between 10 and 100 km.

A measurement of the water vapor concentration was made at 28 km by use of a spin-flip Raman laser technique [PB-74] as considered also in Section 5.3.1; as can be seen on Fig. 9-2, this measurement indicates a very dry atmosphere.

Emission measurements for water vapor using an infrared radiometer [HP-74] have been made in the southern hemisphere at  $34^{\circ}\text{S}$  as well as  $23^{\circ}\text{S}$ . The October and February measurements at  $34^{\circ}\text{S}$  are shown in Fig. 9-2; the February data are in accord with other measurements, generally, but the October data indicate a wet layer around 20 km. Emission measurements in the sub-millimeter infrared region have been made by Harries [Ha-73e] from aircraft at altitudes between 12 and 16 km over the latitude range between  $50^{\circ}\text{N}$  and  $40^{\circ}\text{S}$ . There is considerably less scatter in these data when the volume mixing ratio is plotted against  $\Delta h$ , the difference in altitude between the measurement height and the tropopause height, than when the data are plotted against the measurement height. The data are shown on Fig. 9-2 as they would appear plotted against  $\Delta h$  but with a tropopause height of 14 km which is near the average of the values, ranging between 11 and 17 km, associated with the measurements. The data also show no clear correlation with latitude. Harries et al. [HS-73b] have also made measurements of the mixing ratio for altitudes above 15.2, 24.3 and 31.8 km from a balloon platform. The average value was found to be 2.7 ppm with no significant difference between the measurements at the three altitudes. These measurements have not been included in the profile of Section 9.4 since the reference [HS-73b] was not available in time.

Sissenwine et al. [SG-68a] have made 17 soundings over northern California up to 32 km using an automatic frost-point instrument on balloon flights. These data are shown on Fig. 9-2 and exhibit significantly



larger mixing ratio values above 20 km than any other measurements shown. In the experiments [SG-68a] care was taken to minimize water contamination, but no quantitative assessment of contamination apparently could be made. The data profile has been extended to 80 km by Cadle [Ca-74] based on a typical temperature found in noctilucent clouds at 80 km. Sissenwine et al. [Ca-74] have considered convective clouds which penetrate the tropopause as a source of the significantly higher water content found above 20 km; McElroy [Ca-74] has emphasized the source of water resulting from oxidation of methane in the stratosphere. Sissenwine et al. [SG-68a] also have considered the passage of water vapor into the stratosphere from lower altitudes during overlapping of, say, the tropical and polar tropopauses. However, no definitive account of the large mixing ratios found by Sissenwine et al. [SG-68a] exists.

From an air sample collected over the altitude range between 44 and 62 km, Scholz et al. [SE-70] have found a range of mixing ratio values from 3 to 10 ppmv. An analysis to distinguish the high altitude water vapor from that desorbed from the sampler surface during analysis, had to be made. The ranges of the mixing ratios and altitudes are shown on Fig. 9-2.

Attempts have been made to determine water vapor densities at altitudes above 100 km. One experiment [OP-72] in which a mass spectrometer was used in the altitude range between 130 and 210 km, was admittedly unsuccessful as a result of water contamination. Measurements of water density in the range from 90 to 180 km are shown by Martynkevich [Ma-72d] which are two to four orders of magnitude larger than values calculated by Martynkevich [Ma-72d]; this excess is attributed to hydrogen and oxygen recombination processes inside the mass analyzer. However, the calculations yielding the lowest water



density are based on data of Goldberg and Blumle [GB-70] who consider their mass 18 data to be entirely due to contamination; if this assignment is correct, the measured water densities of Martynkevich [Ma-72d] could be as much as four to six orders of magnitude higher than calculations (see also Section 9.3). Furthermore, the mass 18 data of Hoffman et al. [HJ-69a] which Martynkevich also uses in calculating water density are attributed by the investigators [HJ-69a] to outgassing from the rocket payload and this is substantiated by satellite measurements [HJ-69a] not subject to outgassing and in which the mass 18 signal is attributed to  $O^{18+}$  with a maximum measured density of  $10^2 \text{ cm}^{-3}$  at about 700 km.

### 9.3 MODEL CALCULATIONS

The results of calculations of water density are collected in Fig. 9-3. The calculations of Hunt [Hu-73a], Thomas and Bowman [TB-72], George et al. [GZ-72a] and Hunten and Strobel [HS-74a] are compared. Between 60 and 80 km, the differences in the calculated water densities are relatively small. Between 80 and 100 km, the differences increase significantly; these changes reflect, in a rough fashion, the relative values and changes with altitude of the eddy diffusion coefficients ( $K$ ) used by the calculators. Thus the smallest values of the eddy diffusion coefficient in the region from 60 to about 95 km were used by Hunten and Strobel [HS-74a] whose calculations yield the smallest water densities above 80 km. The eddy diffusion coefficient profile used by George et al. [GZ-72a] has the largest values of  $K$  at 80 km but the values decline at higher altitudes becoming less than those used by Hunt [Hu-73a] and Thomas and Bowman [TB-72] above about 92 km and less than those used by Hunten and Strobel [HS-74a] above 95 km. However, the importance of eddy diffusion declines at these altitudes and becomes

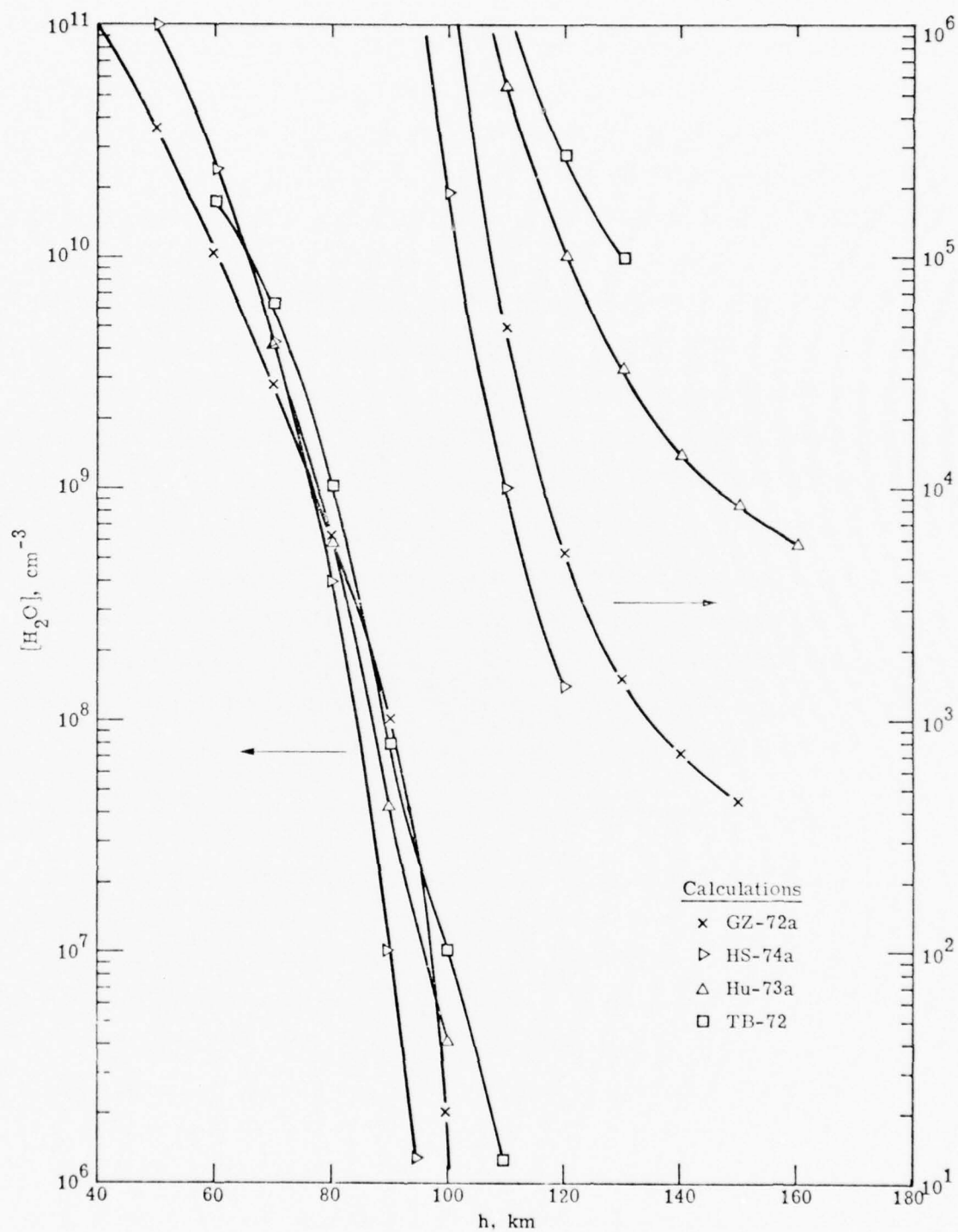


Fig. 9-3. Calculated Water Densities Between 40 and 160 km.

less important than molecular diffusion at altitudes in the vicinity of 100 km. In some of the calculations [GZ-72a, TB-72] the relative importance of eddy diffusion declines rapidly at altitudes between 95 and 105 km whereas a slower decline occurs in others [Hu-73a, HS-74a]. The relative values of water densities established in the four calculations before reaching altitudes slightly above 100 km govern the differences in the water densities found at the highest altitudes of the calculations. Above about 100 km, molecular diffusion and photolysis of water dominate the water profiles; as these processes are similarly treated by the calculators, the four profiles have only small relative changes at these highest altitudes.

The results of the four calculations [GZ-72a, HS-74a, Hu-73a, TB-72] are also shown on Fig. 9-2 for comparison with the experimental data. In addition, calculations of Shimazaki and Ogawa [SO-74c] for altitudes between 15 and 50 km and of Cadle [Ca-74] for the extension of the measurements of Sissenwine et al. [SG-68a] to 80 km are plotted on Fig. 9-2. All calculations are for midlatitudes.

#### 9.4 SELECTION OF WATER PROFILE

Between ground and 16 km, the selected profile is given by the midlatitude mean values assembled by Cadle [Ca-74]; up to 8 km, these values are based on the annual average of radiosonde data for 45°N latitude [GS-66b]; between 10 and 16 km, these values are based on midlatitude,  $\alpha$ -radiation soundings [SG-68a, SG-68b]. The data are plotted in Fig. 9-4 and for altitudes of 4 km and higher; bars show the range of the 1% extremes. The data given by Cadle [Ca-74] have been converted to water densities by using the U. S. Standard Atmosphere [US-62] total densities. See Table 9-1a. Note that the range in density of water vapor at the surface of the earth ranges over five orders of

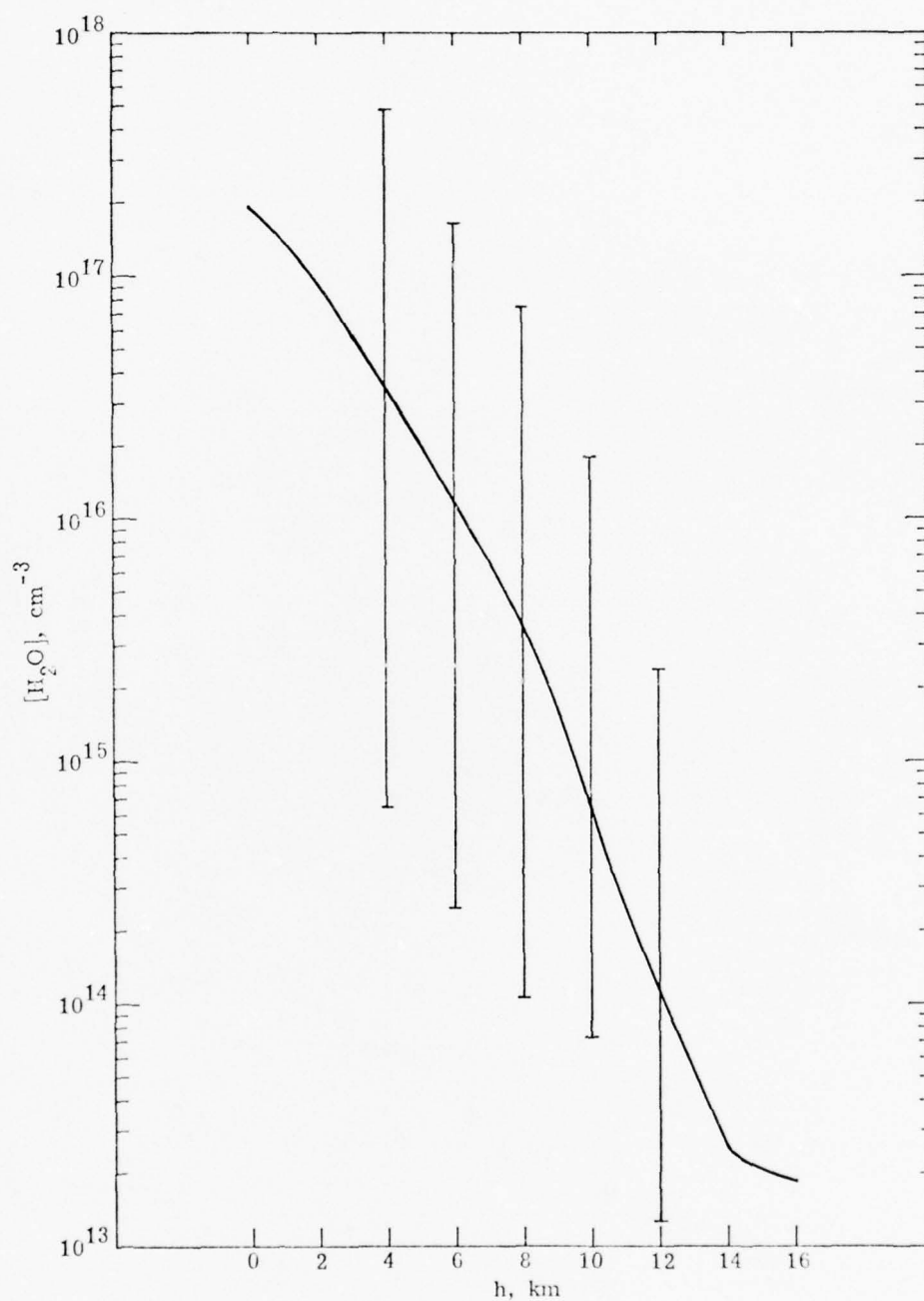


Fig. 9-4. Midlatitude, Tropospheric Water Vapor Densities [Ca-74].

Table 9-1a. Midlatitude Water Vapor Concentrations in the Troposphere.

h, km	ppmw*	$\rho$ , gm/cm <sup>3</sup>	[H <sub>2</sub> O], cm <sup>-3</sup>	h, km	ppmw*	$\rho$ , gm/cm <sup>3</sup>	[H <sub>2</sub> O], cm <sup>-3</sup>
0	4686	2.55(19)	1.91(17)	8	216	1.09(19)	3.78(15)
1	3700	2.31(19)	1.37(17)	10	43.2	8.60(18)	5.93(14)
2	2843	2.09(19)	9.52(16)	12	11.3	6.49(18)	1.17(14)
4	1268	1.70(19)	3.46(16)	14	3.3	4.74(18)	2.51(13)
6	554	1.37(19)	1.22(16)	16	3.3	3.46(18)	1.83(13)

\*Ca-74.

†  $\rho$  total density from U. S. Standard Atmosphere [US-62].

Table 9-1b. Average of Measured Values of Water Mixing Ratios Between 15 and 50 km.

h, km	MG-73a		Mixing Ratio, ppmv						$\rho$ , gm/cm <sup>3</sup>	[H <sub>2</sub> O], cm <sup>-3</sup>
	Feb	June	HP-74	Ma-74c	Ac-74	Fa-74a	Ev-74a	Ha-73e <sup>†</sup>		
15	1.76	1.55	2.4			2.4		5.2 Aug 4.39 Feb	4.05(18)	1.22(13)
20	2.65*	1.85*	2.4	4.2	3.4	2.4			1.85(18)	5.18(12)
25	4.6 <sup>x</sup>	3.0 <sup>x</sup>		4.25	3.4				8.33(17)	3.17(12)
30					3.4		2.95		3.83(17)	1.22(12)
35					3.4		3.65		1.76(17)	6.16(11)
40							5.15		8.31(16)	4.28(11)
45							5.25		4.09(15)	2.14(11)

\*Average of values over the range 19 to 21 km.

<sup>x</sup> Average of values over the range 24 to 27 km.<sup>†</sup> These values read from HP-74.



magnitude and that although the surface density generally decreases with increase in latitude, there are variations due to local sources and sinks of water vapor [Ca-74].

The majority of experimental results of Fig. 9-2 lie between 15 and 50 km; between these altitudes there is a nominal range in mixing ratio between 1 and 30 ppmv. To derive a nominal profile, the experimental data in the altitude range between 15 and 45 km were averaged excluding the very high ratios of Sissenwine et al. [SG-68a] and the "wet layer" data of Hysen and Platt [HP-74] identified on Fig. 9-2 by the filled circles. The data and the averages are given on Table 9-1b.

Between 60 and 80 km an average of the calculated densities was used in the selected profile. Above 100 km, an average of the calculated densities of Hunten and Strobel [HS-74a] and George et al. [GZ-72a] was used in the selected profile on the basis of the arguments of Hunten and Strobel [HS-74a] for lower values of the eddy diffusion coefficient (in the region above 80 km). Thus the calculations of Hunt [Hu-73a] and Thomas and Bowman [TB-72] are excluded. At altitudes between 45 and 60 km and between 80 and 100 km, densities were chosen by interpolation. At altitudes above 120 km, an exponential decline in water density was assumed. Table 9-2 and Fig. 9-5 show the selected data. No diurnal variation was included as the calculations [Hu-73a, TB-72] show no significant variation.



Table 9-2. Water Vapor Densities.

h, km	[H <sub>2</sub> O], cm <sup>-3</sup>	h, km	[H <sub>2</sub> O], cm <sup>-3</sup>
0	1.9(17)	65	9.2(9)
5	2.1(16)	70	4.4(9)
10	6.0(14)	75	1.8(9)
15	1.2(13)	80	6.5(8)
20	5.2(12)	85	2.0(8)
25	3.2(12)	90	4.9(7)
30	1.2(12)	95	8.4(6)
35	6.2(11)	100	1.1(6)
40	4.3(11)	105	1.3(5)
45	2.1(11)	110	2.5(4)
50	8.4(10)	115	8.7(3)
55	3.6(10)	120	3.3(3)
60	1.7(10)	> 120	†

† Above 120 km  $[\text{H}_2\text{O}] = [\text{H}_2\text{O}]_{120} e^{-0.166(h-120)}$

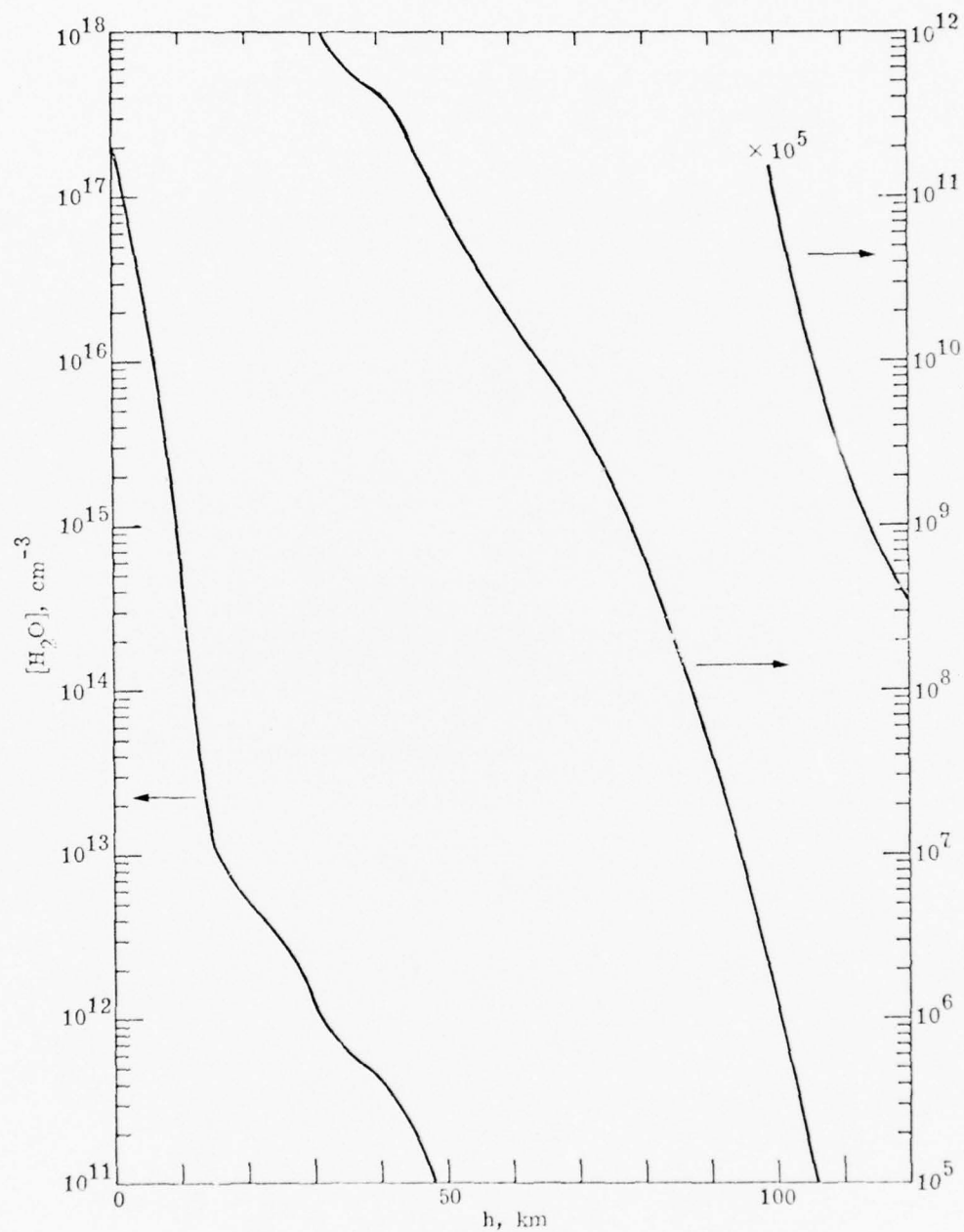


Fig. 9-5. Water Vapor Profile.

## REFERENCES

- Ac-74 M. Ackerman, Stratospheric Water Vapor from High Resolution Infrared Spectra, Planet. Space Sci. 22, 1265 (1974).
- AF-73 M. Ackerman, D. Frimont, C. Muller, D. Nevejans, J. -C. Fontanella, A. Girard and N. Louisnard, Stratospheric Nitric Oxide from Infrared Spectra, Nature 245, 205 (1973).
- AF-73a M. Ackerman, J. C. Fontanella, D. Frimont, A. Girard, R. Gramont, N. Louisnard, C. Muller, and D. Nevejans, Recent Stratospheric Spectra of NO and NO<sub>2</sub>, Aeronomica Acta A-120, (1973).
- AF-74 M. Ackerman, D. Frimont, C. Muller, D. Nevejans, J. C. Fontanella, A. Girard, L. Gramont, and N. Louisnard, Recent Stratospheric Spectra of NO and NO<sub>2</sub>, Can. J. Chem. 52, 1532 (1974).
- AM-72 M. Ackerman and C. Muller, Stratospheric Nitrogen Dioxide from Infrared Spectra, Nature 240, 300 (1972).
- AM-73 M. Ackerman and C. Muller, Stratospheric Methane and Nitrogen Dioxide from Infrared Spectra, Pure and Appl. Geophys. 106-108, 1325 (1973).
- Ba-66c C. A. Barth, Nitric Oxide in the Upper Atmosphere, Ann. Geophys. 22, 198 (1966).
- Ba-66d C. A. Barth, Rocket Measurement of Nitric Oxide in the Upper Atmosphere, Planet. Space Sci. 14, 623 (1966).
- Ba-72a A. E. Barrington, Ed., Climatic Impact Assessment Program, Proceedings of the Survey Conference, 15-16 February 1972, DOT-TSC-OST-72-13, September 1972.
- BB-72c R. K. Bishop, K. D. Baker, and R. Y. Han, Altitude Profile of O<sub>2</sub> (<sup>1</sup>Δ<sub>g</sub>) at Night, J. Atmos. Terr. Phys. 34, 1477 (1972).

- BB-74 V. N. Balabanova, K. D. Bychkova, and V. P. Matrynenko, The Atomic Nitrogen Amount in the Upper Atmosphere According to Measurement of the Ethylene Luminous Cloud Brightness, J. Atmos. Terr. Phys. 36, 1785 (1974).
- BG-73c J. N. Brooks, A. Goldman, J. J. Kusters, D. G. Murcray, F. H. Murcray, and W. J. Williams, Balloon-Borne Infrared Measurements, pp. 278-285 in Physics and Chemistry of Upper Atmospheres, ed. by B. M. McCormac, D. Reidel Publishing Co., 1973.
- BM-73a A. W. Brewer, C. T. McElroy, and J. B. Kerr, Nitrogen Dioxide Concentrations in the Atmosphere, Nature 246, 129 (1973).
- BN-73 G. Brasseur and M. Nicolet, Chemospheric Processes of Nitric Oxide in the Mesosphere and Stratosphere, Planet. Space Sci. 21, 939 (1973).
- Ca-74 R. D. Cadle, Convener, Report of Task Group V, U. S. Committee on Extension to the Standard Atmosphere Trace Constituents, May 1974 (draft copy).
- CH-66a J. H. Carver, B. H. Horton, and F. G. Burger, Natural Ozone Distribution in the Upper Atmosphere, J. Geophys. Res. 71, 4189 (1966).
- Ch-70b K. S. W. Champion, Variations with Season and Latitude of Density, Temperature and Composition in the Lower Thermosphere, Space Research X, 450 (1970).
- CH-72 J. H. Carver, B. H. Horton, R. S. O'Brien, and B. Rofe, Ozone Determinations by Lunar Rocket Photometry, Planet. Space Sci. 20, 217 (1972).
- CI-65 CIRA 1965, COSPAR International Reference Atmosphere 1965, North-Holland Publishing Co., Amsterdam, 1965.
- CI-72 CIRA-1972, COSPAR International Reference Atmosphere, 1972, Compiled by COSPAR Working Group A, Akademie-Verlag, Berlin, 1972.

- CJ-71 P. J. Crutzen, I. T. N. Jones, and R. P. Wayne, Calculation of  $[O_2(^1\Delta_g)]$  in the Atmosphere Using New Laboratory Data, J. Geophys. Res. 76, 1490 (1971).
- Cr-71 P. J. Crutzen, Ozone Production Rates in an Oxygen-Hydrogen-Nitrogen Oxide Atmosphere, J. Geophys. Res. 76, 7311 (1971).
- Cr-74a P. Crutzen, A Review of Upper Atmospheric Photochemistry, Can. J. Chem. 52, 1569 (1974).
- CS-74a S. Chandra and A. K. Sinha, The Role of Eddy Turbulence in the Development of Self-Consistent Models of the Lower and Upper Thermosphere, J. Geophys. Res. 79, 1916 (1974).
- Da-72d A. D. Danilov, Diurnal Variations of Atmospheric Neutral Composition at Altitudes of 130-200 km, Space Research XII, 891 (1972).
- Da-72e A. D. Danilov, Ion Composition and Photochemistry of the E Region, Space Research XII, 1299 (1972).
- DB-74a P. H. G. Dickinson, R. C. Bolden, and R. A. Young, Measurement of Atomic Oxygen in the Lower Ionosphere Using a Rocket-Borne Resonance Lamp, Nature 252, 289 (1974).
- DG-73 T. M. Donahue, B. Guenther, and R. J. Thomas, Distribution of Atomic Oxygen in the Upper Atmosphere Deduced from Ogo 6 Airglow Observations, J. Geophys. Res. 78, 6662 (1973).
- DG-74 T. M. Donahue, B. Guenther, and R. J. Thomas, Spatial and Temporal Behavior of Atomic Oxygen Determined by Ogo 6 Airglow Observations, J. Geophys. Res. 79, 1959 (1974).
- Do-74 T. M. Donahue, An Upper Limit to the Product of NO and O Densities from 105 to 120 km, J. Geophys. Res. 79, 4337 (1974).
- Du-70a H. U. Dütsch, Atmospheric Ozone — A Brief Review, J. Geophys. Res. 75, 1707 (1970).



- Du-71 H. U. Dütsch, Photochemistry of Atmospheric Ozone, pp. 219-322 in Advances in Geophysics, Vol. 15, edited by H. E. Landsberg and J. Van Mieghem, Academic Press, 1971.
- Du-74 H. U. Dütsch, The Ozone Distribution in the Atmosphere, Can. J. Chem. 52, 1491 (1974).
- EH-68 W. F. J. Evans, D. M. Hunten, E. J. Llewellyn, and A. Vallance Jones, Altitude Profiles of the Infrared Atmospheric System of Oxygen in the Dayglow, J. Geophys. Res. 73, 2885 (1968).
- EL-67 W. F. J. Evans, E. J. Llewellyn and A. Vallance Jones, Balloon-Borne Observations of the (0,0) Band of the ( $1\Delta_g-3\Sigma_g^-$ ) System of Oxygen in the Day and Twilight Glow, Nature 213, 352 (1967).
- EL-69 W. F. J. Evans, E. J. Llewellyn, and A. Vallance Jones, Balloon Observations of the Temporal Variation of the Infrared Atmospheric Oxygen Bands in the Airglow, Planet. Space Sci. 17, 933 (1969).
- EL-70a W. F. J. Evans and E. J. Llewellyn, Molecular Oxygen Emissions in the Airglow, Ann. Geophys. 26, 167 (1970).
- EL-72a W. F. J. Evans and E. J. Llewellyn, Measurements of Mesospheric Ozone from Observations of the  $1.27\ \mu$  Band, Radio Sci. 7, 45 (1972).
- EL-72b W. F. J. Evans, E. J. Llewellyn, and A. Vallance Jones, Altitude Distribution of the  $O_2$  ( $1\Delta$ ) Nightglow Emission, J. Geophys. Res. 77, 4899 (1972).
- Ev-74a W. F. J. Evans, Rocket Measurements of Water Vapor in the Stratosphere, draft manuscript, Atmospheric Environment Service, 4905 Dufferin St., Downsview, ONT, M3H 5T4, 1974 (referenced in Ha-74).
- EW-70 W. F. J. Evans, H. C. Wood, and E. J. Llewellyn, Ground-Based Photometric Observations of the  $1.27\ \mu$  Band of  $O_2$  in the Twilight Airglow, Planet. Space Sci. 18, 1065 (1970).
- Fa-74a C. B. Farmer, Infrared Measurements of Stratospheric Composition, Can. J. Chem. 52, 1544 (1974).



- FG-74 J. C. Fontanella, A. Girard, L. Gramont, and N. Louisnard, Vertical Distribution of NO, NO<sub>2</sub> and HNO<sub>3</sub> as Derived from Stratospheric Absorption Infrared Spectra, Proc. Third Conference on CIAP, in press, 1974.
- FT-74 P. D. Feldman and P. Z. Takacs, Nitric Oxide Gamma and Delta Band Emission at Twilight, Geophys. Res. Letters 1, 169 (1974).
- GB-70 R. A. Goldberg and L. J. Blumle, Positive Ion Composition from a Rocket-Borne Mass Spectrometer, J. Geophys. Res. 75, 133 (1970).
- GG-72 D. Golomb and R. E. Good, Atomic Oxygen Profiles over Churchill and Hawaii from Chemical Releases, Space Research XII, 675 (1972).
- GH-68a S. N. Ghosh, B. B. Hinton, L. M. Jones, R. J. Leite, C. J. Mason, E. J. Schaefer, and M. Walters, Atomic Nitrogen in the Upper Atmosphere Measured by Mass Spectrometers, J. Geophys. Res. 73, 4425 (1968).
- GM-70c A. Goldman, D. G. Murcray, F. H. Murcray, W. J. Williams, and F. S. Bonomo, Identification of the  $\nu_3$  NO<sub>2</sub> Band in the Solar Spectrum Observed from a Balloon-Borne Spectrometer, Nature 225, 443 (1970).
- GM-73b A. Goldman, D. G. Murcray, F. H. Murcray, W. J. Williams, and J. N. Brooks, Distribution of Water Vapor as Determined from Balloon Measurements of Atmospheric Emission Spectra in the 24-29  $\mu$ m Region, Appl. Opt. 12, 1045 (1973).
- GS-66b I. I. Gringorten, H. A. Salmela, I. Solomon, and J. Sharp, Major USAF (1966) Atmospheric Humidity Atlas — Northern Hemisphere, Air Force Surveys in Geophysics, No. 186, AFCRL-66-621 (1966).
- GS-75a N. Golshan and C. F. Sechrist, Jr., Seasonal and Solar Cycle Variation of E-Region Nitric Oxide, Radio Sci. 10, 305 (1975).
- Gu-61 M. Gutnick, How Dry the Sky, J. Geophys. Res. 66, 2867 (1961).

- GZ-72a J. D. George, S. P. Zimmerman, and T. J. Keneshea, The Latitudinal Variation of Major and Minor Neutral Species in the Upper Atmosphere, Space Research XII, 696 (1972).
- Ha-73e J. E. Harries, Measurement of Some Hydrogen-Oxygen-Nitrogen Compounds in the Stratosphere from Concorde 002, Nature 241, 515 (1973).
- Ha-74 T. M. Hard, Letter to CIAP Distribution (Charts of Stratospheric Trace-Gas Profiles), U. S. Dept. of Transportation, Kendall Square, Cambridge, Mass. 02142, May 30, 1974.
- He-71 W. R. Henderson, D-Region Atomic Oxygen Measurement, J. Geophys. Res. 76, 3166 (1971).
- He-74a W. R. Henderson, Atomic Oxygen Profile Measurements, J. Geophys. Res. 79, 3819 (1974).
- Hi-71a E. Hilsenrath, Ozone Measurements in the Mesosphere and Stratosphere During Two Significant Geophysical Events, J. Atmos. Sci. 28, 295 (1971).
- HJ-69a J. H. Hoffman, C. Y. Johnson, J. C. Holmes, and J. M. Young, Daytime Midlatitude Ion Composition Measurements, J. Geophys. Res. 74, 6281 (1969).
- HM-69c J. C. Haslett, L. R. Megill, and H. I. Schiff, Rocket Measurements of  $O_2(^1\Delta_g)$ , Can. J. Phys. 47, 2351 (1969).
- HM-73g R. Y. Han, L. R. Megill, and C. L. Wyatt, Rocket Observation of the Equatorial  $O_2(^1\Delta_g)$  Emission after Sunset, J. Geophys. Res. 78, 6140 (1973).
- HN-72a D. R. Hickman and A. O. Nier, Measurement of the Neutral Composition of the Lower Thermosphere Above Fort Churchill by Rocket-Borne Mass Spectrometer, J. Geophys. Res. 77, 2880 (1972).
- HO-70 P. B. Hays and J. J. Olivero, Carbon Dioxide and Monoxide Above the Troposphere, Planet. Space Sci. 18, 1729 (1970).
- HP-74 P. Hyson and C. M. R. Platt, Radiometric Measurements of Stratospheric Water Vapor in the Southern Hemisphere, J. Geophys. Res. 79, 5001 (1974).

- HR-72a P. B. Hays, R. G. Roble, and A. N. Shah, Terrestrial Atmospheric Composition from Stellar Occultations, *Science* **176**, 793 (1972).
- HR-73 P. B. Hays and R. G. Roble, Observations of Mesospheric Ozone at Low Latitudes, *Planet. Space Sci.* **21**, 273 (1973).
- HS-73b J. E. Harries, N. R. Swann, G. P. Carruthers, and G. A. Robinson, Measurements of the Sub-Millimetre Stratospheric Emission Spectrum from a Balloon Platform, *Infrared Phys.* **13**, 149 (1973).
- HS-74a D. M. Hunten and D. F. Strobel, Production and Escape of Terrestrial Hydrogen, *J. Atmos. Sci.* **31**, 305 (1974).
- HS-75 D. A. Hamlin and M. R. Schoonover, Ambient Atmosphere (Major and Minor Neutral Species and Ionosphere) [Model 1], Vol. 2A of Atmospheric, Geomagnetic, and High-Altitude Energy-Deposition and Neutral-Particle-Motion Models for RC JOE, Science Applications, Inc. Report No. SAI-75-609-LJ, 13 June 1975. Also published as Vol. 14a of this manual.
- Hu-73a B. G. Hunt, A Generalized Aeronomic Model of the Mesosphere and Lower Thermosphere Including Ionospheric Processes, *J. Atmos. Terr. Phys.* **35**, 1755 (1973).
- Ja-71c L. G. Jacchia, Revised Static Models of the Thermosphere and Exosphere with Empirical Temperature Profiles, Smithsonian Astrophysical Observatory Special Report 332, 5 May 1971.
- KB-74c V. V. Koshelev and S. I. Belinskaya, Upon Estimation of Effective Concentration of Neutral Atmosphere Minor Constituents NO and N on the Basis of Experimental Values  $[NO^+]/[O_2^+]$ , *J. Atmos. Terr. Phys.* **36**, 315 (1974).
- Kr-70a V. A. Krasnopoly'skiy, Nitrogen Oxide at Heights of 100-220 km, According to Cosmos-224 Data, *Geomag. & Aeron.* **10**, 660 (1970).
- Le-72a H. Levy II, Photochemistry of the Lower Troposphere, *Planet. Space Sci.* **20**, 919 (1972).
- Le-73 H. Levy, II, Photochemistry of Minor Constituents in the Troposphere, *Planet. Space Sci.* **21**, 575 (1973).

- Ma-71c H. J. Mastenbrook, The Variability of Water Vapor in the Stratosphere, J. Atmos. Sci. 28, 1495 (1971).
- Ma-72d G. M. Martynkevich, H<sub>2</sub>O<sup>+</sup> Ions and H<sub>2</sub>O Molecules in the Lower Thermosphere and Ionosphere, Space Research XII, 1311 (1972).
- Ma-74c H. J. Mastenbrook, Water-Vapor Measurements in the Lower Stratosphere, Can. J. Chem. 52, 1527 (1974).
- MB-72b G. M. Martynkevich and E. D. Byuro, Atomic Nitrogen in the Lower Thermosphere in the Period of Rising Solar Activity, Space Research XII, 691 (1972).
- Me-71 L. G. Meira, Jr., Rocket Measurements of Upper Atmospheric Nitric Oxide and Their Consequences to the Lower Ionosphere, J. Geophys. Res. 76, 202 (1971).
- MG-73a D. G. Murcray, A. Goldman, F. H. Murcray, W. J. Williams, J. N. Brooks, and D. B. Barker, Vertical Distribution of Minor Atmospheric Constituents as Derived from Air-Borne Measurements of Atmospheric Emission and Absorption Infrared Spectra, presented at AIAA 11th Aerospace Sciences Meeting held 10-12 January 1973, at Washington, D. C., AIAA Paper No. 73-103 (1973).
- MH-70b L. R. Megill, J. C. Haslett, H. I. Schiff, and G. W. Adams, Observations of O<sub>2</sub>(<sup>1</sup>Δ<sub>g</sub>) in the Atmosphere and Allowable Values of the Eddy Diffusion Coefficient, J. Geophys. Res. 75, 6398 (1970).
- MK-68b D. G. Murcray, T. G. Kyle, F. H. Murcray, and W. G. Williams, Nitric Acid and Nitric Oxide in the Lower Stratosphere, Nature 218, 78 (1968).
- MM-69 D. G. Murcray, F. H. Murcray, W. J. Williams, T. G. Kyle, and A. Goldman, Variation of the Infrared Solar Spectrum Between 700 cm<sup>-1</sup> and 2240 cm<sup>-1</sup> with Altitude, Appl. Opt. 8, 2519 (1969).
- MM-73b J. C. McConnell and M. B. McElroy, Odd Nitrogen in the Atmosphere, J. Atmos. Sci. 30, 1465 (1973).



- Mo-73 K. Moe, Density and Composition of the Lower Thermosphere, J. Geophys. Res. 78, 1633 (1973).
- MR-73 D. E. Miller and P. Ryder, Measurement of the Ozone Concentration from 55 to 95 km at Sunset, Planet. Space Sci. 21, 963 (1973).
- MR-74b A. P. Mitra and J. N. Rowe, Ionospheric Constraints of Mesospheric Nitric Oxide, J. Atmos. Terr. Phys. 36, 1797 (1974).
- MS-75a P. E. Monro and L. G. Smith, Determination of Nitric Oxide Concentrations from Sunrise E-Region Electron Density Measurements, Radio Sci. 10, 317 (1975).
- Ni-70 M. Nicolet, The Origin of Nitric Oxide in the Terrestrial Atmosphere, Planet. Space Sci. 18, 1111 (1970).
- Ni-71a M. Nicolet, Aeronomic Reactions of Hydrogen and Ozone, in Mesospheric Models and Related Experiments, ed. by G. Fiocco, D. Reidel Publishing Co., p. 1, 1971.
- Ni-72b M. Nicolet, Aeronomic Chemistry of the Stratosphere, Climatic Impact Assessment Program, Proceedings of the Survey Conference, 15-16 February 1972, A. E. Barrington, editor, DOT-TSC-OST-72-13, September 1972.
- Ni-74 M. Nicolet, An Overview of Aeronomic Processes in the Stratosphere and Mesosphere, Can. J. Chem. 52, 1381 (1974).
- NP-72a R. S. Narcisi, C. R. Philbrick, J. C. Ulwick, and M. E. Gardner, Mesospheric Nitric Oxide Concentrations During a PCA, J. Geophys. Res. 77, 1332 (1972).
- NS-73 H. B. Niemann, N. W. Spencer, and G. A. Schmitt, A Thermosphere Composition Measurement Using a Quadrupole Mass Spectrometer with a Side Energy Focusing Quasi-Open Ion Source, J. Geophys. Res. 78, 2265 (1973).
- OD-73a D. Offermann and A. Drescher, Atomic Oxygen Densities in the Lower Thermosphere as Derived from In Situ 5577-A Night Airglow and Mass Spectrometer Measurements, J. Geophys. Res. 78, 6690 (1973).

- Of-74 D. Offermann, Composition Variations in the Lower Thermosphere, J. Geophys. Res. 79, 4281 (1974).
- OG-73 D. Offermann and K. U. Grossmann, Thermospheric Density and Composition as Determined by a Mass Spectrometer with Cryo Ion Source, J. Geophys. Res. 78, 8296 (1973).
- OJ-74 E. S. Oran, P. S. Julienne, and D. F. Strobel, The Aeronomy of Odd Nitrogen in the Thermosphere, NRL Memorandum Report 2963, December 1974.
- Ol-74a W. L. Oliver, Determination of Nitric Oxide Concentrations from Eclipse Variations of Ion Concentrations, J. Atmos. Terr. Phys. 36, 801 (1974).
- OP-72 D. Offermann, K. Pelka, and U. von Zahn, Mass Spectrometric Measurements of Minor Constituents in the Lower Thermosphere, Int. J. Mass Spectrom. Ion Phys. 8, 391 (1972).
- OZ-71 D. Offermann and U. von Zahn, Atomic Oxygen and Carbon Dioxide in the Lower Thermosphere, J. Geophys. Res. 76, 2520 (1971).
- PB-74 C. K. N. Patel, E. G. Burkhardt, and C. A. Lambert, Spectroscopic Measurements of Stratospheric Nitric-Oxide and Water Vapor, Science 184, 1173 (1974).
- Pe-69a J. B. Pearce, Rocket Measurement of Nitric Oxide Between 60 and 96 Kilometers, J. Geophys. Res. 74, 853 (1969).
- PL-74a J. H. Park and J. London, Ozone Photochemistry and Radiative Heating of the Middle Atmosphere, J. Atmos. Sci. 31, 1898 (1974).
- Po-72a A. A. Pokhunkov, Mass-Spectrometric Investigations of Upper Atmosphere Neutral Composition at Equatorial, Middle and Polar Latitudes, Space Research XII, 658 (1972).
- Re-68c E. I. Reed, A Night Measurement of Mesospheric Ozone by Observations of Ultraviolet Airglow, J. Geophys. Res. 73, 2951 (1968).



- RM-63 R. D. Rawcliffe, G. E. Meloy, R. M. Friedman, and E. H. Rogers, Measurement of Vertical Distribution of Ozone from a Polar Orbiting Satellite, J. Geophys. Res. 68, 6425 (1963).
- RM-73 J. W. Rogers, R. E. Murphy, A. T. Stair, Jr., J. C. Ulwick, K. D. Baker, and L. L. Jensen, Rocket-Borne Radiometric Measurements of OH in the Auroral Zone, J. Geophys. Res. 78, 7023 (1973).
- RN-72a R. G. Roble and R. B. Norton, Thermospheric Molecular Oxygen from Solar Extreme-Ultraviolet Occultation Measurements, J. Geophys. Res. 77, 3524 (1972).
- RS-73d B. A. Ridley, H. I. Schiff, A. W. Shaw, L. Bates, C. Howlett, H. LeVaux, and L. R. Megill, Measurements in situ of Nitric Oxide in the Stratosphere between 17.4 and 22.9 km, Nature 245, 310 (1973).
- Ru-73a D. W. Rusch, Satellite Ultraviolet Measurements of Nitric Oxide Fluorescence with a Diffusive Transport Model, J. Geophys. Res. 78, 5676 (1973).
- Sc-74a G. Scialom, Neutral Composition in the Lower Thermosphere, Radio Sci. 9, 253 (1974).
- Sc-74b H. I. Schiff, Measurements of NO, NO<sub>2</sub> and HNO<sub>3</sub> in the Stratosphere, Can. J. Chem. 52, 1536 (1974).
- SD-73b This reference supplied upon approval from the Contracting Officer, Contract DNA001-74-C-0182, Defense Nuclear Agency, Washington, D. C. 20305.
- SE-70 T. G. Scholz, D. H. Ehkalt, L. E. Heidt, and E. A. Martell, Water Vapor, Molecular Hydrogen, Methane and Tritium Concentrations Near the Stratosphere, J. Geophys. Res. 75, 3049 (1970).
- SG-68a N. Sissenwine, D. D. Grantham, and H. A. Salmela, Mid-Latitude Humidity Up to 32 km, J. Atmos. Sci. 25, 1129 (1968).
- SG-68b N. Sissenwine, D. D. Grantham, H. A. Salmela, Humidity Up to the Mesopause, AFCRL-68-0550, 1968.

- SH-69a T. G. Scholz, L. E. Heidt, E. A. Martell, and D. H. Ekhalt, Water Vapor and Trace Gases Near the Stratosphere, Trans. A. G. U. 50, 176 (1969).
- SH-70 D. F. Strobel, D. M. Hunten, and M. B. McElroy, Production and Diffusion of Nitric Oxide, J. Geophys. Res. 75, 4307 (1970).
- SL-70a T. Shimazaki and A. R. Laird, A Model Calculation of the Diurnal Variation in Minor Neutral Constituents in the Mesosphere and Lower Thermosphere Including Transport Effects, J. Geophys. Res. 75, 3221 (1970).
- SL-72 T. Shimazaki and A. R. Laird, Correction to 'A Model Calculation of the Diurnal Variation in Minor Neutral Constituents in the Mesosphere and Lower Thermosphere Including Transport Effects', J. Geophys. Res. 77, 276 (1972).
- SL-72a T. Shimazaki and A. R. Laird, Seasonal Effects on Distributions of Minor Neutral Constituents in the Mesosphere and Lower Thermosphere, Radio Sci. 7, 23 (1972).
- SM-70 D. F. Strobel and M. B. McElroy, The F2-Layer at Middle Latitudes, Planet. Space Sci. 18, 1181 (1970).
- SO-74 T. Shimazaki and T. Ogawa, A Theoretical Model of Minor Constituent Distributions in the Stratosphere Including Diurnal Variations, J. Geophys. Res. 79, 3411 (1974).
- SO-74b T. G. Scholz and D. Offermann, Measurement of Neutral Atmospheric Composition at 85-115 km by Mass Spectrometer with Cryoion Source, J. Geophys. Res. 79, 307 (1974).
- SO-74c T. Shimazaki and T. Ogawa, On the Theoretical Model of Vertical Distributions of Minor Neutral Constituents Concentrations in the Stratosphere, NOAA Technical Memorandum ERL OD-20, May 1974.
- St-71 D. F. Strobel, Diurnal Variation of Nitric Oxide in the Upper Atmosphere, J. Geophys. Res. 76, 2441 (1971).
- St-71d D. F. Strobel, Odd Nitrogen in the Mesosphere, J. Geophys. Res. 76, 8384 (1971).
- St-72 D. F. Strobel, Nitric Oxide in the D Region, J. Geophys. Res. 77, 1337 (1972).

- St-72a D. F. Strobel, Minor Neutral Constituents in the Mesosphere and Lower Thermosphere, Radio Sci. 7, 1 (1972).
- SU-74 A. T. Stair, Jr., J. C. Ulwick, D. J. Baker, C. L. Wyatt, and K. D. Baker, Altitude Profiles of Infrared Radiance of O<sub>3</sub>(9.6  $\mu$ m) and CO<sub>2</sub>(15  $\mu$ m), Geophys. Res. Letters 1, 117 (1974).
- TB-72 L. Thomas and M. R. Bowman, The Diurnal Variations of Hydrogen and Oxygen Constituents in the Mesosphere and Lower Thermosphere, J. Atmos. Terr. Phys. 34, 1843 (1972).
- TF-73 R. A. Toth, C. B. Farmer, R. A. Schindler, O. F. Raper, P. W. Schaper, Detection of Nitric Oxide in the Lower Atmosphere, Nature Phys. Sci. 244, 7 (1973).
- Th-71a L. Thomas, Oxygen, Hydrogen and Nitrogen Constituents in the Mesosphere and Ionization Processes, p. 65 in Mesospheric Models and Related Experiments, ed. by G. Fiocco, D. Reidel, 1971.
- Ti-73 G. C. Tisone, Measurements of NO Densities during Sunrise at Kauai, J. Geophys. Res. 78, 746 (1973).
- Tr-75 H. Trinks, Ozone Measurements Between 90 and 110 km Altitude by Mass Spectrometer, Geophys. Res. Letters 2, 99 (1975).
- TS-72b R. P. Turco and C. F. Sechrist, Jr., An Investigation of the Ionospheric D Region at Sunrise. 1. Time Variation of Ozone, Metastable Oxygen and Atomic Oxygen, Radio Sci. 7, 703 (1972).
- US-62 U. S. Standard Atmosphere, 1962. Available from the U. S. Government Printing Office, Washington, D. C. 20402.
- US-66 U. S. Standard Atmosphere Supplements, 1966. Available from the U. S. Government Printing Office, Washington, D. C. 20402.

- Va-73a A. Vallance Jones, The Infrared Spectrum of the Airglow, Space Sci. Rev. 15, 355 (1973).
- VG-63 A. Vallance Jones and R. L. Gattinger, The Seasonal Variation and Excitation Mechanism of the  $1.58\mu$   $^1\Delta_g$ - $^3\Sigma_g^-$  Twilight Airglow Band, Planet. Space Sci. 11, 961 (1963).
- VI-69 M. N. Vlasov, Concentrations of Excited  $O_2(^1\Delta_g)$  Molecules in the Upper Atmosphere, Geomag. & Aeron. 9, 757 (1969).
- VI-70 M. N. Vlasov, Diurnal Pattern of the Concentration of Molecular Oxygen in the  $^1\Delta_g$  State in the Upper Atmosphere, Geomag. & Aeron. 10, 593 (1970).
- Vu-75 R. K. R. Vupputuri, Seasonal and Latitudinal Variations of  $N_2O$  and  $NO_x$  in the Stratosphere, J. Geophys. Res. 80, 1125 (1975).
- WE-70 H. C. Wood, W. F. J. Evans, E. J. Llewellyn, and A. Vallance Jones, Summer Daytime Height Profiles of  $O_2(^1\Delta_g)$  Concentration at Fort Churchill, Can. J. Phys. 48, 862 (1970).
- Wi-66 H. F. Winters, Ionic Adsorption and Dissociation Cross Section for Nitrogen, J. Chem. Phys. 44, 1472 (1966).
- WM-72 S. C. Wofsy, J. C. McConnell, and M. B. McElroy, Atmospheric  $CH_4$ ,  $CO$ , and  $CO_2$ , J. Geophys. Res. 77, 4477 (1972).
- WS-68 L. H. Weeks and L. G. Smith, A Rocket Measurement of Ozone Near Sunrise, Planet. Space Sci. 16, 1189 (1968).
- ZS-74 K. S. Zalpuri and Y. V. Somayajulu, Nitric Oxide Density Determination from Rocket Experiments at the Geomagnetic Equator, J. Atmos. Terr. Phys. 36, 1789 (1974).



## DISTRIBUTION LIST

### DEPARTMENT OF DEFENSE

Director  
Defense Advanced Research Proj. Agency  
ATTN: STO

Defense Communication Engineer Center  
ATTN: Code R410, James W. McLean

Director  
Defense Communications Agency  
ATTN: Code 480

Defense Documentation Center  
Cameron Station  
12 cy ATTN: TC

Director  
Defense Nuclear Agency  
ATTN: DDST  
ATTN: TISI, Archives  
3 cy ATTN: TITL, Tech. Library  
ATTN: RAAE

Dir. of Defense Research & Engineering  
Department of Defense  
ATTN: S&SS (OS)

Commander  
Field Command  
Defense Nuclear Agency  
ATTN: FCPR

Director  
Interservice Nuclear Weapons School  
ATTN: Document Control

Director  
Joint Strat. Target Planning Staff, JCS  
ATTN: JPST, Captain G. D. Goetz

Chief  
Livermore Division, Field Command, DNA  
Lawrence Livermore Laboratory  
ATTN: FCPRL

### DEPARTMENT OF THE ARMY

Commander/Director  
Atmospheric Sciences Laboratory  
US Army Electronics Command  
ATTN: DRSEL-BL-SY-S, F. E. Niles

Director  
BMD Advanced Tech. Center  
2 cy ATTN: ATC-T, Melvin T. Capps

Commander  
Harry Diamond Laboratories  
ATTN: DRXDO-NP, Francis N. Wimenitz  
ATTN: DRXDO-TI

Director  
TRASANA  
ATTN: R. E. DeKinder, Jr.

### DEPARTMENT OF THE ARMY (Continued)

Director  
US Army Ballistic Research Labs.  
ATTN: Lawrence J. Puckett  
ATTN: Mark D. Kregel

Commander  
US Army Foreign Science & Tech. Center  
ATTN: P. A. Crowley

Commander  
US Army Missile Intell. Agency  
ATTN: Jim Gamble

Commander  
US Army Missile Command  
ATTN: DRSMI-XS, Chief Scientist

Commander  
US Army Nuclear Agency  
ATTN: MONA-WE, J. Berberet

### DEPARTMENT OF THE NAVY

Chief of Naval Operations  
Navy Department  
ATTN: Alexander Brandt

Commander  
Naval Ocean Systems Center  
3 cy ATTN: Code 2200, Verne E. Hildebrand

Director  
Naval Research Laboratory  
3 cy ATTN: Code 7701, Jack D. Brown  
ATTN: Code 7750, S. Ossakow

Commander  
Naval Surface Weapons Center  
ATTN: Code WA501, Navy Nuc. Prgms. Off.  
ATTN: Code WX21, Tech. Lib.

Director  
Strategic Systems Project Office  
Navy Department  
ATTN: NSSP-2722, Fred Wimberly  
ATTN: NSP-2722, Marcus Meserole

### DEPARTMENT OF THE AIR FORCE

AF Geophysics Laboratory, AFSC  
ATTN: OPR, James C. Ulwick  
ATTN: OPR, Alva T. Stair  
ATTN: OPR, Harold Gardner

AF Weapons Laboratory, AFSC  
ATTN: NSS, John M. Kamm  
ATTN: SUL  
ATTN: DYT, Capt Mark A. Fry  
ATTN: DYT, Capt L. Wittwer  
ATTN: DYT, Peter W. Lunn

Hq. USAF/RD  
ATTN: RDQSM

DEPARTMENT OF THE AIR FORCE (Continued)

Commander  
Rome Air Development Center, AFSC  
ATTN: EMTLD, Doc. Library

SAMSO/SZ  
ATTN: SZJ, Major Lawrence Doan

Commander in Chief  
Strategic Air Command  
ATTN: ADWATE, Capt Bruce Bauer  
ATTN: XPFS, Maj Brian G. Stephan

Hq. USAF/SA  
ATTN: AFSA, Capt Henkle

ENERGY RESEARCH & DEVELOPMENT ADMINISTRATION

University of California  
Lawrence Livermore Laboratory  
ATTN: Ralph S. Hager, L-31  
ATTN: Donald R. Dunn, L-156

Los Alamos Scientific Laboratory  
ATTN: Doc. Con. for John Zinn  
ATTN: Doc. Con. for Eric Jones

OTHER GOVERNMENT AGENCIES

Department of Commerce  
Office of Telecommunications  
Institute for Telecom Science  
ATTN: William F. Utlaut

DEPARTMENT OF DEFENSE CONTRACTORS

Aerospace Corporation  
ATTN: Norman D. Stockwell  
ATTN: Doug Rawcliffe

Brown Engineering Company, Inc.  
ATTN: James E. Cato  
ATTN: Romeo DeLiberis  
ATTN: Joel D. Bigley

ESL, Inc.  
ATTN: James Marshall  
ATTN: C. Prettie

General Electric Company  
TEMPO-Center for Advanced Studies  
ATTN: Warren S. Knapp  
ATTN: Tim Stephens  
ATTN: DASIAC

General Research Corporation  
ATTN: John Ise, Jr.  
ATTN: Joel Garbarino

Jaycor  
ATTN: S. R. Goldman

Johns Hopkins University  
Applied Physics Laboratory  
ATTN: Document Librarian

DEPARTMENT OF DEFENSE CONTRACTORS (Continued)

Lockheed Missiles & Space Company, Inc.  
ATTN: D. R. Churchill

M.I.T. Lincoln Laboratory  
ATTN: Lib. A-082 for David M. Towle

Martin Marietta Aerospace  
Orlando Division  
ATTN: Roy W. Heffner

Mission Research Corporation  
ATTN: D. Sappenfield  
ATTN: R. Bogusch  
ATTN: R. Hendrick  
ATTN: Russell Christian

Physical Dynamics, Inc.  
ATTN: Joseph B. Workman

R & D Associates  
ATTN: Bryan Gabbard  
ATTN: Robert E. LeLevier

Science Applications, Inc.  
ATTN: D. Sachs  
ATTN: Curtis A. Smith  
ATTN: Daniel A. Hamlin  
ATTN: Jon Y. Wang  
ATTN: John I. Valerio  
ATTN: Melvin R. Schoonover

Science Applications, Inc.  
ATTN: B. F. Myers

Science Applications, Inc.  
Huntsville Division  
ATTN: Dale H. Divis  
ATTN: Noel R. Byrn

Stanford Research Institute  
ATTN: Ray L. Leadabrand  
ATTN: Walter G. Chestnut

VisiDyne, Inc.  
ATTN: J. W. Carpenter  
ATTN: Charles Humphrey